Operation of Copper Cavities at Cryogenic Temperatures

DISSERTATION

zur Erlangung des Doktorgrades
der Naturwissenschaften

vorgelegt beim Fachbereich Physik
der Johann Wolfgang Goethe-Universität
in Frankfurt am Main

von

Huifang Wang
aus Henan, China

Frankfurt am Main, 2023
(D30)

vom Fachbereich Physik der
Johann Wolfgang Goethe-Universität als Dissertation angenommen.

Dekan:	Prof. Dr. Roger Erb
Gutachter:	Prof. Dr. Ulrich Ratzinger
	Prof. Dr. Holger Podlech

Datum der Disputation: 12. Oktober 2023

Contents

List of Tables

List of Figures

Kapitel 1

Zusammenfassung

Der Betrieb von normalleitenden Beschleunigern bei kryogenen Temperaturen ist kürzlich zu einem interessanten Thema geworden. Der kryogene Betrieb von Ionenbeschleunigern wird erstmals seit etwa 2012 am IAP in Frankfurt diskutiert und untersucht. Einerseits zeigt der Werkstoff Kupfer bei Temperaturen von flüssigem Stickstoff und darunter eine deutlich höhere Leitfähigkeit. Andererseits reduziert der anomale Skin-Effekt die Verbesserung der Shunt-Impedanz. Ziel dieser Arbeit ist es zu untersuchen, wie sich der anomale Skin-Effekt auf die Effizienz von Kupferkavitäten im Temperaturbereich von 40 - 50 K auswirkt.

Für Experimente wurden drei $\lambda/4$ koaxiale Kavitäten entworfen und gebaut (s Abb. 1.1). Die genauen Längen des äußeren Zylinders und der Größe des Spalts wurden in Simulationen mit CST Microwave Studio (MWS) verifiziert: 735 mm für die 100 MHz-Kavität, 324 mm für die 220 MHz-Kavität und 201 mm für die 340 MHz-Kavität; die Spaltgröße beträgt jeweils 54 mm.

Die simulierten Gütewerte sind 13060 für die 100 MHz-Kavität, 17264 für die 220 MHz-Kavität und 19665 für die 340 MHz-Kavität. Die gemessenen Gütewerte sind jeweils 11803, 15812 und 17569, was 90.4 %, 91.6 % bzw. 89.3 % der simulierten Werte entspricht.

Zwei kleine Schleifen wurden als Eingangs- und Ausgangskoppler (s Abb. 1.2) verwendet. Ihre Kopplungsstärke hat die Größenordnung 10^{-4} bei Raumtemperatur und 10^{-3} bei kryogener Temperatur nahe 4 K. Das bedeutet, dass die Kopplung schwach genug für das Experiment ist und die gemessene belastete Güte Q_L vom Netzwerkanalysator als gute Annäherung für Q_0 angesehen werden kann.

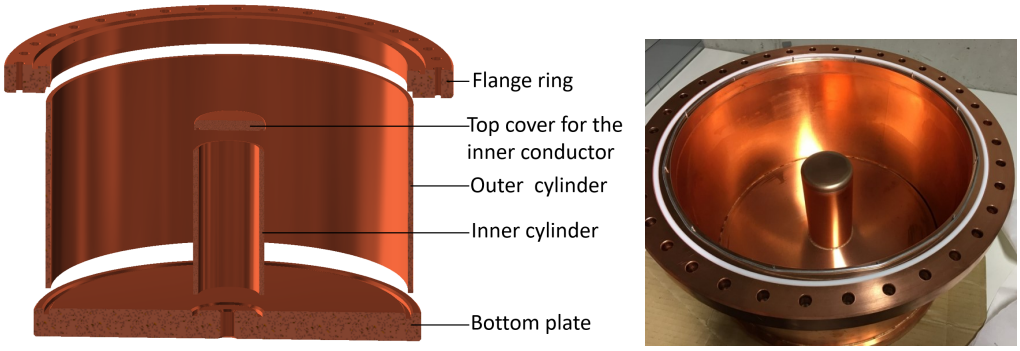

(a) (b)

Abbildung 1.1: Aufbau des koaxialen Resonators mit Kurzschlussboden. (a) Einzelteile vor dem Vakuumhartlöten als Schnittdarstellung. (b) Blick in den fertiggestellten Resonator mit eingelegter Alu-Drahtdichtung und Teflondichtung.

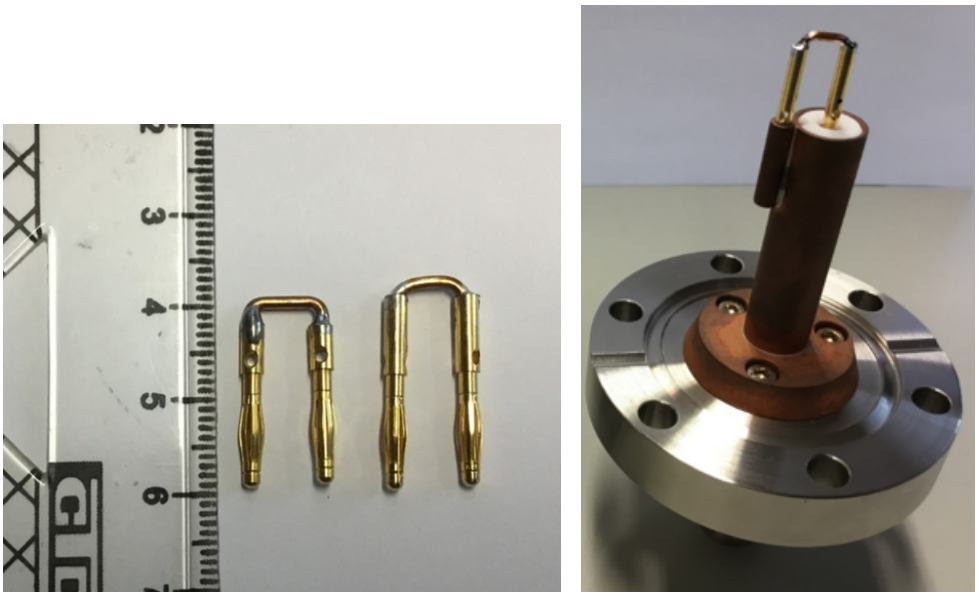

(a) (b)

Abbildung 1.2: In den Messungen verwendete Koppelschleifen. (a) Größe von Ein- bzw. Auskoppelschleife (links). (b) Montierter Koppler auf einem CF40 - Vakuumflansch.

Eine HF-Konditionierung erfolgte von 0 W bis zu 50 W cw und blieb für etwa drei Stunden auf dem Maximalpegel, um Verunreinigungen und Staubpartikel auf der Oberfläche abzubrennen. Die Kavitäten wurden durch eine Kombination aus einem Turbopumpstand und einer Ionengetterpumpe gepumpt, wie sie für den Test von

supraleitenden Kavitäten verwendet wird. Temperatursensoren wurden verwendet, um die Temperaturänderungen aufzuzeichnen. Nach der Kavitätsvorbereitung wurde der gesamte Versuchsaufbau in den Kryostaten gestellt und mit flüssigem Helium auf etwa 10 K heruntergekühlt.

Die Gütemessungen wurden während der Aufwärmphase der Kavität durchgeführt. Aus den Ergebnissen können wir schließen, dass die RRR-Werte des ursprünglichen Kupfers (SF-Cu) sehr niedrig waren – RRR $\cong$ 11. Dies ist nicht ungewöhnlich für Standardrohre aus Kupfer mit nicht spezifizierten kryogenen Eigenschaften. Anschließend wurde die 340 MHz Kavität mattiert verkupfert und später eine Stunde lang bei 400°C vakuumgeglüht. Die Ergebnisse zeigten (s Abb. 1.3), dass die

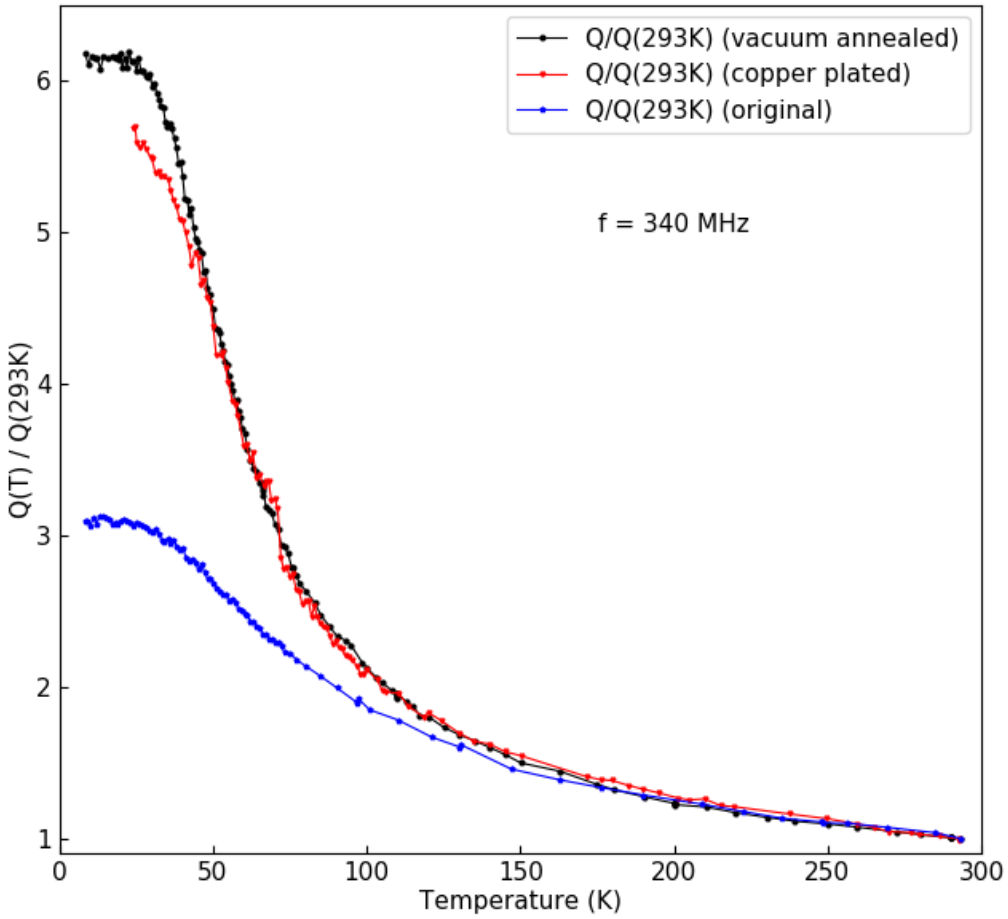

Abbildung 1.3: Gemessene $Q(T)/Q(293K)$ – Werte über Temperaturen T für alle drei Oberflächenbedingungen des 340 MHz Kavität.

Kupferplattierung den Q-Faktor bei tiefen Temperaturen signifikant verbessern kann,

was bedeutet, dass der RRR-Wert viel größer wird. Das nachfolgende Vakuumglühen ergab zur Kupferplattierung eine kleine zusätzliche Verbesserung.

Da die gängige Diffusionstheorie auf der Basis von Elektronen -Kleinwinkelstreuung zur Berechnung des anomalen Skineffektes bekanntermaßen etwas zu gute Ergebnisse im Mikrowellenbereich unter 1 GHz und im hier interessierenden Temperaturbereich liefert, wurde ein "geometrisches Modell" entwickelt, welches darauf gründet, dass stark winkeländernde sogenannte Umklapp-Prozesse eine wesentliche Rolle für die Elektronenbewegung spielen. Dieses Modell vergleicht sich gut mit eigenen Messungen und mit Messungen aus der Literatur.

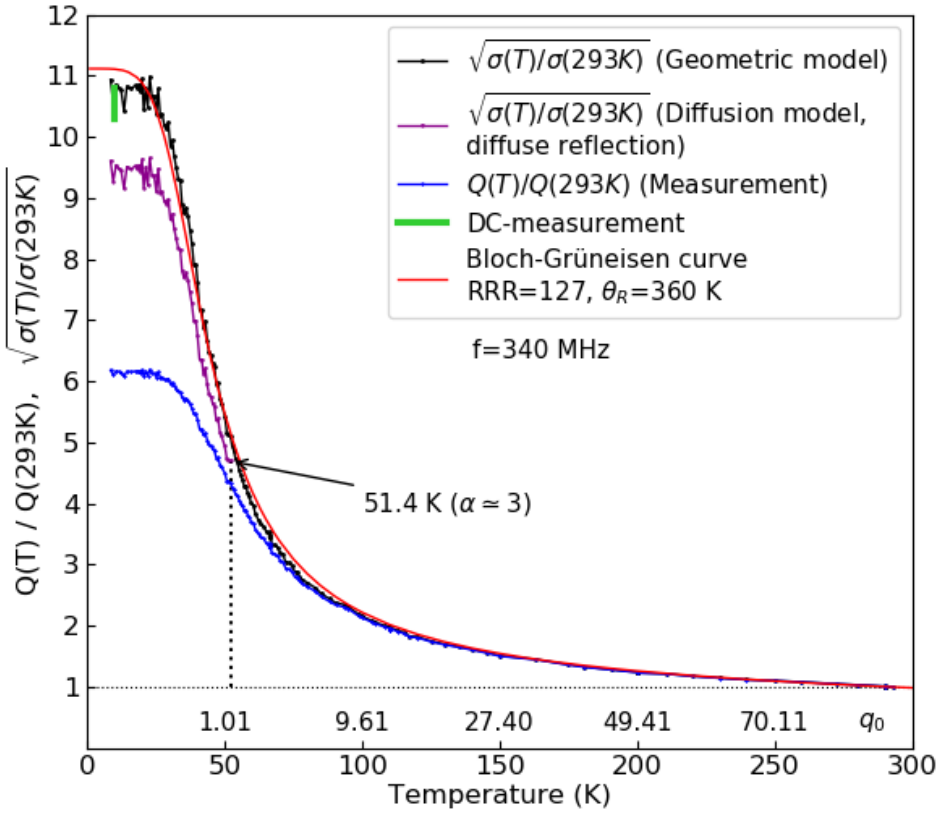

Abbildung 1.4: Quadratwurzeln der DC-Leitfähigkeitsverhältnisse, berechnet aus den gemessenen Q-Wertsverhältnissen. Die DC-Messung für galvanisch verkupferte Schichten ist aus Ref. [14].

Vergleicht man die gemessenen Ergebnisse der 340 MHz Kavität nach dem Verkupfern und Vakuumglühen mit dem berechneten RRR-Wert unter Bezugnahme auf die Theorie und das geometrische Modell, die in Kapitel 4.3 beschrieben sind,

so ergibt sich folgendes: $Q(T)/Q(293K)$ beträgt 6,18 bei der niedrigsten Temperatur, während das zurückgerechnete Gleichstromverhältnis $\sqrt{\sigma(T)/\sigma(293K)}$ bei der niedrigsten Temperatur aus dem geometrischen Modell sich zu etwa 11 ergibt und der RRR-Wert für diese verkupferte Schicht sich zu etwa $11^2 = 121$ ergibt (s Abb. 1.4). Es liegt nur geringfügig über den in Ref. [14] veröffentlichten Messergebnissen: Die DC-gemessenen RRR-Werte von galvanisch verkupferten und vakuumgelühten Schichten liegen demnach zwischen den Werten 107 und 117. Der auf dem Diffusionsmodell basierende berechnete Wert von $\sqrt{\sigma(T)/\sigma(293K)}$ bei der niedrigsten Temperatur liegt dagegen etwa 18 % unter dem Wert aus dem geometrischen Modell.

Der RRR - Wert der galvanisch aufgebrachten Kupferschicht wird durch im Handel erhältliches OF-Cu, DIN 2.0040, sogar noch deutlich übertroffen. Die technische Umsetzung des hier verfolgten Vorhabens ist also von den Werkstoffen und von der Verarbeitung her gegeben.

Das wesentliche Ergebnis der Arbeit ist, dass das Verhältnis $Q(T)/Q(293K)$ bei 40 K immer noch 5.37 und bei 50 K 4.5 beträgt. Um diese Faktoren werden die HF-Leistungsverluste von bei diesen Temperaturen betriebenen Beschleunigern reduziert.

Nach den simulierten Ergebnissen des Temperaturverhaltens auf einen kurzen Energieimpuls bleibt der Temperaturanstieg während eines Impulses im Bereich von 1 ms bei einer definierten 40 K-Starttemperatur in einem akzeptablen Bereich, (s Abb. 1.5). Die Änderung von Q_0 ist gering und die geringfügige Änderung der reflek-

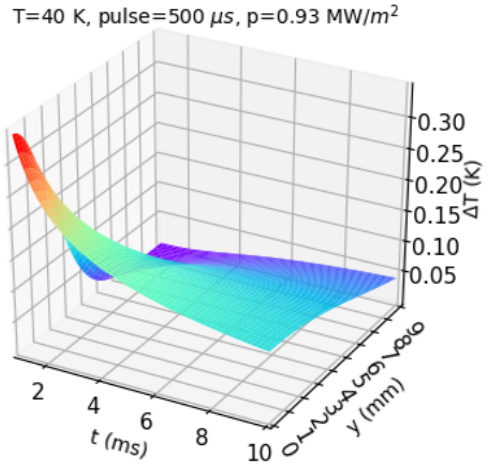

Abbildung 1.5: Temperaturverteilung im Zeitverlauf und in der Eindringtiefe.

tierten HF-Leistung kann sicher von den HF-Reglern ausgeglichen werden. Zusätzlich

zeigten die Messungen in Labors zur Entwicklung von Elektronenbeschleunigerkavitäten bei kryogener Temperatur eine höhere elektrische Oberflächenfeldgrenze [17, 24, 23]. Solche Vorteile sollten ein optimiertes Beschleuniger-Layout in Bezug auf HF-Leistungsverstärker und Kompaktheit des Linearbeschleunigers bei kryogenen Temperaturen ermöglichen - auch bei den deutlich niedrigeren Frequenzen für Ionenbeschleuniger. Kompakte und einfache Driftröhrenkavitäten, wie in Abb. 1.6 dargestellt, sind für den Betrieb bei kryogenen Temperaturen vorzuziehen. Die KONUS- und APF-Strahldynamik ermöglicht eine Abfolge einfacher Driftröhren, die keine Fokussierungselemente enthalten - auch schon bei niedrigen Strahlenergien.

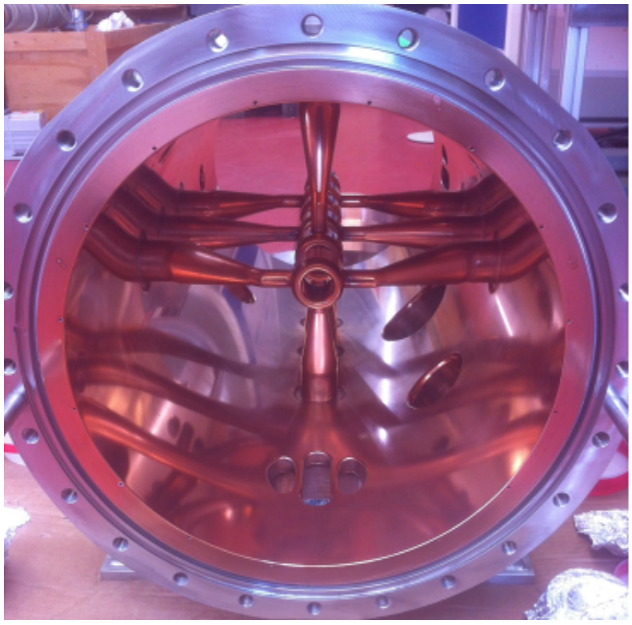

Abbildung 1.6: Blick in dem 325 MHz Prototyp von einer CH-Kavität mit 7 Spalten für den Betrieb bei Raumtemperatur[1]. Der Innendurchmesser beträgt 330 mm.

Im Falle des FAIR-Projekts in Darmstadt könnte ein 100 AMeV Injektor Linac in das Synchrotron SIS100 - der die spezifizierte hohe Partikelzahl bereitstellt - in einem späteren Upgrade-Projekt durch eine solche Technologie realisiert werden. Effektive Beschleunigungsgradienten von 20 bis 25 MV/m erscheinen realistisch - das ist eine Größenordnung über den jetzt bei GSI betriebenen Unilac - Kavitäten.

Weiterhin könnte zum Beispiel ein sehr kompakter, kurz gepulster, medizinischer Linearbeschleuniger für intensive Protonenpulse zur Behandlung entsprechend der neuen Proton -Flash - Radiotherapie mit dieser Technik aufgebaut werden.

Chapter 2

Introduction

A synchrotron is a particular type of cyclic particle accelerator and the first accelerator concept to enable the construction of large-scale facilities [10], such as the largest particle accelerator in the world, the 27-kilometre-circumference Large Hadron Collider (LHC) by CERN near Geneva, Switzerland, the European Synchrotron Radiation Facility (ESRF) in Grenoble, France for the synchrotron radiation, the superconducting, heavy ion synchrotron SIS100 under construction for the FAIR facility at GSI, Darmstadt, Germany and so on. Unlike a cyclotron, which can accelerate particles starting at low kinetic energy, a synchrotron needs a pre-acceleration facility to accelerate particles to an appropriate initial value before synchrotron injection. A pre-acceleration can be realized by a chain of other accelerator structures like a linac, a microtron in case of electrons, for example, Proton and ion injectors Linac 4 and Linac 3 for the LHC, UNLAC as the injector for the SIS18 in GSI and in future the SIS18 as injector for the SIS100. The linac is a commonly used injector for the ion synchrotron and consists of some key components. The three main parts of a linac are: An ion source creating the particles, a buncher system or an RFQ followed by the main drift tube accelerator DTL. In order to meet the energy and the beam current requirement of a synchrotron injector linac, its cost is a remarkable percentage of the total facility costs.

However, the normal conducting linac operation at cryogenic temperatures can be a promising solution in improving the efficiency and reducing the costs of a linac. Synchrotron injectors operate at very low duty factor with beam pulse lengths in 1 micros to 100 micros range, as most of the time is needed to perform the synchrotron

cycle. Superconducting linacs are not convenient, as they cannot efficiently operate at low duty factor and high beam currents

The cryogenic operation of ion linacs is discussed and investigated at IAP in Frankfurt since around 2012 [1, 37]. The motivation was to develop very compact synchrotron injectors at reduced overall linac costs per MV of acceleration voltage. As the needed beam currents for new facilities are increasing as well, the new technology will also allow an efficient realization of higher injector linac energies, which is needed in that case. Operating normal conducting structures at cryogenic temperature exploits the significantly higher conductivity of copper at temperatures of liquid nitrogen and below. On the other hand, the anomalous skin effect reduces the gain in shunt impedance quite a bit[25, 31, 9]. Some intense studies and experiments were performed recently, which are encouraging with respect to increased field levels at linac operation temperatures between 30 K and 70 K [17, 24, 4, 23, 5, 8]. While these studies are motivated by applications in electron acceleration at GHz-frequencies, the aim of this paper is to find applications in the 100 to 700 MHz range, typical for proton and ion acceleration. At these frequencies, a higher impact in saving RF power is expected due to the larger skin depth, which is proportional to $f^{-1/2}$ with respect to the normal skin effect. On the other hand, it is assumed that the improvement in maximum surface field levels will be similar to what was demonstrated already for electron accelerator cavities. This should allow to find a good compromise between reduced RF power needs for achieving a given accelerator voltage and a reduced total linac length to save building costs.

A very important point is the temperature stability of the cavity surface during the RF pulse. This is of increasing importance the lower the operating temperature is chosen: the temperature dependence of the electric conductivity in copper gets rather strong below 80 K, as long as the RRR - value of the copper is adequate. It is very clear, that this technology is suited for low duty cycle operated cavities only - with RF pulse lengths below one millisecond. At longer pulses the cavity surface will be heated within the pulse to temperatures, where the conductivity advantage is reduced substantially. These conditions fit very well to synchrotron injectors or to pulsed beam power applications.

H – Mode structures of the IH – and of the CH – type are well-known to have rather

small cavity diameters at a given operating frequency. Moreover, they can achieve effective acceleration voltage gains above 10 MV/m even at low beam energies, and already at room temperature operation[29]. With the new techniques of 3d – printing of stainless steel and copper components one can reduce cavity sizes even further – making the realization of complex cooling channels much easier[15].

Another topic are copper components in superconducting cavities – like power couplers. It is of great importance to know exactly the thermal losses at these surfaces, which can't be cooled efficiently in an easy way[14].

The surface impedance of cold beam pipes is as well an important subject, where the anomalous skin effect can cause a large contribution to the beam driven wall losses[11].

A so-called diffusion theory of the anomalous skin effect is existing since about 70 years and is briefly introduced in Chapter 4.2.1[31]. It is valid for all frequencies and temperatures. However, there are experiments which show higher RF losses then predicted by that theory in some RF and temperature ranges.

In this work a new concept is introduced and new formulas are derived to calculate the resistive wall losses in "simple" metals like copper and silver, assuming a spherical Fermi – surface in momentum space. The method is suited to calculate ohmic wall losses by adding the anomalous skin effect to the classical theory. The temperature dependent anomalous contribution is explained by a detailed presentation of the geometric model[30].

In the first part of this work, RF cavity knowledge is introduced: important resonator parameters, basic information about the coaxial resonator, power coupling and S-parameters (Chapter 3); the skin effect and anomalous skin effect (Chapter 4). Next, the physical and geometrical parameters are investigated and determined in 3-dimensional RF-simulations with CST Microwave Studio (MWS) (Chapter 5). The measurement method and the preparation for the experiment is described in Chapter 6 and the measured results are shown in Chapter 7. Finally, the temperature response of the cavity wall on a short, instantaneous pulse of energy at the surface was simulated with the Python code.

Chapter 3

RF Cavities

3.1 Resonator Parameters

3.1.1 Stored Energy W

The energy of a resonator W is stored in the electromagnetic RF field and can be calculated by the integral over the volume of the cavity V at constant amplitude level:

$$W = \frac{1}{2}\int_V \left(\mu_0|\vec{H}(x,y,z,t)|^2 + \varepsilon_0|\vec{E}(x,y,z,t)|^2\right) dV = const. \tag{3.1}$$

which is constant in time. The energy oscillates between the electric and the magnetic field $\vec{E}$ and $\vec{H}$ respectively and the phase shift between both fields is 90^0, which means, every quarter of the RF period, when the phase becomes $\varphi = \omega t = n \cdot \pi/2$, one of these two fields reaches its maximum while the other one is zero. The stored energy can also be expressed independently from time as

$$W = \frac{1}{2}\int_V \mu_0 H_0^2 dV = \frac{1}{2}\int_V \varepsilon_0 E_0^2 dV. \tag{3.2}$$

3.1.2 Surface Resistance R_s and Power Loss P_c

As will be described in Chapter 4, due to the skin effect, the electric current does not flow homogeneously through the conductor with high frequency alternating field, but is concentrated only in a thin layer on the surface, which is characterized by the skin

depth $\delta = \sqrt{2\rho/\mu\omega}$, where μ is the permeability of the conductor, $\mu \simeq \mu_0$ for copper. The surface resistance of the normal conducting resonator depends on the electrical conductivity σ of the material and on the skin depth δ and is calculated as follows:

$$R_s = \frac{1}{\sigma\delta} = \sqrt{\frac{\mu\omega}{2\sigma}} = \sqrt{\frac{\mu\omega\rho}{2}} = \sqrt{\pi\mu\rho f} \tag{3.3}$$

where ρ is the electrical resistivity. This equation shows that the surface resistance in the "normal" conducting case is proportional to $\sqrt{f}$.

Due to the surface current induced by the magnetic field, power losses P_c occur at the resonator surface. It can be obtained by integrating the magnetic field over the inner surface of the resonator:

$$P_c = \frac{1}{2} R_s \int_s |\boldsymbol{H}_0|^2 dA \tag{3.4}$$

Details will be explained in Chapter 4.1.

3.1.3 Quality Factor

An RF resonator is an oscillating system which is characterized by the quality factor with respect to power losses. The quality factor Q_0 is determined by the ratio of the reactive power $\omega \cdot W$ and the power loss P_c. A real accelerator system consists of at least an input coupler to feed the cavity with RF power from a generator and an output coupler (is also called the pickup probe) serving as a detector of the RF phase and amplitude. The stored field energy is dissipated in the resonator surface due to the surface resistance. On the other hand, there is energy flowing from the RF amplifier into the resonator through the input coupler. If the coupler is not perfectly matched, a fraction of RF power is flowing back to the RF amplifier. Further on, every pickup probe also contributes to the losses (usually negligible). The power levels at different positions of an accelerator system is shown in Fig. 3.1. Three different quality factors for an accelerator system will be introduced here due to the different power flows.

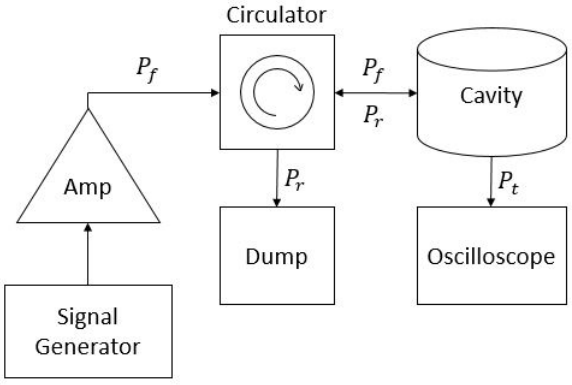

Figure 3.1: Power levels at different positions of an accelerator system[7]. P_f is the forward power from the generator, P_r the reflected power, P_c the power loss inside the cavity, P_e and P_t the emitted and externally dissipated power from the input and output couplers, respectively.

Unloaded Quality Factor Q_0

Due to the induced surface currents inside a cavity, there will be an ohmic power loss P_c, as described in Chapter 3.1.2. The unloaded quality factor Q_0 is a parameter to describe a resonator's ability to store electromagnetic energy and is thus defined by the ratio of the stored energy W and the power loss P_c with no regards on couplers and their influence:

$$Q_0 = \frac{\omega W}{P_c} = 2\pi \frac{W}{T P_c}. \tag{3.5}$$

If the input power into the resonator is being switched off at time $t = 0$, the stored energy W decreases with time t as[26, Chapter 7]

$$\frac{dW}{dt} = -P_c = -\frac{\omega W}{Q_0} \tag{3.6a}$$

$$\frac{1}{W} dW = -\frac{\omega}{Q_0} dt \tag{3.6b}$$

$$W(t) = W_0 \cdot e^{-\frac{\omega}{Q_0} t} = W_0 \cdot e^{-t/\tau} \tag{3.6c}$$

where W_0 is the initial value of the stored energy when the power supply is just cut off and $\tau = Q_0/\omega$. As we can see, the stored energy W decreases with time t exponentially. After time τ, the stored energy W has reduced to $1/e$ of its initial value.

The response of a resonator to the external excitation at $\omega_0 \pm \Delta\omega$ is described by the Lorentz function:

$$|A(\omega)| = \frac{|A_0|}{\sqrt{1 + Q_0^2(\frac{\Delta\omega}{\omega_0})^2}} \tag{3.7}$$

This function describes the frequency distribution of the resonance, where A_0 is the voltage amplitude of the signal at resonance at resonant frequency ω_0. The power of the signal is proportional to $|A(\omega)|^2$. In the resonance curve of the power versus frequency , -3dB is the point of half the power, which means, $|A(\omega')| = |A(\omega_0)|/\sqrt{2}$. The quality factor is now obtained from the ratio of ω_0 to the frequency width $\Delta\omega = 2(\omega' - \omega_0)$ at FWHM (Full Width Half Maximum). This is called 3dB-method.

$$Q_0 = \frac{\omega_0}{\Delta\omega_{3dB}} = \frac{f_0}{\Delta f_{3dB}} \tag{3.8}$$

Experimentally the resonance curve is measured with the parameter S_{21} (see Chapter 3.4) using a network analyzer. Typically, the values for the quality factor are $10^3 - 10^5$ for normal conducting and $10^8 - 10^{11}$ for superconducting cavities.

According to Eq. (3.5), Q_0 is inversely proportional to the power loss P_c. Furthermore, $P_c \propto R_s \propto \sqrt{\rho}$ according to Eqs. (3.3) and (3.4). Therefore,

$$Q_0 \propto \frac{1}{\sqrt{\rho}} \tag{3.9}$$

External Quality Factor

When the generator is turned off, the emitted RF power by the input coupler is P_e and by the pickup is P_t. Analogously, the external quality factor Q_e for the input

coupler and Q_t for the pickup are defined as:

$$Q_e = \frac{\omega W}{P_e} \tag{3.10}$$

$$Q_t = \frac{\omega W}{P_t} \tag{3.11}$$

Loaded Quality Factor Q_L

The unloaded quality factor Q_0 (or the intrinsic quality factor) depends only on the power loss P_c at the surface of a cavity, while the external quality factor is determined only by the emitted power from the couplers, when the generator is turned off. For the whole system, another quality factor related to the total power loss P_{tot}, the loaded quality factor Q_L, is defined:

$$Q_L = \frac{\omega W}{P_{tot}} \tag{3.12}$$

where P_{tot} is equal to:

$$P_{tot} = P_c + P_e + P_t \tag{3.13}$$

According to Eqs. (3.5, 3.10 and 3.12), we obtain

$$\frac{P_{tot}}{\omega W} = \frac{P_c + P_e + P_t}{\omega W} \tag{3.14}$$

$$\frac{1}{Q_L} = \frac{1}{Q_0} + \frac{1}{Q_e} + \frac{1}{Q_t} \tag{3.15}$$

3.2 Coaxial Resonators

For relatively low frequencies especially below about 100 MHz, some accelerating cavities are variants of the simple coaxial resonators. By placing conducting end walls on a section of a coaxial line, two different widely used types of coaxial resonators

for accelerator applications can be formed: half-wave resonators and quarter-wave resonators. A standing wave is excited in the resonators.

3.2.1 Coaxial Half-Wave Resonator

Without considering the specific modifications needed for the acceleration, a coaxial half-wave resonator, shown in Fig. 3.2, can be formed simply by placing conducting walls at both ends ($z = 0$ and $z = l = \lambda/2$) of a section from a coaxial line with an inner conductor of radius a and an outer conductor of radius b.

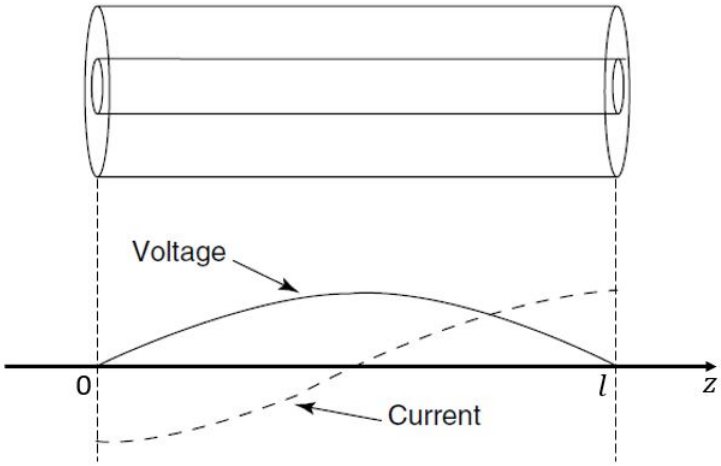

Figure 3.2: Coaxial half-wave resonator with voltage and current standing waves [38, page 23].

The enclosed length of the resonator is half a wavelength of the fundamental mode and inside the resonator, a transverse electromagnetic (TEM) standing-wave mode is excited. Resonance occurs when the boundary conditions at the inner and outer conductor $E_z = E_\phi H_r = 0|_{r=a,r=b}$ and at the end walls $E_r = E_\phi = H_z = 0|_{z=0,z=l}$ are satisfied. In vacuum the relation between B- and H-fields is $B = \mu_0 H$. Imaging that on the inner conductor a current wave $I_0 e^{i(\omega t - kz)}$ travels in the $+z$ direction and another current wave $I_0 e^{i(\omega t + kz)}$ travels in the $-z$ direction. The superposition of these two waves produces a standing wave that satisfies all the boundary conditions and the total current is $2I_0 cos(\pi z/l)e^{i\omega t}$. With the help of the boundary conditions and in conjunction with $Ampère{\cdot}s$ law, the azimuthal magnetic field B_ϕ (Eq. 3.16) can be calculated. From the differential form of $Faraday{\cdot}s$ law, the radial electric

field can be obtained (Eq. 3.17).

$$B_\phi(r,z,t) = \frac{\mu_0 I_0}{\pi r} cos(\pi z/l) e^{i\omega t} \tag{3.16}$$

$$E_r(r,z,t) = \sqrt{\frac{\mu_0}{\varepsilon_0}} \frac{I_0}{\pi r} sin(\pi z/l) e^{i(\omega t+\pi/2)} \tag{3.17}$$

The stored energy is

$$W = \frac{\mu_0 l I_0^2 ln(b/a)}{2\pi} \tag{3.18}$$

To make the cavity in Fig. 3.2 suitable for acceleration, it can be modified by introducing beam holes in the inner and outer conductors at $z = l/2$ where the voltage is maximum. A practical application of this kind of resonator is depicted in Fig. 3.3. As shown in Fig. 3.3, the beam can move along a radial path without

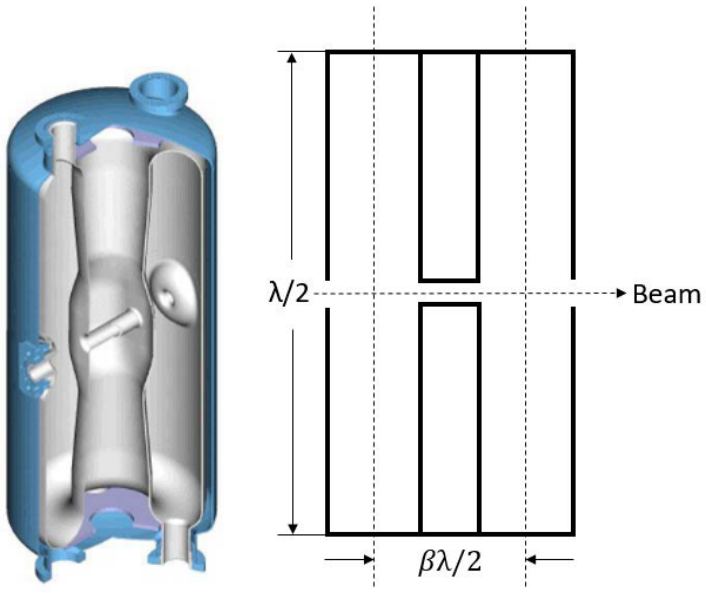

(a) (b)

Figure 3.3: (a): niobium prototype of a coaxial half-wave cavity for the RIA driver linac at Argonne National Laboratory [33]. (b): cut view of the coaxial half-wave cavity.

seeing any field within the inner conductor and it can be accelerated on both sides between the inner and outer conductors by choosing the appropriate injection phase and beam velocity so that the field reverses sign when the beam travels across the

inner conductor.

3.2.2 Coaxial Quarter-Wave Resonator

A coaxial quarter-wave resonator is formed by placing a conducting wall at one end of a section of a coaxial line. The other end is terminated by a capacitance, as shown in Fig. 3.4. Ignoring the difference in the way of termination, the distribution of

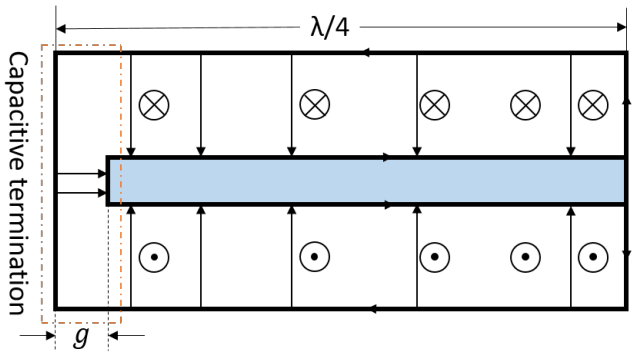

Figure 3.4: Coaxial quarter-wave resonator with the distribution of the electromagnetic field.

the electromagnetic field in a quarter-wave resonator is the same as in a half-wave resonator, which is given by Eq. (3.16 and 3.17). Only the length of the quarter-wave resonator is reduced by about a factor two.

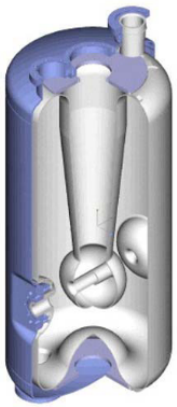

Figure 3.5: Niobium prototype of a coaxial quarter-wave cavity for the RIA driver linac at Argonne National Laboratory [33].

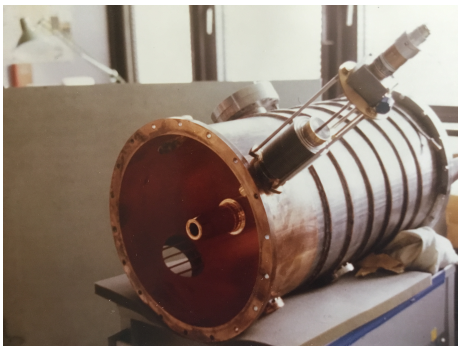

Figure 3.6: A harmonious buncher for the heavy ion post accelerator in Garching, Germany [28].

Like the half-wave resonator, the particles can be accelerated between the inner conductor and the outer cylindrical wall, as shown in Fig. 3.5. Furthermore, an electric field suitable for acceleration can also be obtained along a single gap between the inner conductor and the end wall, as shown in Fig. 3.6. The beam moves along the axial path inside the inner conductor without acceleration and then is accelerated by the electric field between the inner conductor and the end wall. More design details for the quarter-wave resonator are given by Moreno [22, pages 227-230].

3.3 Power Coupling

In order to enable a resonator to accelerate particles, the RF power supplied by a generator must be fed into the resonator through a coupler. There are three most common methods for coupling electromagnetic energy into or out of a cavity: inductive coupling, capacitive coupling and galvanical coupling. For the galvanical coupling, the inner conductor of a coaxial line will be connected to some position within the resonator surface.

Coupling strength is a parameter describing a ratio of RF power levels. As described in Chapter 3.1.3, normally an input coupler and one or more pickup-probes will be used for a cavity. The coupling factor β_e of the input coupler and β_t as sum of all pickup-probes are defined as

$$\beta_e = \frac{P_e}{P_c} = \frac{Q_0}{Q_e}, \quad \beta_t = \frac{P_t}{P_c} = \frac{Q_0}{Q_t} \tag{3.19}$$

Three cases of the coupling strength β_e correspond to three characteristic situations:

$$\beta \begin{cases} < 1, & \text{undercoupled, the power } P_e \text{ extracted through the coupler} \\ & \text{is lower than the intrinsic loss } P_c \text{ of the cavity} \\ = 1, & \text{critically coupled} \\ > 1, & \text{overcoupled} \end{cases} \tag{3.20}$$

Eq. (3.15) can be now expressed as

$$Q_0 = Q_L(1 + \beta_e + \beta_t) \tag{3.21}$$

The coupling factors β_e and β_t can be calculated from the measured S-parameters, which are described in Chapter 3.4. In most cases $\beta_t \simeq 0$ and can be neglected.

3.3.1 Inductive Coupling

For the inductive coupling one uses a coupling loop at the end of a coaxial transmission line (see Fig. 3.7) to couple the magnetic field into the resonator. The alternating

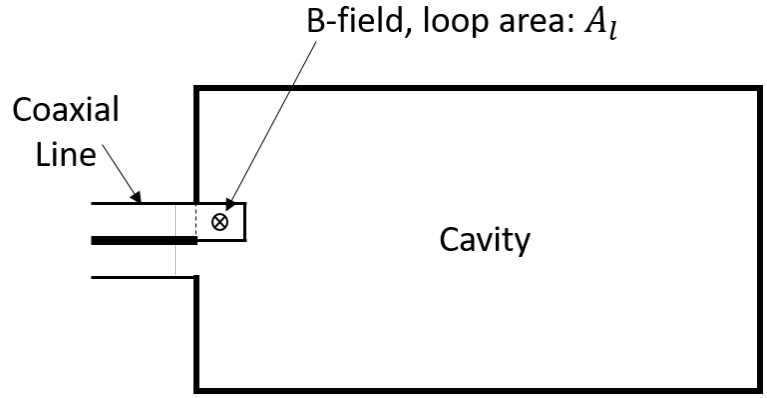

Figure 3.7: Scheme of the inductive coupling[38, pg.140].

magnetic field penetrates into the cavity through the loop and induces a voltage U_l along the loop. In order that the resonator can be coupled without reflection, the impedance of the coupler should be equal to that of the supply cable, which is usually 50Ω (Compare Eq. (3.28) on geometric conditions). The size of the coupling area must be large enough that the power P_f provided by the amplifier can meet the needs for operating the resonator. Without reflections and beam loads, P_f is equal to the power loss P_c that is dissipated in the wall of the resonator. This corresponds to $\beta_e = 1$, critical coupling. Then,

$$P_f = P_c = \frac{U_{l,eff}^2}{Z_L} = \frac{U_{l.eff}^2}{50\Omega} = \frac{U_{l,0}^2}{100\Omega} \tag{3.22}$$

and

$$U_{l,0} = \sqrt{P_c \cdot 100\Omega} \tag{3.23}$$

where $U_{l,0}$ is the amplitude along the coaxial line and at the same time the voltage induced in the coupler loop to get $\beta_e = 1$. According to the law of induction:

$$U_l = -\frac{d\Phi}{dt} = -\frac{d}{dt}\int BdA_l = -A_l\frac{d}{dt}(B_0 e^{i\omega t})cos\alpha = -A_l i\omega B_0 e^{i\omega t}cos\alpha \tag{3.24}$$

where A_l is the area of the loop and B_0 is the amplitude of the magnetic field averaged over the area at the location of the loop. α describes the angle of the loop area vector against the magnetic field vector. The absolute value of the voltage induced in the loop is

$$|U_{l,0}| = A_l\omega B_0 cos\alpha \tag{3.25}$$

If the magnetic field is perpendicular to the loop, namely, $\alpha = 0$, the area A_l of the loop required for critical coupling can be obtained from Eq. (3.25)

$$A_l = \frac{|U_{l,0}|}{\omega|B_0|} \tag{3.26}$$

At critical coupling, $P_f = P_c = P_e$, and substituting Eqs. (3.22 and 3.25) into Eq. (3.10), the Q factor can be expressed as:

$$Q_0 = Q_e = \frac{100\omega W}{U_{l,0}^2} = \frac{100W}{\omega(A_l B_0 cos\alpha)^2} \tag{3.27}$$

3.3.2 Capacitive Coupling

For the capacitive coupling, an electric-coupling probe or antenna (see Fig. 3.8) is introduced into the system to couple the electric field into the resonator. As the necessary capacitive coupling strength for a normal conducting structure can easily cause multipacting or arcing, the capacitive coupling is mainly used for the superconducting structures. This coupling method has also technical advantages in

case of superconducting resonator, like easier cooling than the inductive coupling coupler.

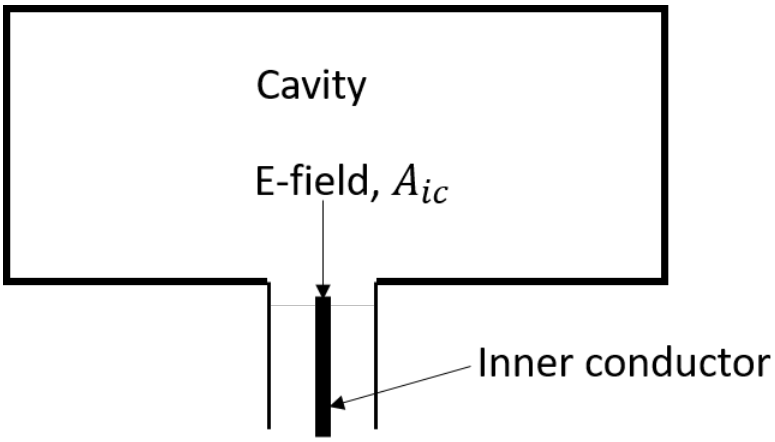

Figure 3.8: Scheme of the capacitive coupling[38, pg.140].

The coupling strength of a capacitive coupler is affected by the position of the coupler on the resonator and its detailed geometry. In the following, the effect of the radius of the inner conductor of a coaxial line on the coupling strength and on the external quality factor will be studied.

As in the case of the inductive coupling, in order to couple the power into the resonator without reflection, the impedance of the coaxial coupler for the capacitive coupling should also be 50Ω. The coaxial line impedance in vacuum is given by

$$Z_L = \sqrt{\frac{L}{C}} = \sqrt{\frac{\mu_0 (ln(b/a))^2}{4\pi^2 \varepsilon_0}} = \frac{ln(r_o/r_i)}{2\pi} \sqrt{\frac{\mu_0}{\varepsilon_0}} \tag{3.28}$$

where r_o is the radius of the outer conductor and r_i the radius of the inner conductor of the coaxial coupler. From this equation one obtains the required ratio of the radius r_o and r_i

$$50\Omega \simeq 60 ln(r_o/r_i) \tag{3.29}$$

$$r_o/r_i \approx 2.3 \tag{3.30}$$

The first Maxwell-equation in vacuum obtained from Gauss's law is

$$\nabla \cdot E = \frac{\rho}{\varepsilon_0} \tag{3.31}$$

$$\rho = \varepsilon_0 \nabla \cdot E \tag{3.32}$$

where ρ is the total electric charge density (total charge per unit volume). For simplification, we assume that the coupling charge q due to the electrical field E only exists on the front surface of the inner conductor with the area of A_{ic}. According to Eq. (3.32), the charge q is given by

$$q \simeq \varepsilon_0 \int_V \nabla \cdot E dV = \varepsilon_0 \int_A E dA = \varepsilon_0 E A_{ic} \tag{3.33}$$

Since the electric field is sinusoidal, the amount of the charge q also varies with time as a harmonic function:

$$q(t) = q e^{i\omega t} \tag{3.34}$$

Thus the current is

$$I(t) = \frac{dq}{dt} = i\omega q e^{i\omega t} \tag{3.35}$$

The power P_e flowing out of the coupler when the generator is switched off is

$$P_e = \frac{1}{2} Z_L I_0^2 \tag{3.36}$$

Substituting Eqs. (3.33 and 3.35) into Eq. 3.36, one obtains

$$P_e = 25(\varepsilon_0 \omega E_0 A_{ic})^2 = 100\pi^4 \varepsilon_0^2 f^2 E_0^2 r_i^4 \tag{3.37}$$

Now considering a cavity with the stored energy W and the resonance frequency

f, the external quality factor Q_e can be matched to Q_0 by

$$Q_e = \frac{\omega W}{P_e} = \frac{W}{50\pi^3 \varepsilon_0^2 f E^2 r_i^4} \tag{3.38}$$

To get Q_e, the stored energy W and the radial electrical field E must be able to be calculated. For real cavities, this can be done by means of numerical calculations. However, analytical solutions can only be obtained for some analytically solvable resonators.

3.4 S-Parameters

In this section we will study the coupler-cavity system from the wave perspective, which allows us to reexamine the cavity system from a more physical point. We will describe the propagation, transmission, reflection, and interference of the waves both in the couplers and in the cavity with an important tool for the analysis, called the scattering matrix [2, 27]. The coupler-cavity system can be considered as a two-port-device that has two channels, as shown in Fig. 3.9. For each channel there is generally an incident wave and an outgoing wave. By defining the scattering matrix,

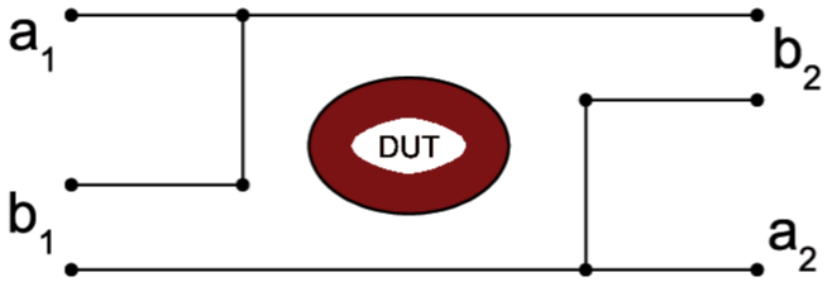

Figure 3.9: Transformation of the RF wave passing through a resonator [6].

the incident waves are normalized. The incoming traveling waves are represented by $a_i, i = 1, 2$, and the outgoing waves are represented by $b_i, i = 1, 2$. The scattering matrix S is defined as the transformation matrix of the column vector $\mathbf{a}$ of the incident waves into the column vector $\mathbf{b}$ of the outgoing waves. Thus, the 2×2

scattering matrix can be expressed as

$$\begin{pmatrix} b_1 \\ b_2 \end{pmatrix} = \begin{bmatrix} s_{11} & s_{12} \\ s_{21} & s_{22} \end{bmatrix} \begin{pmatrix} a_1 \\ a_2 \end{pmatrix} \tag{3.39}$$

All the parameters in the scattering matrix are directly related to the voltage waves.

The diagonal element s_{ii} is the reflection coefficient Γ in the ith port. The off-diagonal element s_{ij} is the transmission coefficient from port j into port i. Rewriting Eq. (3.39) in the form of a system of equations:

$$b_1 = s_{11}a_1 + s_{12}a_2 \tag{3.40}$$

$$b_2 = s_{21}a_1 + s_{22}a_2 \tag{3.41}$$

The expression for b_1 and b_2 have two terms, a reflected wave from the coupler and a wave radiated from the cavity. At the critical coupling, the amplitude of the outgoing wave $b_1 = 0$, which means that the reflected wave from the input coupler is exactly canceled by destructive interference with the wave emitted from the cavity. In this case, all the incident power is absorbed in the cavity. If the reflected wave dominates, the system is undercoupled. If the emitted wave from the cavity dominates, the system is overcoupled. We can solve the parameters s_{11} and s_{21} from Eqs. (3.40 and 3.41):

$$s_{11} = \frac{b_1 - s_{12}a_2}{a_1} \tag{3.42}$$

$$s_{21} = \frac{b_2 - s_{22}a_2}{a_1} \tag{3.43}$$

One can use a network analyzer to measure the s-parameters. By measurements, the part a_2 is usually very small and can be neglected, which means $a_2 \approx 0$. Thus, Eqs. (3.42 and 3.43) can be simplified to

$$s_{11} \approx \frac{b_1}{a_1} \tag{3.44}$$

$$s_{21} \approx \frac{b_2}{a_1} \tag{3.45}$$

We can see that s_{11} is only the ratio of the amplitudes of the reflected wave b_1 and the incoming wave a_1, and s_{21} is the ratio of the amplitudes of the transmitted wave b_2 and the incoming wave a_1. As the power is proportional to the square of the field, the S-parameters can be expressed as

$$|s_{11}| = |\frac{b_1}{a_1}| = \sqrt{\frac{P_r}{P_f}} \tag{3.46}$$

$$|s_{21}| = |\frac{b_2}{a_1}| = \sqrt{\frac{P_t}{P_f}} \tag{3.47}$$

From the equivalent circuit of a resonant-cavity system, the reflection coefficient can be expressed by the coupling strength β as

$$\Gamma = \frac{\beta - 1}{\beta + 1} \tag{3.48}$$

Furthermore, the reflection coefficient is defined as the ratio of the amplitude of the reflected voltage to the forward voltage:

$$\Gamma = \pm\frac{U_r}{U_f} = \pm\sqrt{\frac{P_r}{P_f}} \tag{3.49}$$

In general, the S-parameters are given with the units dB, so that

$$|s_{11}|[dB] = 20 \cdot lg|s_{11}| \tag{3.50}$$

$$|s_{11}|[dB] = 10 \cdot lg\frac{P_r}{P_f} \tag{3.51}$$

Combining Eqs. (3.46, 3.48, 3.49), 3.50 and 3.51, the coupling strength can be calculated and expressed with the S-parameter as

$$\beta_e = \frac{1 \pm \sqrt{10^{s_{11}(dB)/10}}}{1 \mp \sqrt{10^{s_{11}(dB)/10}}} \tag{3.52}$$

The sign depends on whether the cavity is over- or undercoupled.

If the output coupler is not small enough and the power loss P_t can not be neglected,

the quality factor Q_t is then given by

$$Q_t = Q_0 \cdot \frac{P_c}{P_t} = Q_0 \cdot \frac{P_f - P_r - P_t}{P_t} = Q_0 \cdot \frac{1 - P_r/P_f - P_t/P_f}{P_t/P_f} \tag{3.53}$$

According to the definition of β_t and Eq. (3.53), β_t can be calculated with the S-parameter by

$$\beta_t = \frac{Q_0}{Q_t} = \frac{P_t/P_f}{1 - P_r/P_f - P_t/P_f} = \frac{10^{s_{21}(dB)/10}}{1 - 10^{s_{11}(dB)/10} - 10^{s_{21}(dB)/10}} \tag{3.54}$$

Chapter 4

Skin Effect and Anomalous Skin Effect

4.1 Normal Skin Effect

Different from direct current which is evenly distributed over the cross-section of a conductor (typically in the form of wires), alternating current flows mainly in a thin layer of a conductor which is the so-called skin depth δ (see in Fig. 4.1) [13, pages 2-50][19, pages 58-78]. This phenomenon is called the skin effect.

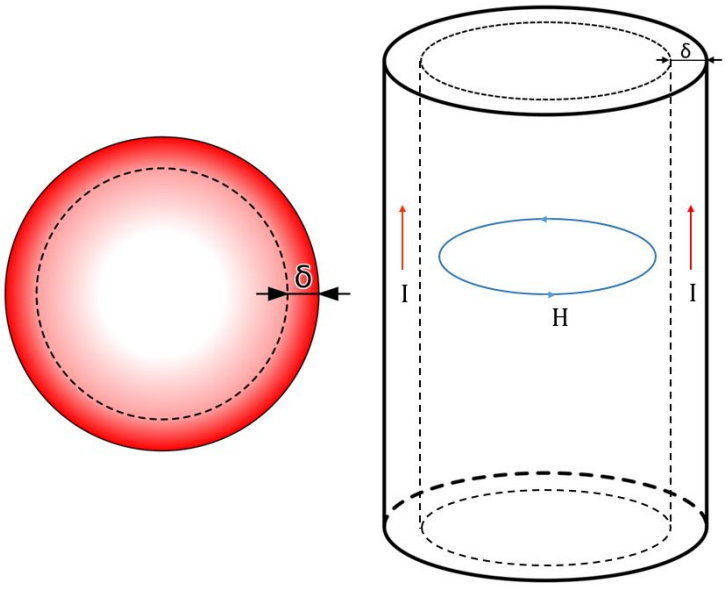

Figure 4.1: Distribution of current flow in a cylindrical conductor and cause of the skin effect.

Now we consider a semi-infinite planar conductor shown in Fig. 4.2. A plane electromagnetic wave propagates along the x-axis in the $y < 0$ space. Applying the Ampere's law to the loop S_1 and neglecting the displacement current due to the high conductivity of metal, one gets

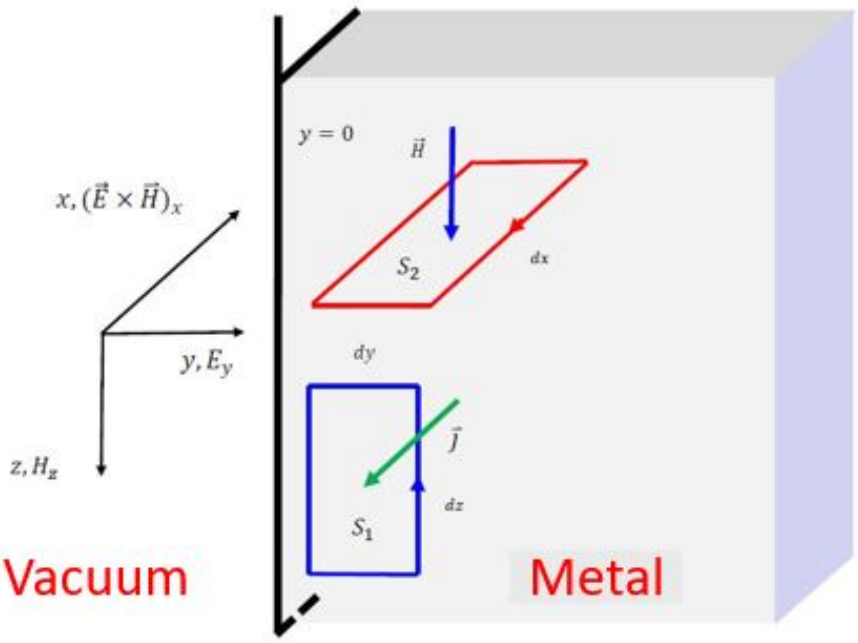

Figure 4.2: Analysis of the surface currents and fields with loops S_1 and S_2 with respect to the surface plane y=0[36].

$$\nabla \times \vec{H} = \vec{J} \tag{4.1}$$

According to the Stokes Theorem,

$$J_z(y + dy)dz - H_z(y)dz = j_x(y)dydz \tag{4.2}$$

we get

$$\frac{\partial H_z(y)}{\partial y} = j_x(y) \tag{4.3}$$

Applying the Faraday's law of induction to the loop S_2, one gets

$$\oint_{S_2} \vec{E} ds = -\frac{\partial \Phi_{S_2}}{\partial t} \tag{4.4}$$

This leads to

$$\frac{\partial E_x(y)}{\partial y} = \mu_0 \mu_r \frac{\partial H_z(y,t)}{\partial t} \tag{4.5}$$

Substituting $H_z(y,t) = H_z(y) \cdot e^{i\omega t}$ and $E_x = j_x/\rho$ into Eq. (4.5),

$$\frac{\partial j_x(y)}{\partial y} = \frac{i\omega\mu_0\mu_r}{\rho} \cdot H_z(y) \tag{4.6}$$

Partially differentiating for y in Eq. (4.6) and substituting Eq. (4.3) into the resulting equation, we get

$$\frac{\partial^2 j_x(y)}{\partial y^2} - \frac{i\omega\mu_0\mu_r}{\rho} \cdot j_x(y) = 0 \tag{4.7}$$

The general solution can be

$$j_x(y,t) = j_x(0) \cdot e^{-\sqrt{\frac{i\omega\mu_0\mu_r}{\rho}} \cdot y} + j_x(0) \cdot e^{+\sqrt{\frac{i\omega\mu_0\mu_r}{\rho}} \cdot y} \tag{4.8}$$

The second term can be neglected because it is unphysical since $j(y)$ has to vanish for $y \to \infty$. Substituting $\sqrt{i} = \sqrt{1/2} + i\sqrt{1/2}$, one obtains

$$j_x(y,t) = j_x(0) \cdot e^{-\frac{y}{\delta}} \cdot e^{-\frac{iy}{\delta}} \tag{4.9}$$

where δ is the so-called skin depth and

$$\delta = \sqrt{\frac{2\rho}{\omega\mu_0\mu_r}} \tag{4.10}$$

Substituting Eq. (4.9) into Eq. (4.3), one gets

$$H_z(y) = -\frac{\delta}{1+i} \cdot j_x(y) \tag{4.11}$$

The current I flowing in the surface can be calculated by integrating over $y > 0$ and according to Eq. (4.11), it is obtained

$$I = \int_{y=0}^{\infty} j_x(y)dy = \frac{\delta}{1+i} \cdot j_x(y) = -H_z(0). \tag{4.12}$$

4.2 Anomalous Skin Effect

Theoretically, the DC electrical resistivity ρ of copper should decrease with decreasing temperature. But in fact, as the temperature decreases to a certain value, the resistivity tends to a stable value, rather than continuing to decrease, as shown in Fig. 4.3. That's because there are defects such as grain boundaries, impurities, etc. in the material, which act as scattering sources that contribute a temperature independent ρ value at the cryogenic temperatures near absolute zero.

The parameter RRR (the residual-resistivity ratio or the residual-resistance ratio) labeled for the curves in Fig. 4.3 can just serve as a rough index of the purity and the overall quality of a sample. It can be defined for DC currents as:

$$RRR = \frac{\rho_{300K}}{\rho_{4.2K}} \tag{4.13}$$

However, for the RF case under some specific conditions, the electrical resistivity can behave with the temperature differently from the DC case shown in Fig. 4.3. It still maintains a decreasing trend with decreasing temperature, but at lower temperatures, the electrical resistivity may be significantly higher than that of direct current (DC). This phenomenon is called the anomalous skin effect. The temperature and frequency play a decisive role in whether the anomalous skin effect occurs.

If the temperature is sufficiently high, the mean free path of the conduction electrons l is smaller than the skin depth δ. All the electrons in the skin depth layer stay in this layer and contribute to the conductivity. In the momentum space, the

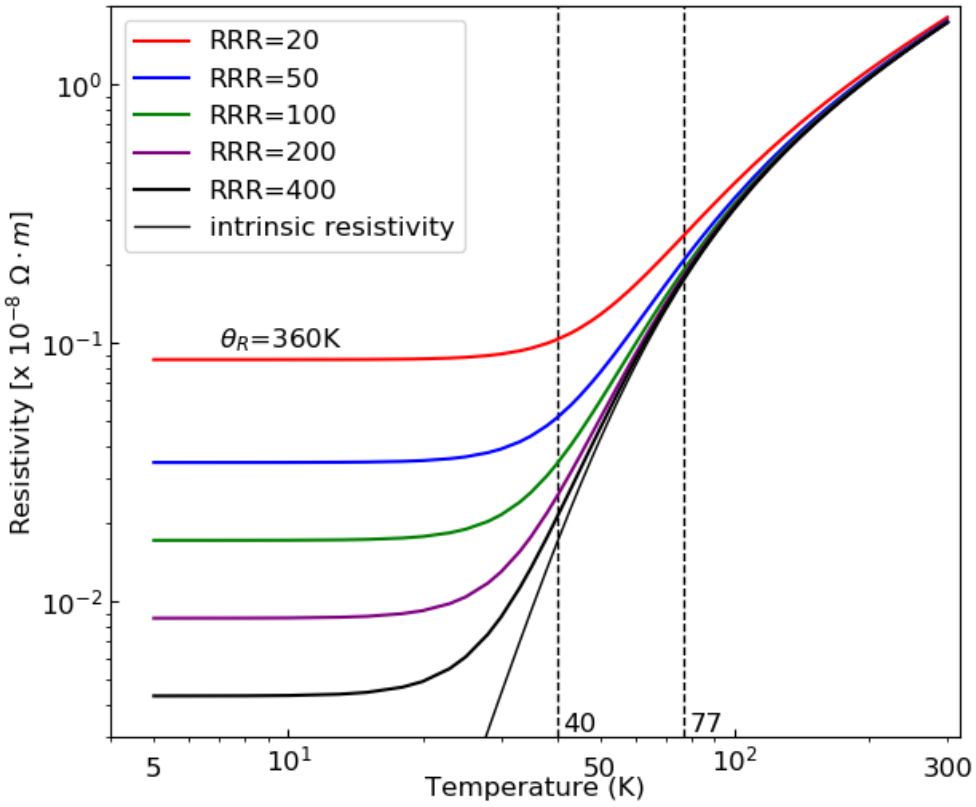

Figure 4.3: Dependence of the specific electrical resistivity in copper from its RRR - value and from temperature by applying Eq. (4.33).

Fermi surface shifts due to the applied electric field. In this case, electrons in the whole sheath (see (a) in Fig. 4.4, marked in red) contribute to the conductivity. Therefore, the anomalous skin effect will not occur. But at low temperatures there are three frequency regions to distinguish:

1. For sufficiently low frequencies: the skin depth is large compared with the mean free path and the anomalous skin effect will not occur (see (a) in Fig. 4.4).

2. For sufficiently high frequencies: in this case, the mean free path doesn't play a determining role any more because the distance traveled by an electron during one complete oscillation of the electric field is small compared to the mean free path.

3. At intermediate frequencies: the mean free path of the electrons can be com-

parable to or even considerably larger than the skin depth. Electrons whose velocity has large angels with the electric field (marked with the blue arrow by (b) in Fig. 4.4) can leave the skin depth layer and stop contributing to the RF current. Only the electrons whose velocity has small angels with the electric field (marked with the red arrow by (b) in Fig. 4.4) continue contributing to the RF current, which correspond to only a fraction of the sheath in the momentum space (see (b) in Fig. 4.4, marked in red).

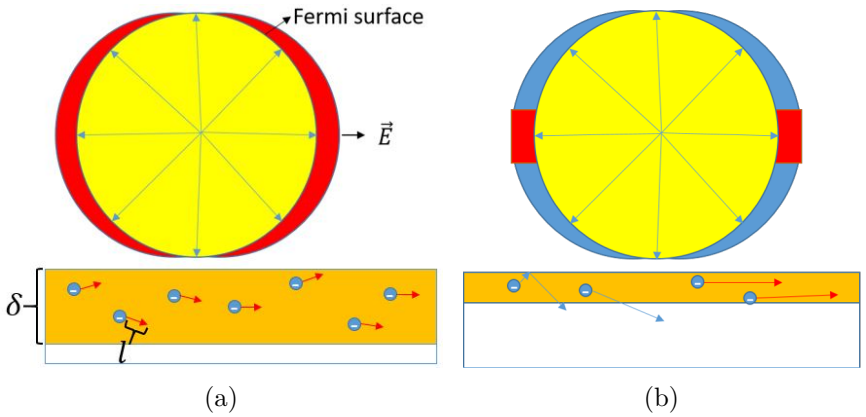

Figure 4.4: Distribution of the conduction electrons in momentum space (K-space). Only electrons in the red parts of the sheath contribute to the current. (a). Normal skin effect. (b). Anomalous skin effect.

4.2.1 The Theory of the Anomalous Skin Effect in Metal

In the classical theory, the electric field can be regarded as spatially constant for the purpose of calculating the current at a point. However, Pippard [25] pointed out that this assumption cannot be generally valid. It is certainly valid when the field does not vary appreciably over a distance of the order of the free path of the conduction electrons, which means, when the free path is small compared with the skin depth, which ($\delta = \sqrt{2\rho/\omega\mu_0\mu_r}$) is dependent on the frequency and the temperature. Different situations based on different frequencies and temperatures are discussed in Chapter 4.2.

G. E. Reuter and E. H. Sondheimer [31, 9] derived the fundamental equation using the general methods of the theory of metals without neglecting any of the terms

compared to Pippard's equation, to obtain explicit solutions over the whole frequency and temperature range. All measurable quantities can be expressed in terms of the surface impedance Z, which is defined as

$$Z = \frac{4\pi}{c}\frac{E}{H} \tag{4.14}$$

where c is the speed of light in vacuum, E and H are the electric and magnetic field strengths in parallel to the surface of the metal [32], respectively. The real part of Z is the surface resistance R and the imaginary part is the surface reactance X. Therefore, G. E. Reuter and E. H. Sondheimer focused on the derivation of the expression for Z and compared the results of Z from the theory with the experimental results for mercury (Pippard)[25]. To find Z, one needs to find the expressions of E and H at first.

We consider a semi-infinite metal with its surface in the xy-plane and the positive z-axis directed towards the interior of the metal. The electric field $E(z)e^{i\omega t}$ is along the x-direction and the magnetic field $H(z)e^{i\omega t}$ is along the y-direction. According to the Maxwell's equations

$$-\frac{dH}{dz} = \frac{i\omega}{c}E + \frac{4\pi}{c}J, \tag{4.15}$$

$$\frac{dE}{dz} = -\frac{i\omega}{c}H, \tag{4.16}$$

where J is the current density. Eliminating H from the equations, one gets the first relation between E and J:

$$\frac{d^2E}{dz^2} + \frac{\omega^2}{c^2}E = \frac{4\pi i\omega}{c^2}J. \tag{4.17}$$

To obtain the expression of E, a second relation between J and E is needed. In the theory of metallic conduction, the conduction electrons are regarded as free and the

distribution function f of the electrons is

$$f = f_0 + f_1(v, z), \tag{4.18}$$

where f_0 is the Fermi function $1/[e^{(E-\zeta)/kT} + 1]$ (ζ is the Fermi energy level), v is the velocity of an electron and f is a function fo v and z needed to be determined. The collisions of the electrons with the lattice under the action of the applied electromagnetic field will eventually reach a steady state and the distribution function of the electrons in this steady sate is determined by the Boltzmann equation[39]

$$\frac{\partial f}{\partial t} - \frac{2\pi e}{h}\left(\vec{E} + \frac{1}{c}\vec{v} \times \vec{H}\right) \cdot grad_k f + \vec{v} \cdot grad_r f = -\frac{f - f_0}{\tau} \tag{4.19}$$

where e is the electronic charge and τ is the time of relaxation of the conduction electrons.

Combining Eqs. (4.18), (4.19) and $hk = 2\pi mv$ which holds for free electrons, and neglecting the product of E with f and all the terms involving H, a differential equation for f_1 is found

$$\frac{\partial f_1}{\partial z} + \frac{1 + i\omega\tau}{\tau v_z} f_1 = \frac{e}{mv_z}\frac{\partial f_0}{\partial v_x} E(z) \tag{4.20}$$

The general solution of Eq. (4.20) is

$$f_1 = exp\left[-\frac{(1 + i\omega\tau)z}{\tau v_z}\right]\left\{F(v) + \frac{e}{mv_z}\frac{\partial f_0}{\partial v_x}\int^z E(t) exp\left[\frac{(1 + i\omega\tau)t}{\tau v_z}\right] dt\right\} \tag{4.21}$$

where $F(v)$ is a function of the velocity which is determined by the appropriate boundary condition.

For $v_z < 0$, f_1 must not become exponentially large as $z \to \infty$ which gives

$$f_1^{(1)} = -\frac{e}{mv_z}\frac{\partial f_0}{\partial v_x} exp\left[-\frac{(1 + i\omega\tau)z}{\tau v_z}\right]\int_z^\infty E(t) exp\left[\frac{(1 + i\omega\tau)t}{\tau v_z}\right] dt, \tag{4.22}$$

the superscript (1) denotes the solution of f_1 for $v_z < 0$.

The solution of f_1 for $v_z > 0$ is denoted by $f_1^{(2)}$. Assuming that a fraction p of the

electrons arriving at the surface is scattered specularly with reversal of the velocity component v_z, while the rest are scattered diffusely with complete loss of their drift velocity and $E(-z) = E(z)$, one obtains

$$\begin{aligned} f_1^{(2)} &= \frac{e}{mv_z}\frac{\partial f_0}{\partial v_x} exp\left[-\frac{(1+i\omega\tau)z}{\tau v_z}\right] \\ &\times \left\{p\int_{-\infty}^{z} E(t) exp\left[\frac{(1+i\omega\tau)t}{\tau v_z}\right]dt + (1-p)\int_0^z E(t) exp\left[\frac{(1+i\omega\tau)t}{\tau v_z}\right]dt\right\} \end{aligned} \tag{4.23}$$

Introducing spherical coordinates (v, θ, φ) in the v-space and integrating over φ, the current density $J(z)$ is obtained with E

$$\begin{aligned} J(z) =& -2e\left(\frac{m}{h}\right)^3 \int\int\int v_x f dv_x dv_y dv_z \\ & \frac{2\pi e^2 m^2 v_F^2}{h^3}\left\{p\int_{-\infty}^{\infty} k_a\left(\frac{z-t}{l}\right)E(t)dt + (1-p)\int_0^{\infty} k_a\left(\frac{z-t}{l}\right)E(t)dt\right\} \end{aligned} \tag{4.24}$$

where $a = \omega\tau$, $l = \tau v_F$, v_F is the Fermi velocity, and

$$k_a(u) = \int_0^{\frac{1}{2}\pi} sin^3\theta sec\theta e^{-(1+ia)|u|sec\theta} d\theta \tag{4.25}$$

Combining Eqs. (4.17) and (4.24), one gets the equation for E

$$\begin{aligned} \frac{d^2E}{dz^2} + \frac{\omega^2}{c^2}E =& \frac{8\pi^2 i\omega e^2 m^2 v_F^2}{c^2 h^3} \\ & \times\left\{p\int_{-\infty}^{\infty} k_a\left(\frac{z-t}{l}\right)E(t)dt + (1-p)\int_0^{\infty} k_a\left(\frac{z-t}{l}\right)E(t)dt\right\} \end{aligned} \tag{4.26}$$

Introducing dimensionless coordinates $x = z/l, y = t/l$, and writing $E(lx) = g(x)$, Eq. (4.26) can be expressed as

$$g''(x) + \frac{\omega^2 l^2}{c^2}g(x) = i\alpha\left\{p\int_{-\infty}^{\infty} k_a(x-y)\,g(y)dy + (1-p)\int_0^{\infty} k_a(x-y)\,g(y)dy\right\}, \tag{4.27}$$

where

$$\alpha = 8\pi^2\omega e^2 m^2 v_F^2 l^3/(c^2h^3) = \frac{3}{2}l^2/\delta^2. \tag{4.28}$$

with

$$\delta = c/\sqrt{2\pi\omega\sigma}, \quad n = \frac{8\pi}{3}\left(\frac{mv_F}{h}^3\right), \quad \sigma = \frac{ne^2l}{mv_F} \tag{4.29}$$

where δ is the skin depth, n the density of electrons per unit volume and σ the D.C. conductivity.

Since the surface impedance Z can be obtained by

$$Z = \frac{4\pi}{c}\frac{E(0)}{H(0)} = -\frac{4\pi i\omega l}{c^2}\frac{g(0)}{g'(0)}, \tag{4.30}$$

one doesn't need to know $g(x)$ explicitly. The general expressions of $g(x)$ and $g(0)/g'(0)$, and the applications are described in [31].

4.3 Estimation of the Anomalous Skin Effect in Microwave Cavity Walls by a "Geometric Model"

Models about the anomalous skin effect were developed from the beginning for a full range of frequencies – up to the optical spectrum. H. London made the suggestion, that a reduced conductivity might be due to the mean free path of electrons - when becoming longer than the skin depth in metal surfaces. Mathematical models based on the so-called diffusion model were developed and experimentally tested by A.B. Pippard[25] and others like G.E. Reuter, E.H. Sondheimer, R.G. Chambers [31, 9]. The theory is valid over a wide range of frequencies.

These descriptions were successful and have been proven experimentally. However, the RF experiments show reduced performance against the theoretical predictions in many cases. This gave the motivation to describe this effect for the Microwave Regime up to around 2.5 GHz in a more transparent way, and to be focused on the change in wall resistance, as this is the most important parameter in usual applications. A "geometric model" is developed, where a well-defined starting condition for the 6-D phase space distribution of electrons is exactly solved with respect to the percentage of electrons, which are leaving the skin sheath within their free path length between two collisions and collision time τ.

The upper frequency limit for this model at around 2.5 GHz is set by the condition $\omega\tau \ll 1$, which is to be fulfilled at all temperatures. At higher frequencies, the influence of the anomalous skin effect is on one hand overestimated by this model, as the shorter RF period results in a lower loss probability of current carrying electrons. On the other hand, the influence is underestimated as small angle scattering will play the main role under these conditions.

4.3.1 Assumptions for the Geometric Model

The main parameters of copper are introduced from the beginning to make the assumptions clear by numerical cross-checks. However, the model can be applied to other "simple" metals as well by adapting those parameters.

Table 4.1: Key parameters for copper.

Fermi-energy E_F/eV	7.0
Fermi-velocity $v_F/m/s$	$1.57 \cdot 10^6$
Free electron density n_e/m^{-3}	$8.5 \cdot 10^{28}$
Electron mass mc^2/keV	511
Parameters at 293 K:	
Spec. electr. resistivity $\rho_n/\Omega m$	$1.7 \cdot 10^{-8}$
El. Conductivity $\sigma_n/S/m$	$5.9 \cdot 10^7$

From now onwards, temperature dependent parameters contributing to the anomalous skin effect are denoted by an index a like σ_a, ρ_a, δ_a, while parameters at room temperature are denoted by an index n. Parameters from the normal skin effect theory are denoted by index c like δ_c.

From the parameters in Table 4.1 the collision time τ_n and the mean free path l_n at 293 K can be derived classically:

$$\sigma_n = \frac{n_e e^2 \tau_n}{m} \tag{4.31}$$

This results in

$$\tau_n = 2.46 \cdot 10^{-14} s \tag{5.4a}$$

and in a mean free electron path length of

$$l_n = v_F \cdot \tau_n = 3.9 \cdot 10^{-8} m = 0.039 \mu m. \tag{5.4b}$$

It means, that τ is very short against the RF period T. The "normal" skin depth in copper at 293 K and at 340 MHz equals to:

$$\delta_n = \sqrt{\frac{2}{\omega \cdot \mu_0 \cdot \sigma_n}} = 6.56 \cdot 10^{-2} \cdot f^{-1/2} = 3.56 \mu m. \tag{4.32}$$

No anomalous skin effect will happen at room temperature operation as δ is by two orders in magnitude larger than the mean free electron path. However, the free path is increasing proportionally to $\sigma(T)$ and the skin depth is reduced with $\sigma(T)^{-1/2}$. It becomes clear from Fig. 4.3, that at some temperature the skin depth will be shorter then $l(T)$, and the anomalous skin effect will become an issue, as soon as the RRR – values of the copper surface are high enough. The temperature dependence of the electric specific resistance is described by Matthiessen's Rule with the Bloch-Grüneisen equation for the intrinsic resistivity of a metal[20], which in case of copper reads

$$\rho(T) = \rho_R + \rho_i = \frac{\rho(300K)}{RRR} + 4.226 \cdot \left(\frac{T}{\theta_R}\right)^5 \cdot \rho_\theta(T) \cdot \int_0^{\theta_R/T} \frac{x^5}{(e^x - 1)(1 - e^{-x})} dx \tag{4.33}$$

where θ_R is the Debye temperature and ρ_θ is the electrical resistivity at the Debye temperature.

A realistic RRR-value for larger quantities of deliverable material is RRR=400 for OF-Cu, DIN 2.0040 in Europe, C10100 in USA. For envisaged operation temperatures at and above 40 K, RRR – values around 300 are sufficient (compare Fig. 4.3). This results in

$$\sigma(4.2K) = 1.77 \cdot 10^{10} S/m; \quad \tau(4.2K) = 7.38 \cdot 10^{-12} s; \quad l(4.2K) = 11.7 \mu m. \tag{4.34}$$

Compared to the corresponding electron collision rate of down to 135 GHz at 4.2 K, one can conclude, that up to around 2.5 GHz, the electron collision rate at low

temperature is still high against the RF period.

The following assumptions are made for the geometric model:

- The cavity surface is locally described as a plane perpendicular to the y – axis
- The tangential H-field is along the x-direction, the corresponding RF current along the z-direction
- The RF current density is constant across the skin layer and zero beyond (equivalent conductive layer model[40] and Fig. 4.5, resulting in a correct classical surface resistance)
- Electrons hitting the surface are assumed
  - to show specular reflection (p=1)
  - to be completely diffusely reflected (p=0)

  Both cases are compared with measurements to find an according description finally
- A Fermi – Dirac distribution at 0 K for the electrons is assumed. This sphere is displaced by Δv_F when electric surface current is transported
- Electrons stop contributing to the RF current as soon as they leave the skin layer along their free path between two collisions
- Electron losses within a given velocity space will be partly compensated by electrons accelerated from the core into the available states

Assumption 3 is visualized by Fig. 4.5. The current-density distribution across the conducting metal sheath (ref. [18]) is plotted at $\varphi = 0, -\pi/4$ (corresponding to the maximum in surface current), and $-\pi/2$. The according θ-functions describing the equivalent skin model at those phases are plotted as well. Current density:

$$j_z(y,\varphi) = \sqrt{2} \cdot H_{0,x}/\delta \cdot e^{-y/\delta} \cdot cos(y/\delta + \varphi); \quad \varphi = 3\pi/4 - \omega t; \quad y \geq 0. \tag{4.35}$$

Integration over y results in the surface current $\kappa_z(t) = -H_x(t) = -H_{0,x} \cdot cos(\omega t)$.

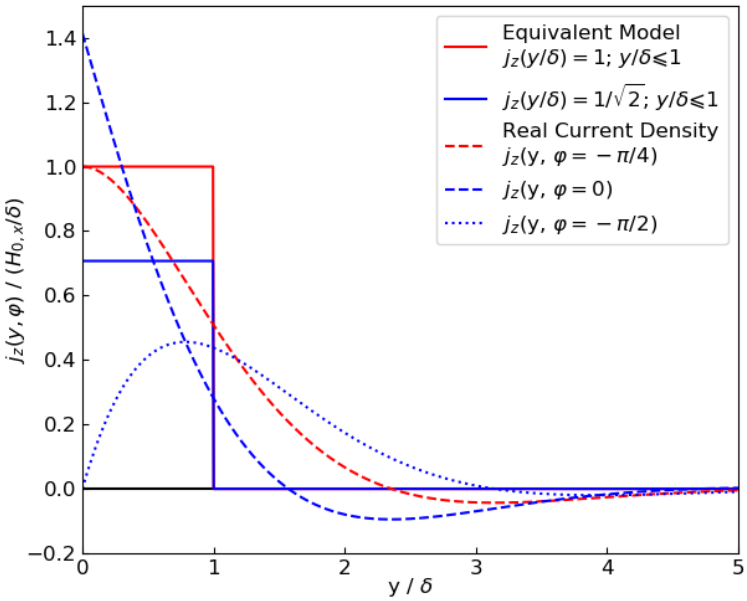

Figure 4.5: Current density amplitude across the conducting sheath according to the normal skin effect and to the equivalent model [40] assumption. The red curves correspond to the field maximum , while the blue curves are relevant to the situation ±45° before and after the maximum.

Equivalent surface-current model:

$$j_z(y,t) = -H_{0,x}/\delta \cdot cos(\omega t); 0 \leq y \leq \delta \tag{4.36}$$

and elsewhere $j_z(y,t) = 0$. $H_{0,x} \equiv$ Tangential magnetic surface field amplitude. (Coordinates like in Fig. 4.6, but the y-axis in Eqs. (4.35, 4.36) is oriented into the metal, and y=0 corresponds to the metal surface.)

With respect to assumption 4, it was stated by Refs. [25, 31, 9], that any assumption on the reflection mechanism makes no significant change in the surface resistance (the graphs show up to about 20% difference). In this paper, like in Ref. [31], a transition from lower to higher p-values with decreasing temperature is suggested and justified with a decreasing scattering angle. Best fits to measurements are resulting from that concept.

A consequence from assumptions 5 and 6 is, that details of small angle scattering are not considered here. This agrees to literature, where the electric resistance

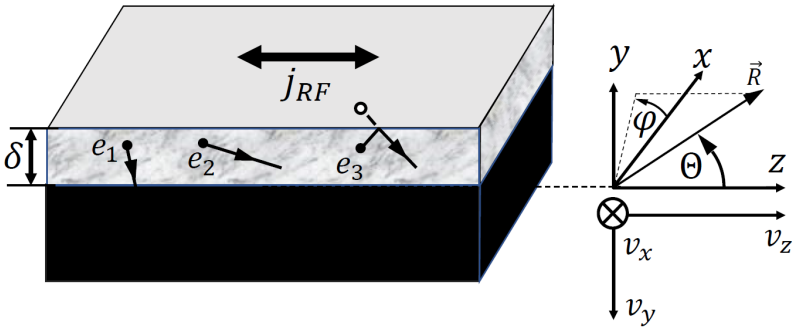

Figure 4.6: Orientation of the skin layer, the RF current and the coordinate systems to calculate the anomalous skin effect. The metal surface corresponds to $y = \delta$. Additionally, paths of electrons are shown, e_3 is an example for specular reflection..

at lower temperatures is mainly attributed to Umklapp-scattering processes with phonons [3], which change the electron path direction significantly in one step. The mean free path concept and the insertion into the free electron equation of motion is copied to add the anomalous losses.

Though the thermal excitations at the Fermi-surface are relatively large (meV) when compared to the shift of the Fermi – surface by the RF currents (μeV), statistically the localization of the electrons in phase space contributing to the surface currents are very well described by this model. The authors of the diffusion model already demonstrated very well, that details of the individual Fermi-surfaces of most common metallic conductors are not important to describe quantitatively the anomalous skin effect. Instead, the free electron model is sufficient.

The quality factor of a cavity is proportional to δ^{-1} at a given geometry[18]:

$$Q = g \cdot \frac{V}{A \cdot \delta} \tag{4.37}$$

The geometric factor g is due to the individual cavity geometry. From a measured $Q(T)$ at a temperature T, one can derive $\delta(T)$, and by that parameter gets access to the conductivity. However, the RF conductivity is reduced against its DC-value as soon as the anomalous skin effect is contributing.

This conductivity reduction at each temperature will be derived now by applying the geometric model. At an operation temperature T, the **D**irect **C**urrent DC-

conductivity reads

$$\sigma(T) = \frac{n_e e^2 \tau(T)}{m}. \tag{4.38a}$$

The free conducting electron motion along z at AC frequency ω is described by:

$$m\dot{v}_z + m\frac{v_z}{\tau} = -e \cdot E_z, \tag{4.36b}$$

$$m \cdot \left(\frac{1}{\tau} + i\omega\right) v_z = e \cdot E_z \tag{4.36c}$$

$$j_z = -n_e \cdot e \cdot v_z = \sigma \cdot E_z. \tag{4.36d}$$

This results in

$$\sigma = \frac{n_e \cdot e^2 \cdot \tau \cdot (1 - i\omega\tau)}{m \cdot (1 + \omega^2\tau^2)} \rightarrow \frac{n_e \cdot e^2 \cdot \tau}{m} \text{for} f \leq 2.5GHz \tag{4.36e}$$

That means, the DC conductivity can be used as a good approximation within that frequency range and for RRR-values as discussed above. Δv_F in Eq. (4.36d) is illustrated in Fig. 4.7 and describes the shift of the Fermi-sphere in an electric field.

However, the RF surface conductivity $\sigma_a(T)$ will be reduced, with consequences for the skin depth:

$$\delta_a(T) = \sqrt{\frac{2}{\omega \cdot \mu_0 \cdot \sigma_a(T)}}. \tag{4.39}$$

The reason are electrons with a velocity component in y-direction, large enough to leave the skin layer between two collisions. By that they lose contact with the RF fields and get out of phase.

It is useful to define the following parameters:

$$h_l = \frac{\delta_a(T)}{l(T)} = \sqrt{\frac{2}{\omega \cdot \mu_0 \cdot \sigma_a(T)}} \cdot \frac{n_e \cdot e^2}{v_F \cdot \sigma(T) \cdot m_e} = \frac{7.7 \cdot 10^{17}}{(\sigma_a(T))^{1/2} \cdot \sigma(T) \cdot f^{1/2}}$$
$$= \frac{(\sigma_n)^{3/2}}{\sigma(T) \cdot (\sigma_a(T))^{1/2}} \cdot \frac{1.7 \cdot 10^6}{f^{1/2}}. \tag{4.40a}$$

$$h_0 = \frac{\delta_c(T)}{l(T)} = \frac{(\sigma_n)^{3/2}}{(\sigma(T))^{3/2}} \cdot \frac{1.7 \cdot 10^6}{f^{1/2}} \tag{4.40b}$$

$$q_0 = \frac{(\sigma_n)^{3/2}}{(\sigma_a(T))^{3/2}} \cdot \frac{1.7 \cdot 10^6}{f^{1/2}} \tag{4.40c}$$

$\delta_c(T)$ in Eq. (4.40b) denotes the classical skin depth.

4.3.2 Conducting Electrons in Velocity Space

When RF current is flowing, the current carrying electrons in velocity space are those within the hemispherical shell as sketched in Fig. 4.7. All other electrons cancel each other as they have a partner which exactly carries the opposite momentum. At first, the integral in momentum space over this shell is carried out. The occupation probability 1 is taken as is valid at temperature 0 K for the Fermi-Dirac-distribution. Δv_F in Fig. 4.7 corresponds to v_z in Eqs. (4.36b, 4.36c) and is very small against v_F, which denotes the Fermi–velocity.

The relative current density contribution in local space from a solid angle element $d\Omega$ at Θ in electron velocity space varies then (see Fig. 4.7) with

$$dn_c(\Omega) \sim 2\Delta v_F \cdot v_F^2 \cdot cos\Theta \cdot d\Omega. \tag{4.41}$$

Each electron in the conducting half shell contributes to the current density j_z proportionally to its velocity $v_z = v_F \cdot cos\Theta$.

The current density as used in Eq. (4.36d) results then by integration over the

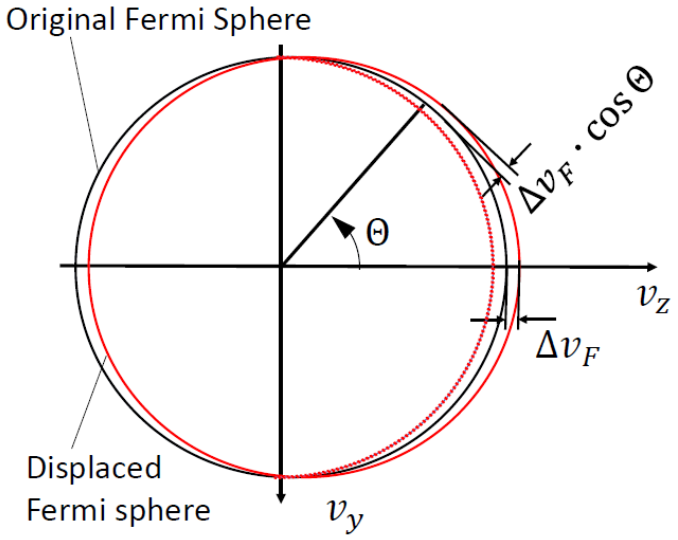

Figure 4.7: Conducting sheath (between shifted spheres) with maximum thickness $2\Delta v_F$ in z–direction. For convenience, v_y is oriented in y-direction.

velocity space of contributing electrons:

$$j_{z,tot} \sim e \cdot \int_{\Theta=0}^{\pi/2} \int_{\varphi=0}^{2\pi} v_z(\Omega) dn_c(\Omega) d\Omega \tag{4.42}$$

and by including the geometric parameters of the shell:

$$j_{z,tot} \sim e \cdot 2\Delta v_F \cdot v_F^3 \cdot \int_0^{\frac{\pi}{2}} \int_0^{2\pi} cos^2\Theta sin\Theta d\Theta d\varphi$$

$$j_{z,tot} \sim -e \cdot 4\pi \cdot \Delta v_F \cdot v_F^3 \cdot \frac{1}{3} \cdot cos^3\Theta|_0^{\pi/2}$$

$$j_{z,tot} \sim \frac{4\pi}{3} \cdot e \cdot \Delta v_F \cdot v_F^3. \tag{4.43}$$

For simplification in the next step, this integration is projected into the $v_x v_y$–plane: There, the conducting sheath Δv_z has a constant thickness $2\Delta v_F$. However, the $cos\Theta$ - dependence of v_z has to be adapted.

The integration is now performed along the coordinates $u = v_x/v_F$, $w = v_y/v_F$,

for the circular area. The integral reads then

$$j_{z,tot} \sim e \cdot 2\Delta v_F \cdot v_F^3 \cdot \int_{-1}^{1} \int_{-(1-w^2)^{1/2}}^{(1-w^2)^{1/2}} (1-u^2-w^2)^{1/2} dw du, \tag{4.44}$$

giving a result identical to Eq. 4.43.

4.3.3 Fraction of Lost RF Conduction Electrons in a y-plane within the Skin Sheath

The anomalous skin effect is due to electrons within the current carrying sheath, which have a v_y-component and are able to leave the skin depth. By diving deeper into the metal their connection and response to the RF fields is lost.

As soon as the electron mean free path comes close to the skin depth the anomalous skin effect will appear.

In local space the position $y = 0$ marks the bottom of the skin layer. At a (positive) position y within the skin layer, an electron will be "lost" as soon as it has a velocity component v_y high enough to pass the projected length y within the collision time $\tau(T)$. Alternatively, an electron at position y will be lost after specular reflection at the metal surface as soon as it has a negative velocity component v_y, high enough to transit a projected path length $\Delta y = 2\delta - y$ within τ. The same result is received, when these electrons are started at $y' = 2\delta - y$ with velocity v_y (Note: Positive v_y are directed antiparallel to the y–axis).

In case of completely diffuse reflection, electrons are lost for RF conductivity in the same way as soon as they reach the upper or lower boundary of the skin sheath. The loss contribution from the positive v_y-velocity space is then identical with the negative one and the first one will be just multiplied by two to get the full result.

The loss condition for an RF current carrying electron at y is then

$$y < v_y \cdot \tau(T), \tag{4.45}$$

y will run from 0 to δ for diffuse reflection and up to 2δ for specular reflection. In the normalized velocity space the integration limits are $0 \leq w \leq 1$, $-(1-w^2)^{1/2} \leq$

$u \leq (1 - w^2)^{1/2}$. With

$$v_y = v_F \cdot sin\Theta \cdot sin\varphi = v_F \cdot w \tag{4.46a}$$

the loss condition finally reads

$$y < v_F \cdot w \cdot \tau(T) \tag{4.46b}$$

$$w > h(T,y) \quad \text{with} \tag{4.46c}$$

with

$$h(T, y) \equiv h = \frac{y}{v_F \cdot \tau(T)} = \frac{y}{l(T)} \tag{4.47}$$

With Eq. (4.38a) one gets

$$h = \frac{y \cdot n_e \cdot e^2 \cdot c^2}{v_F \cdot \sigma \cdot mc^2}. \tag{4.48}$$

For copper with v_F, n_e as given above it results in

$$h = 1.53 \cdot 10^{15} \cdot \frac{y}{\sigma}. \tag{4.49}$$

Finally, with Eqs. (4.45) and (4.49) the condition for anomalous losses in copper at depth y is

$$w > 1.53 \cdot 10^{15} \cdot \frac{y}{\sigma}; \quad 0 < y < \delta(\text{diffuse refl.}), \quad 0 < y < 2\delta(\text{specular refl.}) \tag{4.50}$$

As a first task, the percentage of reduced RF conductivity in z–direction at a given h – that means in a given y–plane $0 < y < \delta(2\delta)$ – has to be calculated. The conductivity is reduced by the anomalous skin effect as soon as $h(T, y) < 1$. This is illustrated by Fig. 4.8.

Within a given loss angle around Θ, φ, the loss time is given by (see Eqs. (4.45,

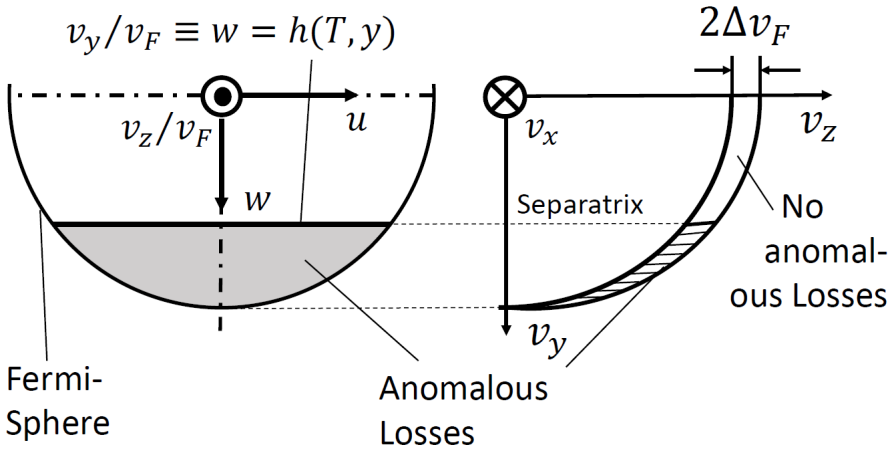

Figure 4.8: Illustration of the separatrix between fully conducting (white) and reduced conducting electron surfaces (shaded) in velocity space at a position y and $h \equiv y/l$, respectively. View on the Fermi surface (left) and cut through one quadrant of the Fermi -Sphere (right). The upper half shell in velocity space is mirrored to positive v_y for easier calculation of anomalous losses (compare Fig. 4.6).

4.46a))

$$\Delta t = \frac{y}{v_y} = \frac{y}{v_F \cdot sin\Theta \sin\varphi} = \frac{h \cdot \tau}{sin\Theta sin\varphi} = \frac{h \cdot \tau}{w}. \tag{4.51}$$

Including this loss mechanism in Eq. (4.36b) one gets

$$m\dot{v_z} + m\frac{v_z}{\tau} + m\frac{v_z}{\Delta t} = -e \cdot E_z \tag{4.52}$$

and in equilibrium (same approximation as in Eq. (4.38))

$$m\frac{v_z}{\tau} + m\frac{v_z}{\Delta t} = -e \cdot E_z$$

$$mv_z\frac{\tau + \Delta t}{\tau \cdot \Delta t} = -e \cdot E_z$$

$$m \cdot \frac{v_z}{\tau'} = -e \cdot E_z \tag{4.53}$$

with

$$\tau' = \frac{\tau \cdot \Delta t}{\tau + \Delta t} = \tau \frac{h}{w+h} \tag{4.54}$$

This results in a reduced local conducting electron sheath thickness in velocity phase space:

$$2\Delta v_z'(h,w) = 2\Delta v_F \cdot \frac{\tau'}{\tau} = 2\Delta v_F \frac{h}{w+h}, \text{if} \quad h(T,y) < 1 \tag{4.55}$$

with $w = v_y/v_F$ as introduced before.

The resulting conductivity at the layer $h = y/l$ within the skin sheath is calculated for positive w by repeating the integration in velocity space like in Eq. (4.44), but with replacing the constant Δv_F by $\Delta v_z'(w)$ within the range $h \leq w \leq 1, h < 1$, and adding the loss free part in the velocity range $0 \leq w < h, h < 1$:

$$j_{z,1}'(h) \sim e \cdot 2\Delta v_F \cdot v_F^3 \cdot \int_h^1 \int_{-(1-w^2)^{1/2}}^{(1-w^2)^{1/2}} (1-u^2-w^2)^{1/2} \cdot \frac{h}{w+h} du dw, \tag{4.56a}$$

$$j_{z,1}'(h) \sim e \cdot \Delta v_F \cdot v_F^3 \cdot \pi \left[-\frac{h^3}{2} + h^2 - \frac{h}{2} + (h-h^3) \cdot ln(h+1) - (h-h^3) \cdot ln(2h) \right]. \tag{4.56b}$$

The loss-free part within $h < 1$ is

$$j_{z,2}'(h) \sim e \cdot 2\Delta v_F \cdot v_F^3 \cdot \int_0^h \int_{-(1-w^2)^{1/2}}^{(1-w^2)^{1/2}} (1-u^2-w^2)^{1/2} du dw, \tag{4.56c}$$

$$j_{z,2}'(h) \sim e \cdot \Delta v_F \cdot v_F^3 \cdot \pi \left[h - \frac{h^3}{3} \right] \tag{4.56d}$$

The completely loss-free zones in case of $h \geq 1$ are contributing to the current den-sity as

$$j_{z,3}'(h) \sim e \cdot 2\Delta v_F \cdot v_F^3 \cdot \int_0^1 \int_{-(1-w^2)^{1/2}}^{(1-w^2)^{1/2}} (1-u^2-w^2)^{1/2} du dw = \frac{2}{3} \pi e \Delta v_F v_F^3. \tag{4.56e}$$

4.3.4 Reduced RF conductivity within the skin sheath

The two cases "specular reflection with $p = 1$" and "diffuse reflection with $p = 0$" are considered separately at first. The integration over h is applied on Eqs. (4.56b, 4.56d and 4.56e).

In the specular case, the integration is from $h = 0up$ to $2h_0 = 2\delta/l$ for including the velocity space with negative starting values for v_y (see Fig. 4.9).

In case of diffuse reflection, as mentioned before the conductivity calculated for positive v_y is just multiplied by a factor two, the h-integration is from 0 to $h_0 = \delta/l$ (see Fig. 4.9).

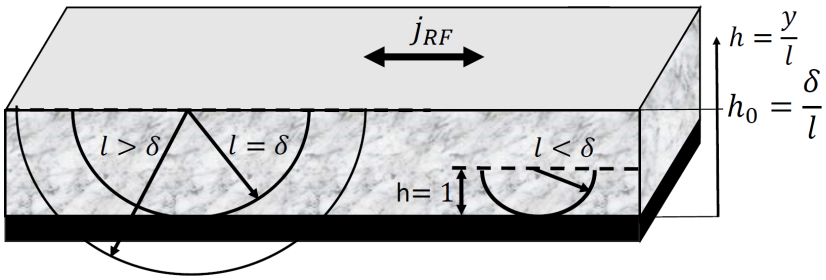

Figure 4.9: Illustration of different electron free path length cases and of a reduced loss region up to $h < 1$ only for $l < \delta$.

Case 1, Specular reflection, $p = 1$:

Two regions have to be distinguished:

Region 1: For $2h_0 < 1$ losses will occur for all h and the integration is performed over the whole h-range:

$$j_{z,a1} \sim e \cdot \pi \cdot \Delta v_F \cdot v_F^3 \cdot \frac{1}{h_0} \left[\int_0^{2h_0} j'_{z,1}(h) \cdot dh + \int_0^{2h_0} j'_{z,2}(h) \cdot dh \right], \tag{4.57a}$$

This result is

$$j_{z,a1} \sim \frac{4\pi}{3} \cdot e \cdot v_F^3 \cdot \Delta v_F \cdot F_{s1}(h_0) \tag{4.57b}$$

with

$$F_{s1}(h_0) = 0.375 - 0.95445h_0 + 1.5h_0^2 + 1.6587h_0^3$$
$$+ln(1+2h_0)\cdot(1.5H_0 - 3h_0^3 - 0.1875h_0^{-1}) + ln(h_0)\cdot(3h_0^3 - 1.5h_0) \quad (4.57c)$$

Region 2: $2h_0 \geq 1$

$$j_{z,a1} \sim e{\cdot}\pi{\cdot}\Delta v_F{\cdot}v_F^3{\cdot}\frac{1}{h_0}\left[\int_0^1 j'_{z,1}(h)\cdot dh + \int_0^1 j'_{z,2}(h)\cdot dh + \int_1^{2h_0} j'_{z,3}(h)\cdot dh\right], \quad (4.57d)$$

This results in

$$j_{z,a1} \sim \frac{4\pi}{3}\cdot e\cdot v_F^3\cdot\Delta v_F\cdot F_{s2}(h_0) \quad (4.57e)$$

with

$$F_{s2}(h_0) = 1.0 - 0.1299\cdot h_0^{-1} \quad (4.57f)$$

Case 2, Diffuse reflection, $p = 0$:

Region 1, $h_0 < 1$:

$$j_{z,a1} \sim e\cdot\pi\cdot\Delta v_F\cdot v_F^3\cdot\frac{1}{h_0}\left[\int_0^{h_0} j'_{z,1}(h)\cdot dh + \int_0^{h_0} j'_{z,2}(h)\cdot dh\right], \quad (4.58a)$$

$$j_{z,a1} \sim \frac{4\pi}{3}\cdot e\cdot v_F^3\cdot\Delta v_F\cdot F_{d1}(h_0) \quad (4.58b)$$

with

$$F_{d1}(h_0) \quad = 0.375 + 0.0426h_0 + 0.375h_0^2 - 0.0525h_0^3 - ln(1+h_0)\cdot(0.375h_0^3$$
$$-0.75h_0 + 0.375h_0^{-1}) + ln(h_0)\cdot(0.375h_0^3 - 0.75h_0) \quad (4.58c)$$

Region 2: $h_0 \geq 1$

$$j_{z,a1} \sim e{\cdot}\pi{\cdot}\Delta v_F{\cdot}v_F^3{\cdot}\frac{1}{h_0}\left[\int_0^1 j'_{z,1}(h)\cdot dh + \int_0^1 j'_{z,2}(h)\cdot dh + \int_1^{h_0} j'_{z,3}(h)\cdot dh\right], \quad (4.58d)$$

This results in

$$j_{z,a1} \sim \frac{4\pi}{3}\cdot e\cdot v_F^3\cdot\Delta v_F\cdot F_{d2}(h_0) \quad (4.58e)$$

with

$$F_{d2}(h_0) = 1.0 - 0.2598\cdot h_0^{-1} \quad (4.58f)$$

The anomalous conductivity at that stage is given by (see Eq. (4.43) for $j_{z,tot}$)

$$\sigma_{a,1} = \sigma\cdot\frac{j_{z,a1}}{j_{z,tot}} = \sigma\cdot F(h_0); \quad (4.59)$$

and has to be chosen accordingly for the 4 different cases for F as defined above.

If a measured DC function $\sigma(T)$ exists, one can apply the geometric model by calculating an h_0 with Eq. (4.40b). With h_0 inserted in functions $F_{m1,2}$ or $F_{d1,2}$, in the following denoted by F, one gets $\sigma_{a,1}$. However, due to reduced RF conductivity the skin depth has to become larger, resulting in an $h_1 > h_0$. This leads to a recursion formula with the starting DC value $\sigma \equiv \sigma(T)$:

$$\sigma_{a,0} = \sigma; \quad \sigma_{a,1} = \sigma\cdot F(h_0); \quad \sigma_{a,2} = \sigma\cdot F(h_1); ... \quad \text{with} \quad F(h_{-1}) = 1 \quad (4.60a)$$

The relation between neighbor-elements of the sequence is

$$\sigma_{a,i}/\sigma_{a,i-1} = \frac{F(h_{i-1})}{F(h_{i-2})}; \quad i \geq 1. \quad (4.60b)$$

For the h_i one gets from the starting condition $\sigma_{a,0} = \sigma$, and from Eq. (4.40a)

$$h_i = h_{i-1}\cdot\left(\frac{\sigma_{a,i-1}}{\sigma_{a,i}}\right)^{1/2}; \quad i \geq 1. \quad (4.60c)$$

Insertion of Eq. (4.60b) gives the recursion formula for h:

$$h_i = h_{i-1} \cdot \left(\frac{F(h_{i-2})}{F(h_{i-1})} \right)^{1/2} ; \quad i \geq 1, \tag{4.60d}$$

$F(h_i)$ is calculated by insertion of h_i into the according F-function (4.57c, 4.57f, 4.58c, 4.58f), respectively.

The sequence will converge to an h_l for every starting value h_0, with $h_0 > 0$. With $F(h_l)$ one finally gets the anomalous conductivity

$$\sigma_a = \sigma \cdot F_l(h_0) \tag{4.61}$$

with $h_l = \lim_{i \to \infty} h_i$, $\quad F_l(h_0) \equiv F(h_l)$ for a given starting value h_0.

The starting functions $F(h_0)$ and the final functions $F_l(h_0)$ are shown in Fig. 4.10 for the most relevant h_0 range. Another plot for a larger range of h_0 is shown in Fig. 4.11.

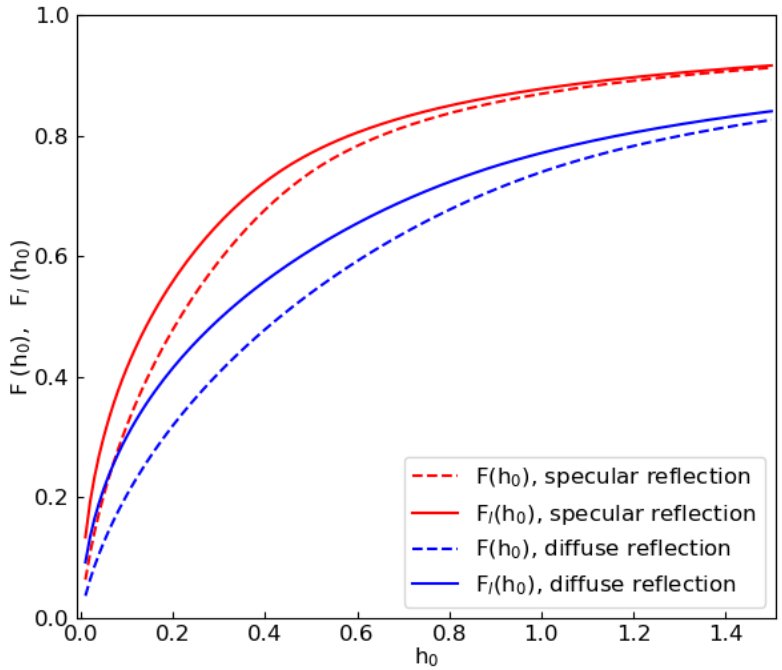

Figure 4.10: Plot of $F(h_0)$- and $F_l(h_0)$-functions for specular and diffuse reflection, $0.01 \leq h_0 \leq 1.5$.

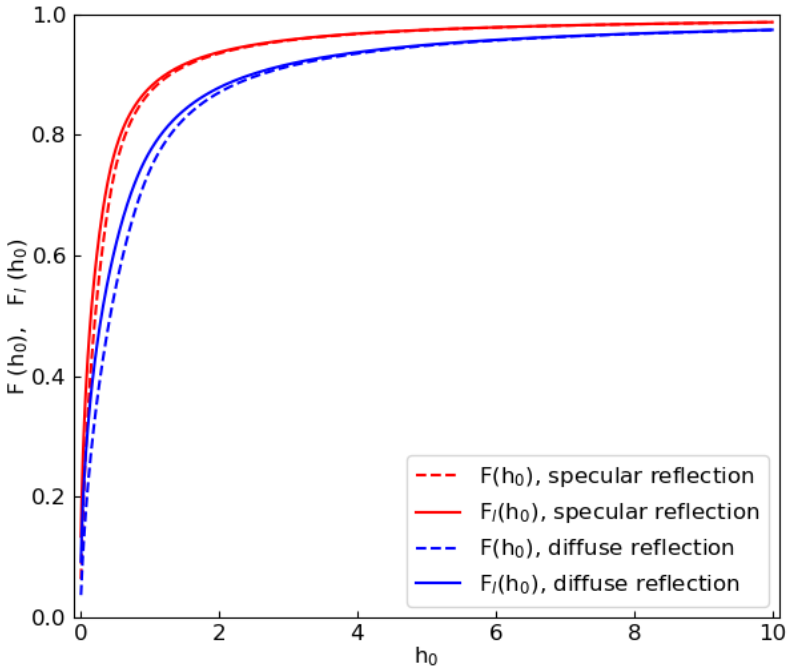

Figure 4.11: Plot of $F(h_0)$- and $F_l(h_0)$-functions for specular and diffuse reflection, $0.01 \leq h_0 \leq 10$.

One should also find the effective DC-conductivity $\sigma(T)$ of an unknown copper quality in case of RF measurements providing $\sigma_a(T)$: As mentioned in many publications (see for example Refs. [25, 31, 9]), the RRR-value is very sensitive to manufacturing steps and annealing processes. Therefore, one needs to develop also the reversed calculation process, as described in the following.

h is now called q for a better distinction. The starting values q_0 for copper in that case are defined in Eq. (4.40c). Comparison with Eq. (4.40a) and getting $\sigma(T)$ in the denominator by starting with $\sigma_a(T)$ one gets now

$$\sigma_0 = \sigma_a(T); \quad \sigma_1 = \frac{\sigma_0}{F(q_0)}; \quad \sigma_2 = \frac{\sigma_0}{F(q_1)}; \ldots \quad \text{with} \quad F(q_1) = 1. \tag{4.62a}$$

$$\sigma_i = \frac{\sigma_0}{F(q_{i-1})}; \frac{\sigma_{i+1}}{\sigma_i} = \frac{F(q_{i-1})}{F(q_i)}; i \geq 1, \tag{4.62b}$$

$$q_i = q_{i-1} \cdot \frac{\sigma_{i-1}}{\sigma_i} \quad \text{from Eq. (4.40a)} \tag{4.62c}$$

$$q_i = q_{i-1} \cdot \frac{F(q_{i-1})}{F(q_{i-2})}; \quad i \geq 1, \tag{4.62d}$$

$F(q_i)$ is calculated by insertion of q_i into the according F-function (4.57c, 4.57f, 4.58c, 4.58f) - for regions 1 and 2. The transition between both regions is again at $q_0 = 1$.

The recursion will converge to a finite limit q_l for every starting value q_0, with $q_0 > 0$. With this value and $F(q_l)$ one finally gets the DC-conductivity

$$\sigma \cong \sigma_a / F_l(q_0), \tag{4.63}$$

with $q_l = \lim_{i \to \infty} q_i, \quad F_l(q_0) \equiv F(q_l)$ for a given starting value q_0.

$F(q_0)$ and $F_l(q_0)$ are plotted by Fig. 4.12. By comparing both recursion formulas, they are coinciding with respect to

$$\frac{\sigma_a(T)}{\sigma(T)} = F(h_l) = F(q_l); \quad h_l(h_0(T)) = q_l(q_0(T)). \tag{4.64}$$

From Eqs. (4.40a, 4.40b, 4.40c) one can calculate q_0 after knowing h_0 and h_l or h_0 after knowing q_0 and $q_l = h_l$:

$$q_0 = h_0 \cdot \left(\frac{h_l}{h_0}\right)^3; \quad h_0 = q_0 \cdot \left(\frac{q_l}{q_0}\right)^{3/2}. \tag{4.65}$$

Most authors argue, that the difference between specular and diffuse reflection is not of surprisingly significant importance. Ref. [9] compares measured curves to calculations and by that comes to the conclusion, that the diffuse assumption results in better fits to measurements (all in the GHz-range).

In this paper we argue with the dependence of the averaged incidence angle γ of reflected electrons, which are contributing to anomalous current losses. Each loss is weighted with its current loss contribution. Instead of $\langle\gamma\rangle$, $\langle sin\gamma\rangle = \langle w\rangle$ can be calculated much easier, and reflection is performed at plane $h = 0$ with positive w

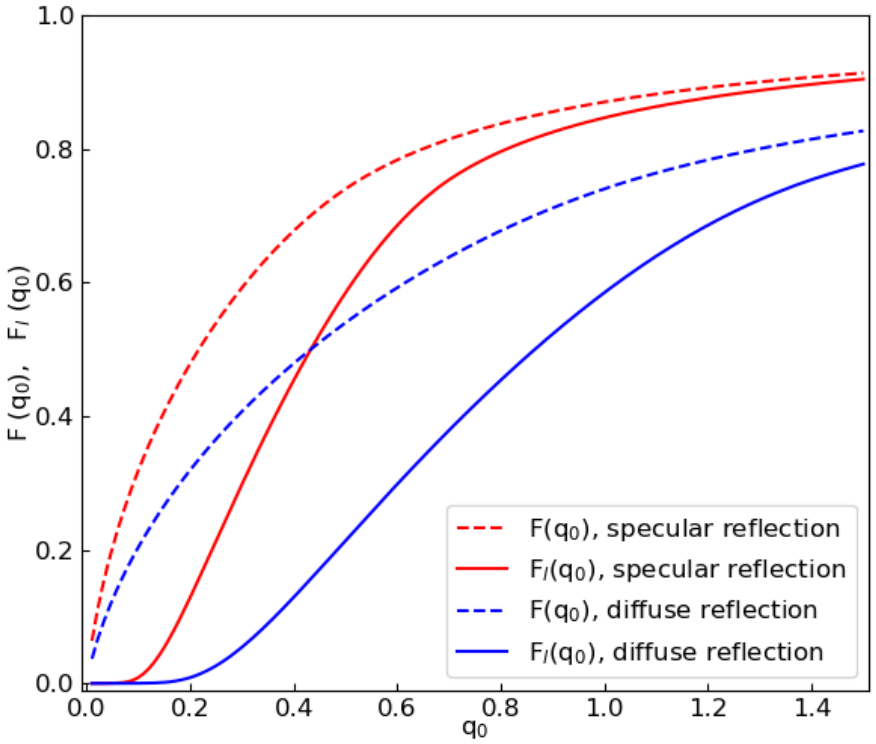

Figure 4.12: Plot of $F(q_0)$- and $F_l(q_0)$-functions for specular and diffuse reflection.

for convenience:

$$\langle sin\gamma \rangle = \left[\int_0^{h_0} \int_h^1 \int_{-(1-w^2)^{1/2}}^{(1-w^2)^{1/2}} w \cdot (1 - w^2 - u^2) dudwdh \right] / U \tag{4.66}$$

with

$$U = \int_0^{h_0} \int_h^1 \int_{-(1-w^2)^{1/2}}^{(1-w^2)^{1/2}} (1 - w^2 - u^2) dudwdh \tag{4.67}$$

giving

$$\begin{aligned} \langle sin\gamma \rangle &= (1.5 - h_0^2 + 0.3h_0^4)/(4 - 3h_0 + 0.5h_0^3), \quad h_0 \leq 1 \\ \langle sin\gamma \rangle &= 0.55, \quad h_0 > 1 \end{aligned} \tag{4.68}$$

At lower h_0-values (lower operation temperatures) smaller angles dominate (see Fig. 4.13). For values $h_0 > 1$ the mean scattering angle stays constant. Therefore,

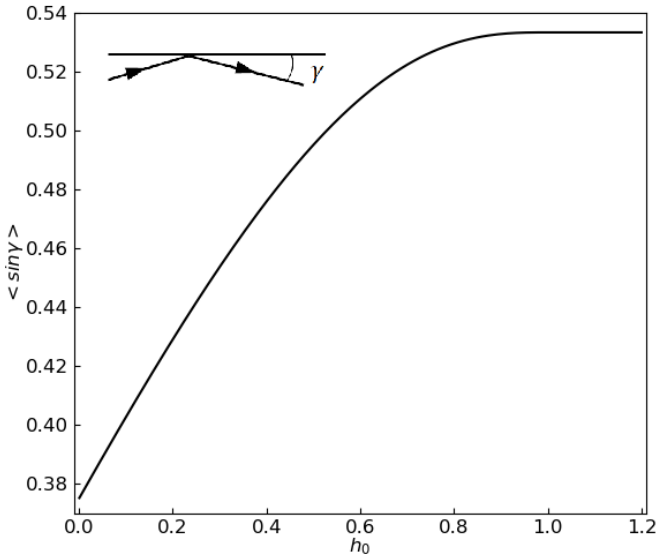

Figure 4.13: Plot of the $\langle sin\gamma \rangle$-function.

and by finding an optimum match with measurements the following combination of F–functions for specular and diffuse reflection is proposed:

$$F(h_0) = (a - \alpha b) \cdot F_{s1} + (1 - a + \alpha b) F_{d1} \quad \text{for} \quad h_0 < 0.5 \tag{4.69a}$$

$$\text{with} \quad 2a - b = 1, \quad \alpha = \frac{\overline{sin\gamma}(h_0) - \overline{sin\gamma}(h_0 = 0)}{\overline{sin\gamma}(h_0 = 1.0) - \overline{sin\gamma}(h_0 = 0)} \tag{4.69b}$$

$$F(h_0) = (a - \alpha b) \cdot F_{s2} + (1 - a + \alpha b) F_{d1} \quad \text{for} \quad 0.5 \leq h_0 < 1 \tag{4.69c}$$

$$F(h_0) = (a - b) \cdot F_{s2} + (1 - a + b) F_{d2} \quad \text{for} \quad h_0 > 1 \tag{4.69d}$$

$$\text{An adequate choice is} \quad a = 0.75, \quad b = 0.5 \tag{4.69e}$$

The F-functions from Eqs. (4.69a, 4.69c, 4.69d) are to be used finally in the recursion Eqs. (4.60, 4.62).

Fig. 4.14 allows a comparison of the three functions. An easy transformation from

DC- to RF-conductivity and vice-versa is possible by Table B.1. Additionally, each line contains parameters relevant in the geometric model.

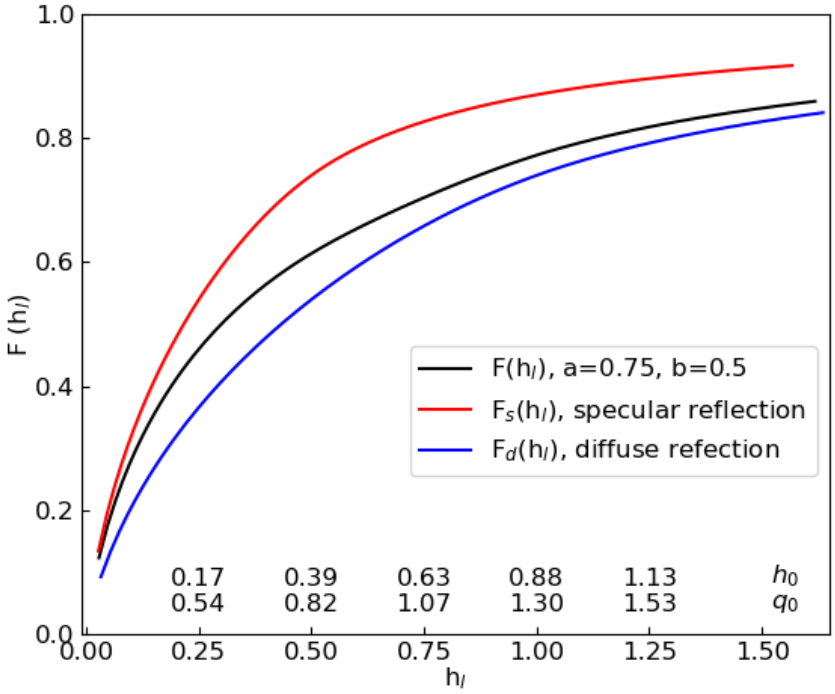

Figure 4.14: Plot of $F_s(h_l)$, $F_d(h_l)$, $F(h_l)$, for the mixing parameters a=0.75, b=0.5.

4.3.5 Specific Surface Resistance

The wall losses in the cavity at a surface element $dxdz$ with magnetic surface field amplitude H_0 are given by

$$dP = \frac{1}{2} H_0^2 \cdot R \cdot dxdz \tag{4.70}$$

with the specific surface resistance, by including anomalous losses:

$$\begin{aligned} R(T)/\Omega \quad &= \frac{\rho_a(T)}{\delta_a(T)} = \sqrt{\frac{\omega \cdot \mu_0}{2\sigma_a(T)}} = \sqrt{\frac{\omega \cdot \mu_0}{2\sigma(T) \cdot F_l(h_0)}} \\ &= R_c(T) \cdot F_l(h_0)^{-1/2}. \end{aligned} \tag{4.71}$$

$R_c(T)$ is the "classic" result regarding the normal skin effect only.

This means, the surface resistance by including the anomalous skin effect is a factor $F_l(h_0)^{-1/2}$ larger than predicted from the normal skin effect. Eq. (4.71) is applicable, as soon as the dc–conductivity values $\sigma(T)$ are known to calculate $h_0(\sigma)$ and to insert the tabulated $F_l(h_0)$–value.

For comparison, the same ratio can be calculated from the formulas as published by R.G. Chambers[9] with the so-called diffusion model. The interpolation formula in [9], Eq. (A.1) and inserting the constants in R_∞ gives for copper

$$R(T) = 1.123 \cdot 10^{-9} \cdot f^{2/3}[1 + F_R \cdot (\alpha)^{-G}]. \tag{4.72a}$$

Under the assumption of diffuse electron reflection at the surface the coefficients are

$$F_R = 1.157, \quad G = 0.2757. \tag{4.72b}$$

In case of specular reflection instead, the formula from R.G. Chambers results in the coefficients

$$F_R = 1.376, \quad G = 0.3592. \tag{4.72c}$$

When applying the same formula to the results of Reuter–Sondheimer[31], Chambers found for that case the adequate coefficients

$$F_R = 1.004, \quad G = 0.333. \tag{4.72d}$$

The "classic" case, neglecting the anomalous skin effect gives $R_c(T) = \sqrt{\pi f \mu_0 \rho(T)}$.

The parameter α in Eq. (4.72a) is related to h_0 as defined above by $\alpha = 1.5 \cdot (h_0)^{-2}$ - see Eq. (4.28, 4.40b) and (Ref. [31] - Eq. (19)). This gives then with Eq. (4.72a)

$$\frac{R(T)}{R_c(T)} = \frac{[1 + F_R \cdot (1.5/h_0^2)^{-G}]}{1.93 \cdot h_0^{1/3}}. \tag{4.73}$$

According to the author, the equations of the diffusion model are applicable for $\alpha > 3$, that is $h_0 < 0.7$, where the anomalous skin effect makes significant

contributions. As can be seen by Fig. 4.15, the geometric model predicts a larger contribution of the anomalous skin effect than all diffusion model variants as soon as $h_0 > 0.0005$. This gets visible mainly in the range, where the skin depth and the free path length are of the same order of magnitude.

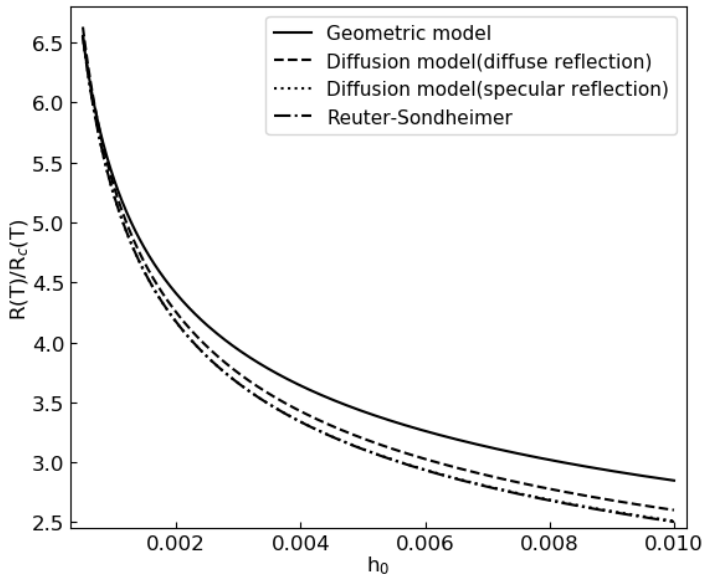

(a) $0.0005 \leq h_0 \leq 0.01$

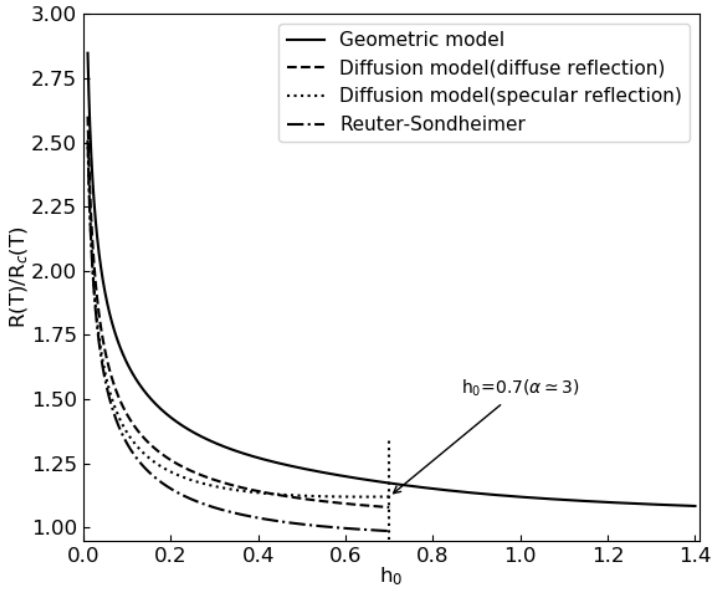

(b) $0.01 \leq h_0 \leq 1.4$

Figure 4.15: Plot of $R(T)/R_c(T)$ according to Eq. (4.71) and to Eqs. (4.72a, 4.72b, 4.72c, 4.72d, 4.73).

In the next few chapters three $\lambda/4$ coaxial cavities were designed and built. After all the preparations the quality factor of the cavities were measured in the temperature range from about 10 K to room temperature. Theoretical calculations based on the theory and the geometric model presented in this chapter were done in Chapter 7 to comparing with the measured results.

Chapter 5

Simulations and Design of Three $\lambda/4$ Coaxial Resonators

For the experiment three $\lambda/4$ coaxial resonators were designed and built. Copper tubes with diameters of 360 mm and 70 mm, each at a thickness of 5 mm, were available in the workshop store, as shown in Fig. 5.1. These tubes were cut to the

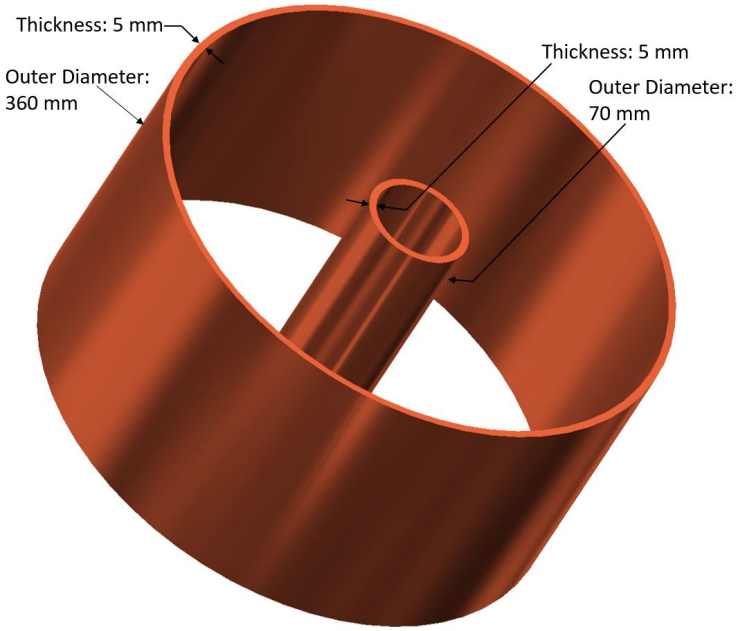

Figure 5.1: Dimension of the outer and inner conductor of the three coaxial resonators.

lengths as needed to get the quarter-wave resonators. End flanges from bulk copper were produced and the tubes were in a one-step procedure vacuum-brazed to the end-plates by a silver-solder.

The three coaxial cavities have the same structure but different lengths, which correspond to three different resonant frequencies. The planned resonant frequencies are 100 MHz, 220 MHz and 340 MHz. In free space, the wavelength λ is given by

$$\lambda = \frac{c}{f} \tag{5.1}$$

where c is the speed of light in free space. Theoretically the lengths of the three cavities ($\lambda/4$) are about 220 mm for the 340 MHz cavity, 341 mm for the 220 MHz cavity and 749 mm for the 100 MHz cavity. For $\lambda/4$ coaxial resonators, a gap is reserved at one end between the top cover and the inner conductor as seen in Fig. 5.2. At the other end the inner and outer conductors are short-circuited. Due to these changes of the coaxial structure, the lengths of the cavities will be slightly different from the theoretical values. The exact values of the lengths l of the outer cylinder and the size of the gap will be verified in simulations with CST Microwave Studio (MWS). CST MWS[34] is a commercial software and simulation code, which can solve 3-dimensional electrodynamic fields for arbitrary volumes and bodies.

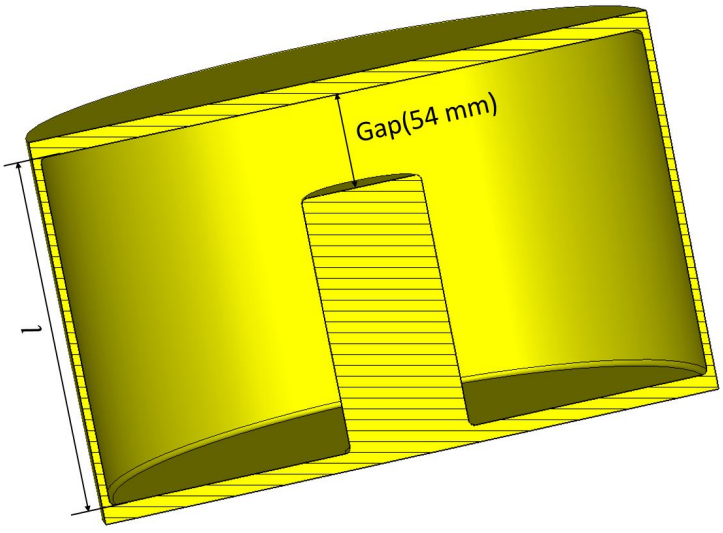

Figure 5.2: Sectional isometric view of the simplified and parameterized CST mode.

5.1 Determining the Resonant Frequencies

A coaxial cavity can be seen as an LC-circuit which is an oscillating system. According to Thompson's equation, the resonant frequency f of the LC-circuit is yields:

$$f = \frac{1}{2\pi\sqrt{LC}} \tag{5.2}$$

where L and C are the inductance and the capacitance, respectively. L and C are determined by the structure of the cavity which are explained in Chapter 5.4. Therefore, the resonant frequency of the cavity can be adjusted via the length of the outer cylinder and the gap size (see Fig. 5.2). Figures 5.3, 5.4 and 5.5 illustrates the results of simulations. The resonant frequency decreases as the length of the outer conductor increases and the size of the gap decreases. Based on the simulations, the size of the gap has been chosen to be 54 mm for the three cavities. The lengths of the outer conductor $l_{outer_cylinder}$ have been chosen to be 735 mm for the 100 MHz cavity (the longest cavity), 324 mm for the 220 MHz cavity (the middle cavity) and 201 mm for the 340 MHz cavity (the shortest cavity).

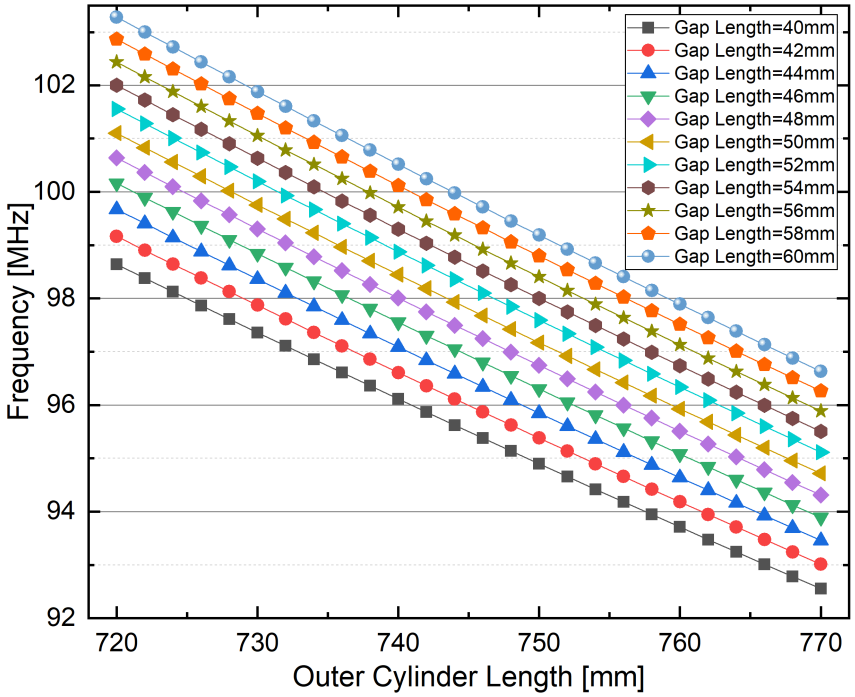

Figure 5.3: Dependence of the resonant frequencies of the 100 MHz on the length of the outer cylinder and the gap size.

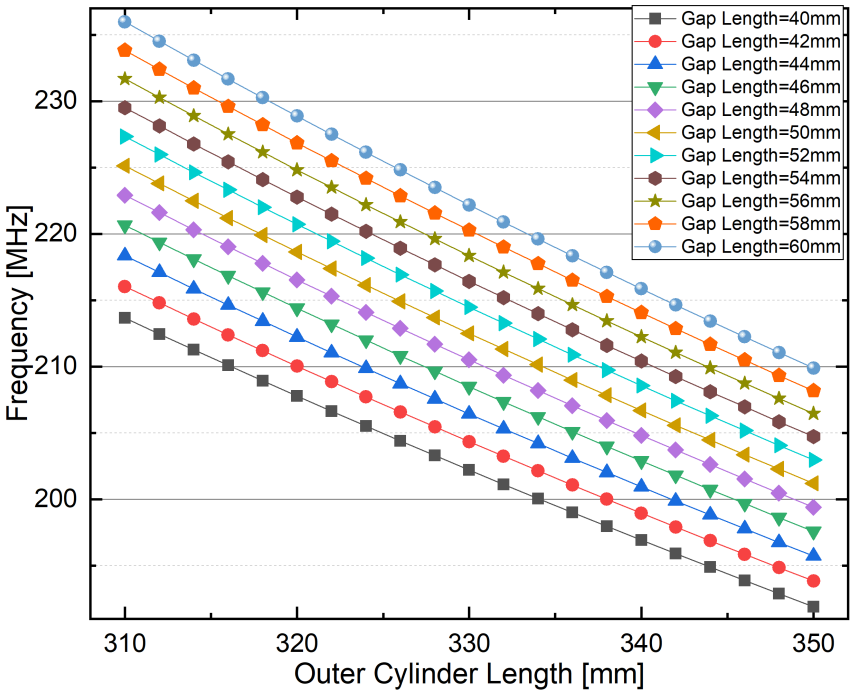

Figure 5.4: Dependence of the resonant frequencies of the 220 MHz on the length of the outer cylinder and the gap size.

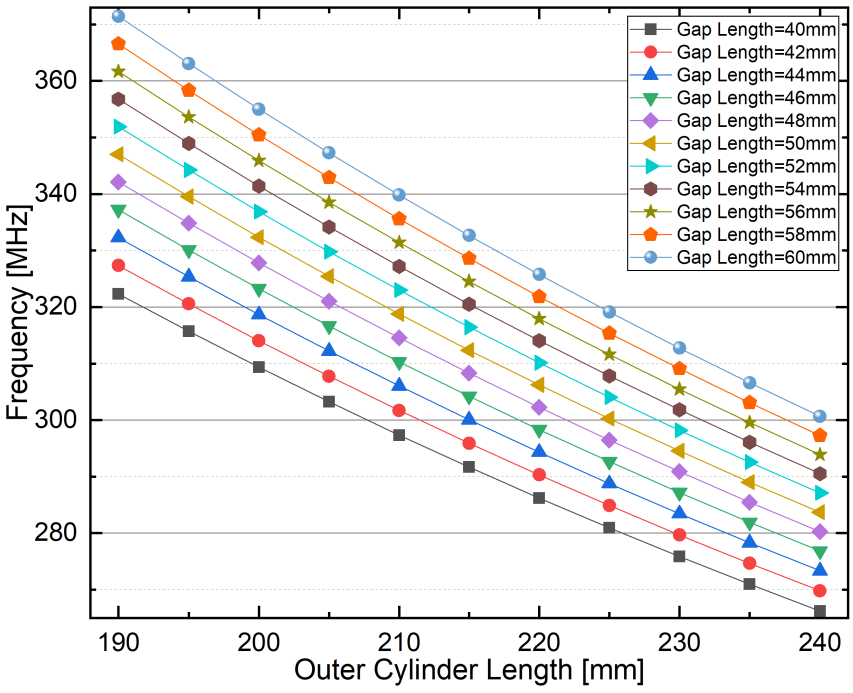

Figure 5.5: Dependence of the resonant frequencies of the 340 MHz on the length of the outer cylinder and the gap size.

5.2 Field Distribution

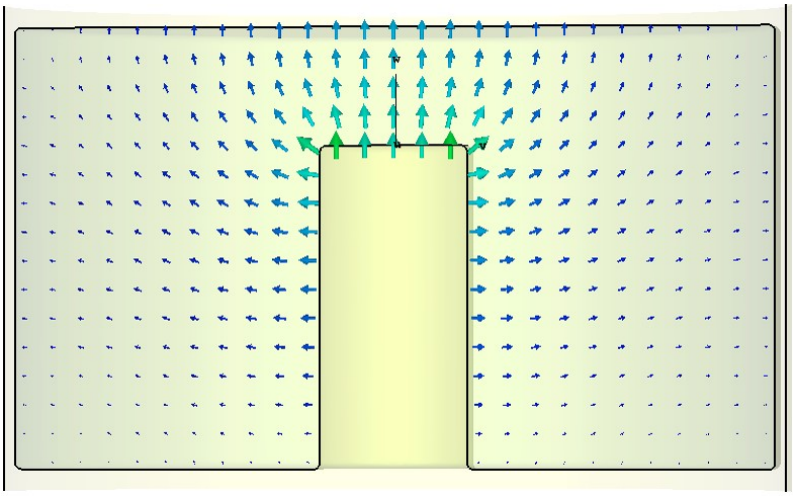

(a) Electric field

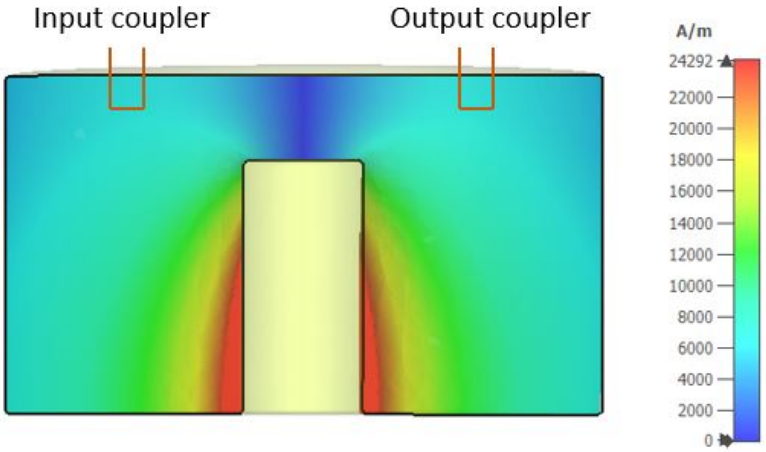

(b) Magnetic field $|B_\varphi|$

Figure 5.6: Distribution of the electric and magnetic fields from simulations. By the simulations the stored energy in the cavity is $1J$.

Fig. 5.6 illustrates the electric and magnetic field distributions in the $\lambda/4$ coaxial cavity. The electric field is perpendicularly oriented between the inner and outer conductors and increases by the sine function from the bottom to the top of the cavity. The magnetic field wraps around the inner conductor and decreases from the bottom to the top of the cavity by the cosine function. For the experiments, the inductive coupling was chosen for the cavities. The coupling strength should be very weak for the measurements (see Chapter 6.1). Therefore, two small loops were used

as the input and output coupler (weak coupling) which are located at the top cover, where the B-field is relatively weak (see Fig. 5.6(b)).

5.3 Mechanical Design of the Cavities

Based on the simulations a mechanical design of the three coaxial cavities was made. The structure can be divided into two main parts: the top cover and the tank.

The top cover was manufactured from stainless steel, as shown in Fig. 5.7. There are totally five flanges welded on it for the coupling and vacuum. To minimize the RF losses in the walls, the inner side of the top cover was galvanically high-gloss copper-plated with a thickness of 100 μm in the company Galvano-T.

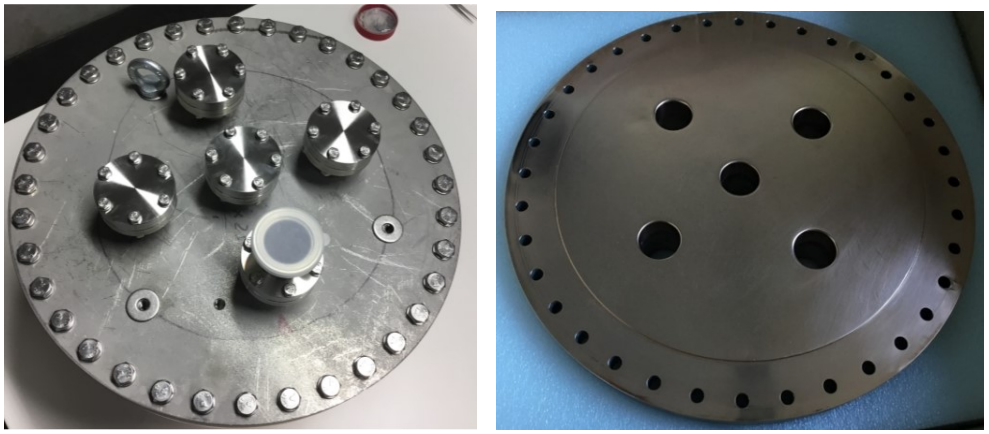

(a) (b)

Figure 5.7: Structure of the top cover. (a). Five flanges were welded on it. (b). Inner side of the cover was galvanically high-gloss copper-plated with the thickness of 100 μm.

The tank was produced from bulk copper and the different parts of it were in a one-step procedure vacuum-brazed together with the silver-solder in GSI (Helmholtz Centre for Heavy Ion Research), as shown in Fig. 5.8. The dimension of the shortest cavity is shown in Fig. 5.9. As described at the beginning of this chapter, the three coaxial cavities have the same structure, but different lengths. A complete description of the dimensions of the three cavities can be found in Appendix A.

Two cavity components are screwed together. A teflon ring and an aluminum ring (see Fig. 5.8) were used for the vacuum sealing and RF contact, respectively. The

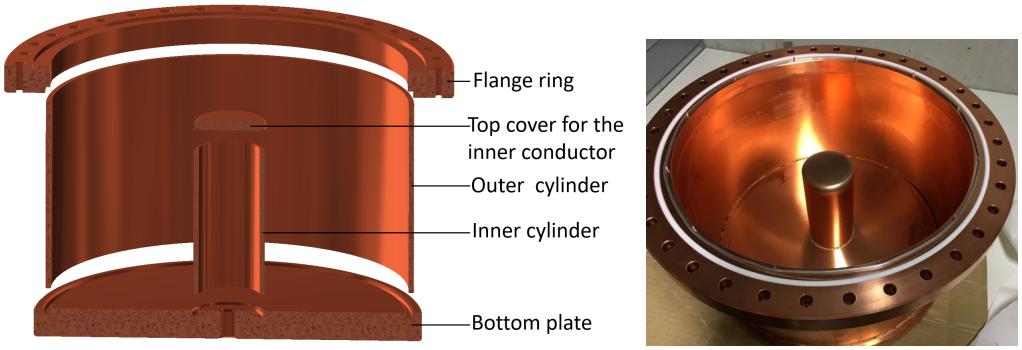

(a) (b)

Figure 5.8: Structure of the main part of the cavity. (a). Cross section view of the cavity with separate parts. (b). Cavity after being vacuum brazed with silver in GSI.

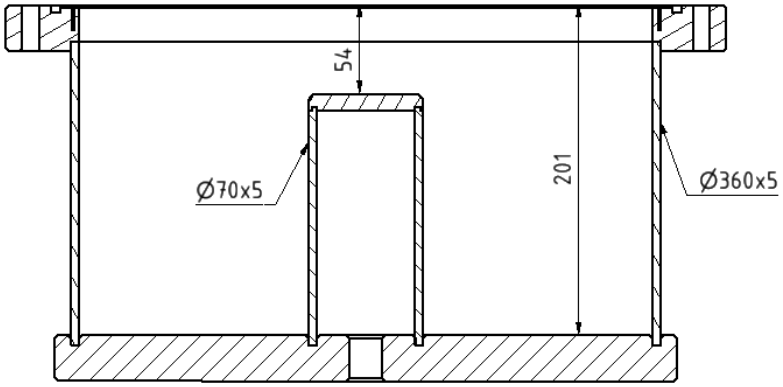

Figure 5.9: Cross section view of the 340 MHz cavity with dimensions.

aluminum ring was soft annealed at 400 $°C$ for 5 hours in a vacuum oven by GSI to make sure it is soft enough not to damage the contact surface of the copper flange.

5.4 Calculation of the Basic Parameters

In a cylindrical coordinate system (r, φ, z) (see Fig. 5.10), the z-axis passes through the center of the coaxial cavity. The transverse electric and magnetic fields (TEM)

are given by

$$E_r(r,z,\alpha) = \frac{E_0}{r} \cdot e^{i(\vec{k}\cdot\vec{z}-\alpha)} \tag{5.3}$$

$$H_\varphi(r,z,\alpha) = \frac{E_0}{r \cdot Z_F} \cdot e^{i(\vec{k}\cdot\vec{z}-\alpha)} \tag{5.4}$$

where E_0 is the amplitude of the E-field, r the radial distance from the z-axis, $Z_F = \sqrt{\mu_0/\epsilon_0} = 377\Omega$ the impedance of free space and α a constant phase.

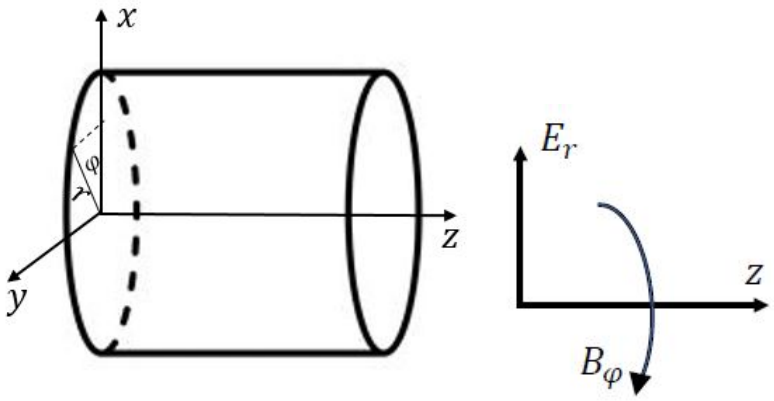

(a) (b)

Figure 5.10: (a). A cylindrical coordinate system r, φ, z. (b). E-field is along the radial coordinate r. B-field always remains perpendicular to the E-field, as this is a TEM - mode.

If the inner and outer cylinders of a coaxial conductor are short-circuited at $z = 0$ with a metal plate, as shown in Fig. 5.11, the electromagnetic wave will be totally reflected on this metal plate and a standing wave is formed in the coaxial conductor:

$$E_r(r,z,\alpha) = \frac{E_0}{r} \cdot e^{-i\alpha}(e^{i\vec{k}\cdot\vec{z}} - e^{-i\vec{k}\cdot\vec{z}}) = 2i \cdot \frac{E_0}{r} sin(\vec{k}\cdot\vec{z}) \cdot e^{-i\alpha} \tag{5.5}$$

$$H_\varphi(r,z,\alpha) = \frac{E_0}{r \cdot Z_F} \cdot e^{-i\alpha}(e^{i\vec{k}\cdot\vec{z}} + e^{-i\vec{k}\cdot\vec{z}}) = 2 \cdot \frac{E_0}{r \cdot Z_F} \cdot cos(\vec{k}\cdot\vec{z}) \cdot e^{-i\alpha} \tag{5.6}$$

From these two equations one can see that the electrical oscillation is spatially shifted by $\lambda/4$ and temporally by 90^o compared to the magnetic oscillation, as shown in Fig. 3.4. If the radius of the inner cylinder is r_i and the radius of the outer cylinder is r_o, the voltage between the inner and outer cylinders can be obtained by integrating the

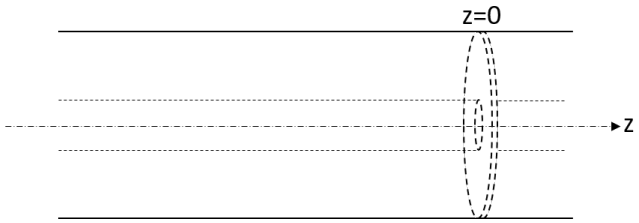

Figure 5.11: A coaxial conductor is short-circuited at one end by $z = 0$.

E_r from r_i to r_o:

$$V(z,\varphi) = \int_{r_i}^{r_o} E_r dr = 2iE_0 sin(\vec{k}\cdot\vec{z}) \cdot ln\frac{r_o}{r_i} \cdot e^{-i\alpha} = V \cdot sin(\vec{k}\cdot\vec{z}) \cdot e^{-i(\alpha-\frac{\pi}{2})} \quad (5.7)$$

where V is the amplitude of the voltage.

The capacitance between the top cover and the inner conductor is

$$C_{gap} = \frac{\varepsilon_0 A}{d} \quad (5.8)$$

where A is the area of the top cover of the inner conductor and d is the size of the gap between the top cover and the inner conductor.

Due to the capacitively loaded termination at the open end with the capacitance C_{gap}, the length of the inner conductor should be changed from $\lambda/4$ to l[36]:

$$l = \frac{\lambda}{2\pi} arctan\frac{1}{\omega C_{gap} Z_L} \quad (5.9)$$

where Z_L is the line impedance in vacuum. The capacitance per meter between the inner and outer cylinders is[21]

$$C_c' = \frac{2\pi\varepsilon_0}{ln(r_o/r_i)} \quad (5.10)$$

The effective capacitance between the inner and outer conductor is

$$C_c = -\int_0^l C_c' \cdot sin(\frac{2\pi}{\lambda} \cdot z) dz \quad (5.11)$$

The total capacitance of the cavity is

$$C_t = C_c + C_{gap} \tag{5.12}$$

The inductance per meter between the inner and outer cylinders is[21]

$$L^{'} = \frac{\mu_0}{2\pi} ln\left(\frac{r_o}{r_i}\right) \tag{5.13}$$

The effective inductance of the coaxial cavity is

$$L = \int_0^l L^{'} \cdot cos(\frac{2\pi}{\lambda} \cdot z)dz \tag{5.14}$$

According to Eqs. (5.11, 5.8, 5.12 and 5.14), the capacitance and the inductance of the three coaxial cavities are listed in Table 5.1

Table 5.1: Capacitance and Inductance of the three coaxial cavities.

Cavity	$C_c(pF)$	$C_{gap}(pF)$	$C_t(pF)$	$L(\mu H)$
Longest cavity	16.12	0.724	16.844	0.154
Middle cavity	7.12	0.724	7.844	0.070
Shortest cavity	4.48	0.724	5.204	0.045

The resonant frequencies of the three cavities can be calculated according to Eq. (5.2): $f = 1/2\pi\sqrt{C_t L}$. The comparison of the theoretically calculated and the simulated resonant frequencies at room temperature is listed in Table 5.2 The

Table 5.2: Comparing the theoretically calculated resonant frequencies with the simulate resonant frequencies.

Cavity	calculated f (MHz)	simulated f (MHz)	difference
Longest cavity	101.17	100	1.17%
Middle cavity	225.85	220	2.66%
Shortest cavity	354.44	340	4.25%

difference between the theoretical calculated and the simulated resonant frequencies is mainly due to the capacitively loaded termination at the open end, which leads to an increase of the capacitance and the inductance. Therefore, the calculated resonant frequencies are relatively smaller than the simulated resonant frequencies.

The stored energy is given by

$$W = \frac{1}{2}(C_{gap}V^2 + \int_0^l C_c' \cdot V^2 sin^2(\frac{2\pi}{\lambda}z)dz) \tag{5.15}$$

Neglecting the effect of capacitive shortening, which means, $l = \lambda/4$, the stored energy W is now equal to

$$W = \frac{1}{2}(C_{gap} + \frac{C_c'\lambda}{8})V^2 \tag{5.16}$$

We assume that the amplitude of the voltage V is 100 kV, the stored energy W can be calculated according to Eq. (5.16) and the results are listed in Table 5.3.

Table 5.3: Stored Energy in the three cavities.

Cavity	W(J)
Longest cavity	0.06710
Middle cavity	0.03160
Shortest cavity	0.02098

According to Eq. (3.4), the power loss by different parts of a cavity (see Fig. 5.12) can be calculated as:

1. Power loss by the inner and outer conductor:

$$\int_0^l \frac{1}{2}(\frac{2E_0}{r_{i/o} \cdot Z_F}\cos kz)^2 \cdot \sqrt{\frac{\rho\omega\mu_0\mu_r}{2}} \cdot 2\pi r_{(i/o)} \cdot dz \tag{5.17}$$

2. Power loss by the bottom cover:

$$\int_0^l \frac{1}{2}(\frac{2E_0}{r \cdot Z_F})^2 \cdot \sqrt{\frac{\rho\omega\mu_0\mu_r}{2}} \cdot 2\pi r \cdot dr \tag{5.18}$$

If the amplitude of voltage V is 100 kV, the amplitude of the electric field $E_0 = V/2ln(r_o/r_i) = 31.07kV/m$ according to Eq. (5.7). Substituting the value of E_0 into Eqs. (5.17, 5.18) and neglecting the effect of capacitive shortening, we get the power losses of the three main parts of the cavities: the outer conductor, the inner conductor, the shorting plate and list them in Tables 5.4, 5.5 and 5.6.

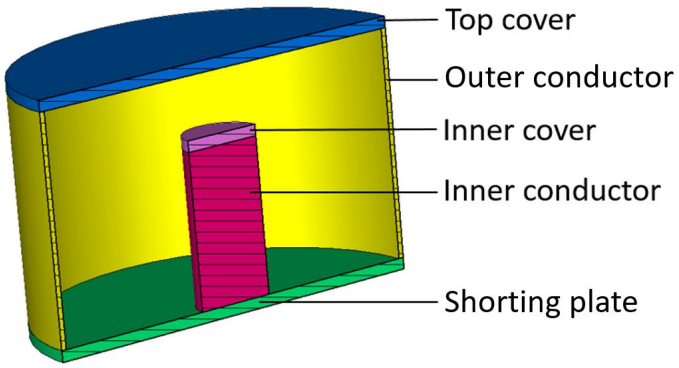

Figure 5.12: Different parts of the coaxial cavity.

Table 5.4: Power losses of different part of the 100 MHz cavity.

Parts	P_c/kW	percentage
Inner conductor	2.162	72.38%
Outer conductor	0.467	15.63%
Shorting plate	0.358	11.99%

Table 5.5: Power losses of different part of the 220 MHz cavity.

Parts	P_c/kW	percentage
Inner conductor	1.271	60.32%
Outer conductor	0.305	14.48%
Shorting plate	0.531	25.20%

Table 5.6: Power losses of different part of the 340 MHz cavity.

Parts	P_c/kW	percentage
Inner conductor	1.177	58.59%
Outer conductor	0.172	8.56%
Shorting plate	0.660	32.85%

The percentage of the power loss for different parts from simulations is listed in Table 5.7. Comparing the percentages of the power losses of the three main parts: the tank shell, the inner conductor and the shorting plate, to the theoretically calculated percentages listed in Table 5.4, 5.5 and 5.6, the results of the 100 MHz cavity agree with the simulated results very well and the results of the 220 MHz cavity agree with the simulated results also quite close. The results of the 340 MHz cavity fit the simulated results not as well, which means, the capacitive shortening at one end affects the shortest cavity most.

Table 5.7: Percentage of the power loss for different parts of a cavity from simulations (see Fig. 5.8 for designations).

Cavity	100 MHz	220 MHz	340 MHz
Top cover	0.15%	1.47%	5.3%
Outer conductor	15.26%	14.35%	15.85%
Inner cover	0.03%	0.25%	0.80%
Inner conductor	73.14%	62.18%	48.31%
Shorting plate	11.42%	21.74%	29.71%

Substituting the calculated results of the stored energy W and the power loss P into Eq. (3.5), we obtain the quality factors Q_0 of the three cavities. The comparison of the simulated and calculated Q_0 is listed in Table 5.8. The calculated Q_0 is larger than the simulated Q_0. This is plausible as the losses in the top cover and at the end-lid of the inner conductor were neglected.

Table 5.8: Comparison of the simulated and the calculated quality factors Q_0.

Cavity	Simulated Q_0	calculated Q_0	Difference
$Q_{0,100MHz}$	13060	14107	7.4%
$Q_{0,220MHz}$	17264	20721	16.7%
$Q_{0,340MHz}$	19665	22298	11.8%

Chapter 6

Measurement Method and cavity Preparation

6.1 Measurement Method

Normally, the output coupler only serves as a detector of the phase and for an amplitude measurement of the stored field energy, so its loop is kept very small, namely, $\beta_t \ll 1$. If the input coupler is also very small, which means, $\beta_e \ll 1$, according to Eq. (3.21) in Chapter 3.3, we can get that:

$$Q_0 \approx Q_L \tag{6.1}$$

Q_L can be measured directly with a network analyzer in the experiment. If a resonator is very weakly coupled with very small couplers, the measured Q_L can be seen as the approximation of Q_0 .

The couplers for the experiment are shown in Fig. 6.1. One can directly measure the coupling strength β_e according to Eq. (3.52) with the two loops used for the experiment.

One can also mesure β_e with Eq. (3.54) by introducing a third loop, which is relative larger than the two loops for the experiment. The third loop was used for the input coupler and the input coupler for the experiment replaced the pickup used as the output coupler. In this case, the calculated β_t with Eq. (3.54) is exactly the value of β_e of the input coupler for the experiments and is listed in Table 6.1. We

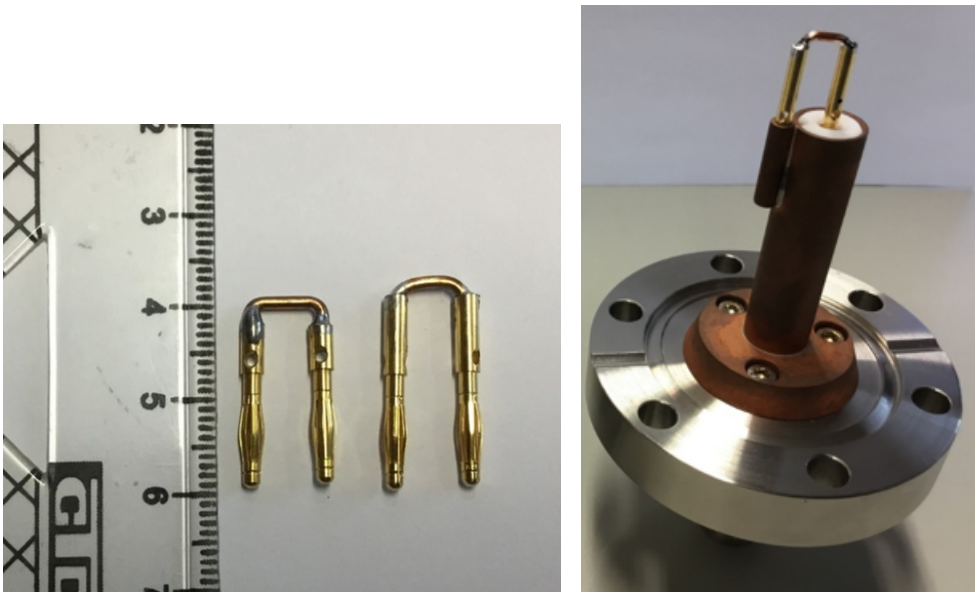

(a) (b)

Figure 6.1: Couplers used for the measurements. (a). The size of the input and output couplers. On the left is the output coupler and on the right is the input coupler. (b). Flange used for the couplers.

use the second method with Eq. (3.54) to measure the coupling strength, because it is more accurately than the first method with Eq. (3.52).

Table 6.1: β_e at room temperature for the three cavities.

Cavity	β_e
100MHz	3.21×10^{-4}
220MHz	6.15×10^{-4}
340MHz	4.24×10^{-4}

As we can see, all the values of β_e have an order of -4, which are small enough for the experiment. According the definition of β_e in Eq. (3.19)

$$\beta_e \propto \frac{1}{P_c} \propto \frac{1}{R_s} \propto \frac{1}{\sqrt{\rho}}. \tag{6.2}$$

So the β_e at lower temperatures can be given by

$$\beta_{e,low} = \beta_{e,room} \cdot \sqrt{\frac{\rho_{room}}{\rho_{low}}} \tag{6.3}$$

We assume that the RRR value of the copper is 200, which is larger than the bulk copper used for the original cavities in experiments. According to Eq. (6.3), β_e at the cryogenic temperature near 4 K is listed in Table 6.2. They have the order of -3, which are still small enough for the experiments. Therefore, these two loops are suitable for the measurements from cryogenic temperature near the absolute zero to the room temperature.

Table 6.2: β_e at the cryogenic temperature near 4 K for the three cavities.

Cavity	$\beta_{e,cryo}$
100MHz	4.54×10^{-3}
220MHz	8.70×10^{-3}
340MHz	6.01×10^{-3}

6.2 Multipacting and Conditioning

6.2.1 Multipacting

Electrons can be knocked out from the cavity walls by bombardment of charged particles, such as the impact of electrons. If the impact process occurs between two plane-parallel metallic plates (see Fig. 6.2) and the two conditions are fulfilled:

1. the electrons travel from surface to surface in an integer number of half periods of the ac voltage,

2. the secondary electron coefficient is larger than one,

electrons will be knocked out from the two metallic plates continuously until the avalanche is limited by the space charge of the electrons. This phenomenon is called multipacting. The electrons from the multipacting absorb energy from their interaction with the electromagnetic fields and limit the magnitude of the field.

The multipacting between two plane-parallel conducting plates belongs to the type of the two-point multipacting. Because electrons can be born at different phases of the RF wave, the two-point multipacting can occur at the range of voltages between

$$V_{max} = \frac{m\omega^2 x_0^2}{2e} \tag{6.4}$$

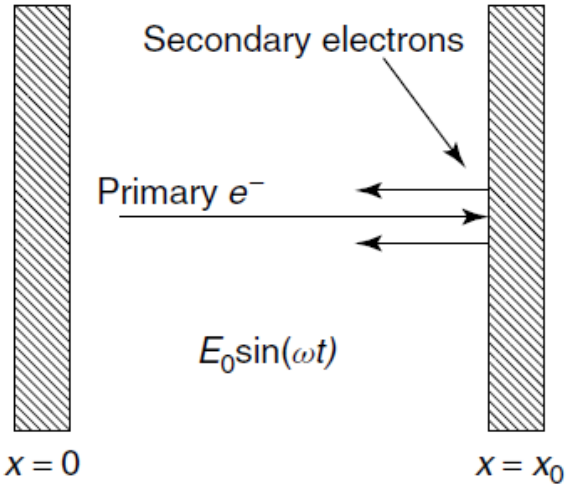

Figure 6.2: Initial stage of two-point multipacting between two plane surfaces[[38, p. 159]].

and

$$V_{min} = \frac{m\omega^2 x_0^2}{e} \frac{1}{\sqrt{4 + (2n+1)^2\pi^2}}, n = 0, 1, 2, ... \tag{6.5}$$

where e and m are the electron charge and mass. x_0 is the distance between the two conducting plates. The index n is the order of the multipacting level which is related to the transit time between two plates $t = (n + 1/2)T$, where T is the RF period. As n can be increased indefinitely, there is no lower limitation of the field for the occurrence of the two-point multipacting. While there is a maximum electric field

$$E_{max} = \frac{V_{max}}{x_0} = \frac{m\omega^2 x_0}{2e}, \tag{6.6}$$

above which the multipacting cannot occur, because for larger fields the electron transit times are too short and the first condition for the occurrence of the multipacting can not be satisfied.

Another form of multipacting is the single-point multipacting, which was discovered in superconducting cavities. For more information about the single-point multipacting the reader is referred to Ref. [38, chapter 5.9].

From Eqs. (6.4 and 6.5) we can see that the multipacting can occur from very

low electric field levels up to the value of Eq. (6.6). Normally these values are much lower than those typically used for the acceleration of the beam, which means, multipacting occurs when the cavity field is raised to the operating level. It can be reduced in size through the conditioning procedure.

With respect to multipacting, the coaxial resonator is indeed very sensitive. It has rather wide amplitude ranges as the voltage increases along the coaxial geometry from the shorting plate up to the gap. However, most pronounced multipacting levels occur with respect to the voltage levels around the gap area - that means, at low levels compared to the accelerating mode.

6.2.2 Conditioning

Discharges and multipacting occur due to the impurities on the surfaces, dust particles and absorbed gas molecules on the vacuum walls and limit the magnitude of the electric field. These impurities and dust particles on the surface of the resonator components can be burnt off during conditioning thereby decreasing the occurrence of multipacting and sparking.

The experimental setup for the conditioning is shown in Fig. 6.3. A network

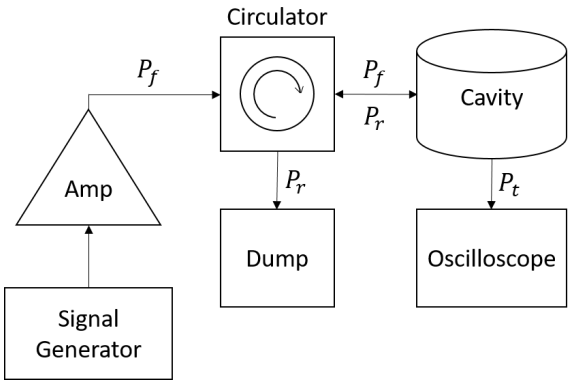

Figure 6.3: Schematic setup of the RF components for the conditioning procedure.

analyzer creates a low level sine voltage at the resonant frequencies of the cavity under test and drives the amplifier. The amplified RF signal is then applied to a circulator, a three port device which transmits the incoming RF signal to the output port in rotation. Finally the forward power is fed into the cavity. At the same time, the reflected power from the cavity is redirected to the third port of the circulator,

which is connected with a dummy resistor. The reflected power will be dissipated by the resistor to protect the amplifier.

Due to the limitation of the amplifier, the forward power can only reach 50 W. The sweep mode of the network analyzer is cw mode. The transmitted power P_t is fed into an oscilloscope. With the help of the voltage signal on the oscilloscope, one can adjust the frequency to meet the resonant frequency and observe the multipacting levels. At the same time, changes of the vacuum pressure in the cavity observed from a vacuum gauge is also a signal for the occurrence of multipacting.

For all the three cavities, the forward power was raised slowly from 0 W to 50 W. When the forward power reaches the maximum, it remained at this level for about three hours, which can burn off impurities and dust particles on the surface.

In particular, the conditioning process for the 100 MHz cavity was observed. According to Eqs. (6.4, 6.5), multipacting of first few orders occurs when the gap voltage is about 3270 mV (V_{max}), 1757 mV (n=0) and 679 mV (n=1), respectively, if the distance between two plane-parallel conducting plates is 54 mm, which corresponds to the size of the gap between the inner cylinder and the top cover. The gain of the amplifier for this conditioning system is 41.4 dB. The observed multipacting occurred when the input power of the network analyzer are -5.01 dBm, -10.5 dBm and -20 dBm, which correspond to the voltage of 3704 mV, 1968 mV and 659 mV respectively, which are close to the values given by Eqs. (6.4, 6.5). The multipacting was also observed by -0.02 dBm and -14.92 dBm, which should occur between the inner and outer conductors.

After that process the cavities were ready for quality factor measurements at room temperature and under cryogenic conditions as reported in the next chapter.

Chapter 7

Measurements

7.1 Measurements at Room Temperature

A first measurement of Q_0 at room temperature gave the results as shown in Table 7.1. At the same time, the theoretical numbers from CST–simulations are given for comparison (ρ was assumed to be $1.7 \cdot 10^{-8} \Omega m$).

Table 7.1: Characteristic cavity parameters at room temperature.

f_{cavity}	$Q_{0,sim}$	$Q_{0,meas}$	$Q_{0,meas}/Q_{0,sim}$
100 MHz	13060	11803	0.904
220 MHz	17264	15812	0.916
340 MHz	19665	17569	0.893

The reasons for the difference between the simulated and measured Q_0 can be

- The cavity was brazed together from different parts, not as a whole as used in the simulations (see Fig. 5.2),
- The contact between the top cover and the tank is not perfect,
- The surface roughness.

7.2 Cryogenic Experimental Setup

Cryogenic tests are done in a vertical He-cryostat. The prepared 340 MHz cavity with cryostat-lid at the top is shown in Fig. 7.1. The cavity was pumped by a

Figure 7.1: Photo of the prepared 340 MHz cavity, ready for installation in the cryostat: 1=turbo molecular pump station, 2=ion getter pump, 3=lid of the vertical cryostat, 4=cavity, 5=open cryostat, 6=heater, 7=coaxial cable for the input signal, 8=coaxial cable for the output signal, 9=temperature sensors.

combination of a turbo pumping-station and an ion getter-pump, as in use for the test of superconducting cavities. The signal is carried by two coaxial copper cables (7 and 8 in Fig. 7.1). After all preparations, the whole experimental setup was placed

in the cryostat (below ground floor level, Number 5) and cooled down to about 10 K with liquid helium. Two temperature sensors (Number 9) were used for the 340 MHz cavity to record the temperature changes. Both were taped to the sides of the cavity and close to the top and the end flanges respectively. The Q factor measurements were performed during the warming up phase of the cavity. With the help of a heater (Number 6), the measurement process can be shortened from more than 2 weeks in case of normal warming up to around 1 week by a forced warming up procedure.

For the other two longer cavities (220 MHz and 100 MHz), five temperature sensors were used and their location is shown in Fig. 7.2. Finally, the temperature value is taken as the average of all measured values.

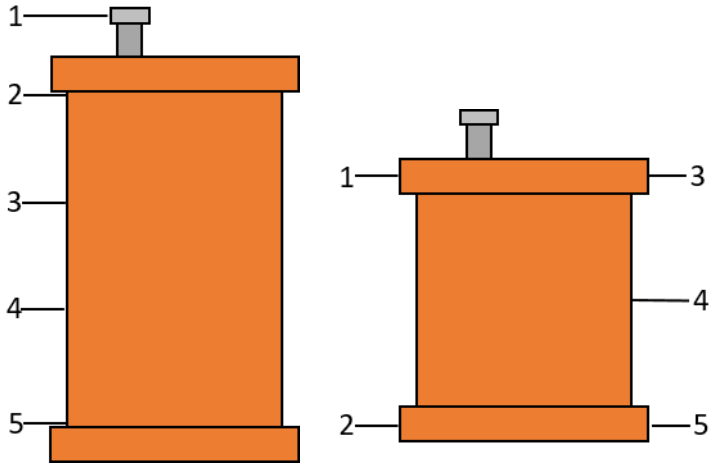

(a) 100 MHz (b) 220 MHz

Figure 7.2: Location of the temperature sensors for the 100 MHz and 220 MHz cavity.

7.3 Measurements from Cryogenic to Room Temperatures

The quality factors at different temperatures were directly measured and they are different at room temperature for the three cavities, as listed in Table 7.1. In order to better compare the measurement results, we plot the ratio of the measured Q factor to that at room temperature instead of directly plotting the measured Q-values versus the temperature, as shown in Fig. 7.3.

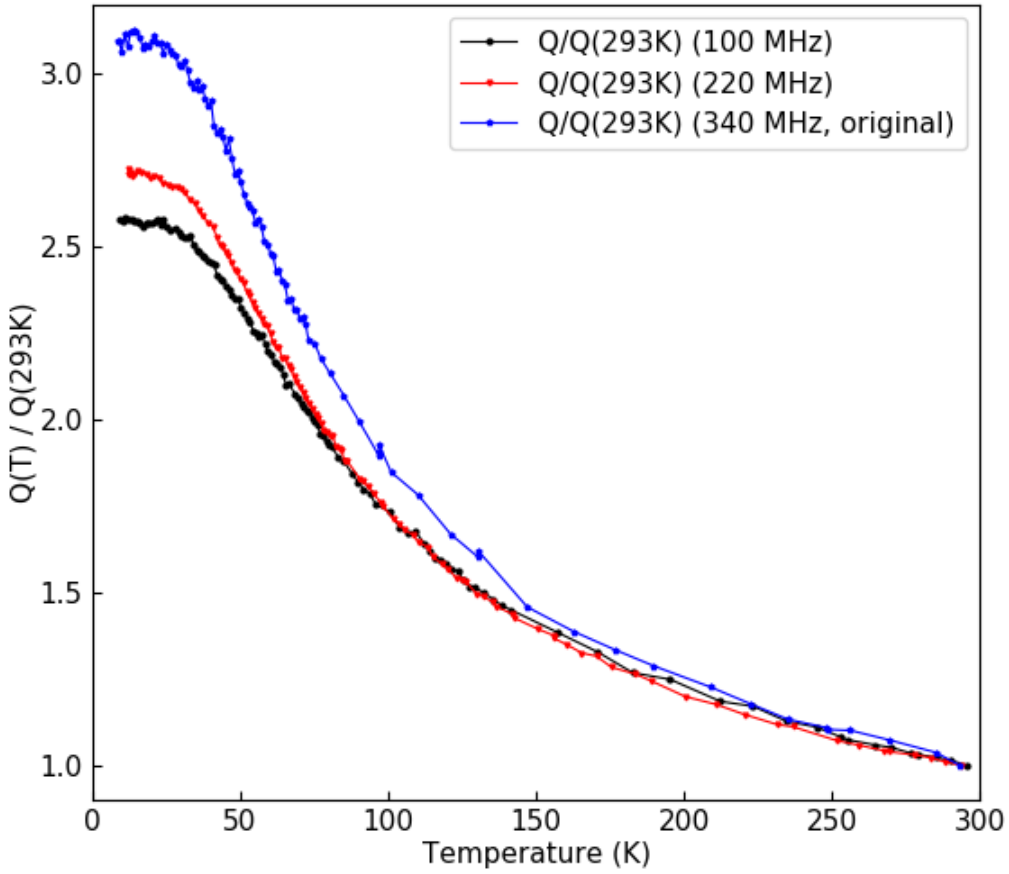

Figure 7.3: Measured Q(T)/Q(293K) - values over T for the three original cavities.

According to the geometric model presented in Chapter 4.3, one can find the DC-values $\sigma(T)$ from the RF measurements providing $\sigma_a(T)$. According to Eqs. (3.3, 3.4 and 3.5), we get

$$\frac{\sigma_n}{\sigma_a(T)} = \left(\frac{Q(293K)}{Q(T)}\right)^2. \tag{7.1}$$

Substituting the measured $Q(10K)/Q(293K)$ into Eq. (7.1) and according to Eq. (4.40c), the value of q_0 at 10 K can be calculated. According to the recursive method described in Chapter 4.3, one can obtain q_l from q_0. Substituting q_l into the Eq. (4.57c), we get $F_l(q_0) = F(q_l)$. According to Eq. (4.63), one obtains

$$\frac{\sigma(10K)}{\sigma_n} \cong \frac{\sigma_a(10K)}{\sigma_n} \cdot \frac{1}{F_l(q_0)}. \tag{7.2}$$

The calculated $\sigma(10K)/\sigma_n$ can be seen as an approximation of the RRR - values of the original bulk copper cavity. All the calculated results are listed in Table 7.2.

Table 7.2: RRR-values of the three original cavities calculated from the geometric model.

cavity	$Q(10K)/Q(293K)$	q_0	q_l	$F_l(q_0)$	$\sigma(10K)/\sigma_n$
100 MHz	2.57596	5.3938	4.7425	0.8792	10.8941
220 MHz	2.7087	4.6390	4.0110	0.8646	11.0786
340 MHz	3.09494	3.1099	2.5422	0.8174	11.7178

From these results it became evident, that the original RRR – values of the used copper-components were very low - RRR $\cong$ 11. This is not unusual for bulk - copper with unspecified cryogenic capabilities. As the behavior at lower frequencies was even worse, it is speculated, that some small fraction showing spontaneous magnetization like cobalt, nickel or iron should be contained in this bulk copper.

According to Eq. (4.40b), if $h_0 = 1$, $\sigma(T)/\sigma_n = \rho_n/\rho(T)$ is equal to about 31 at the frequency 100 MHz, about 24 at the frequency 220 MHz and about 20 at the frequency 340 MHz, which means, for these three frequencies: 100, 220 and 340 MHz, only RRR values are larger than 31, 24 and 20, respectively, the anomalous skin effect start to show a gradually stronger influence. The calculated RRR-values of the three original cavities is just about 11 (see Table 7.2), therefore, the anomalous skin effect exhibits only a small effect on the resistivity of the copper cavities at cryogenic temperatures and further affect the Q factor of the cavities slightly.

7.4 Measurements of the 340 MHz Cavity after the Copper Plating and Vacuum Annealing

In a next step the 340 MHz bulk copper cavity (without the stainless-steel end-lid) was matt copper–plated. This method was chosen, as it applies less organic ingredients in the copper–bath and forms larger copper grains. The completed cavity was again RF–preconditioned and tested in the cryostat. The measurement for that case was not as stable as the measurements before and after that case: A weak cable connection within the cryostat was found as the reason afterwards. Finally, inspired by Ref. [14], vacuum – annealing at 400°C for one hour of the copper-plated copper

cavity was performed in the vacuum furnace. The resulting values are plotted in Fig. 7.4

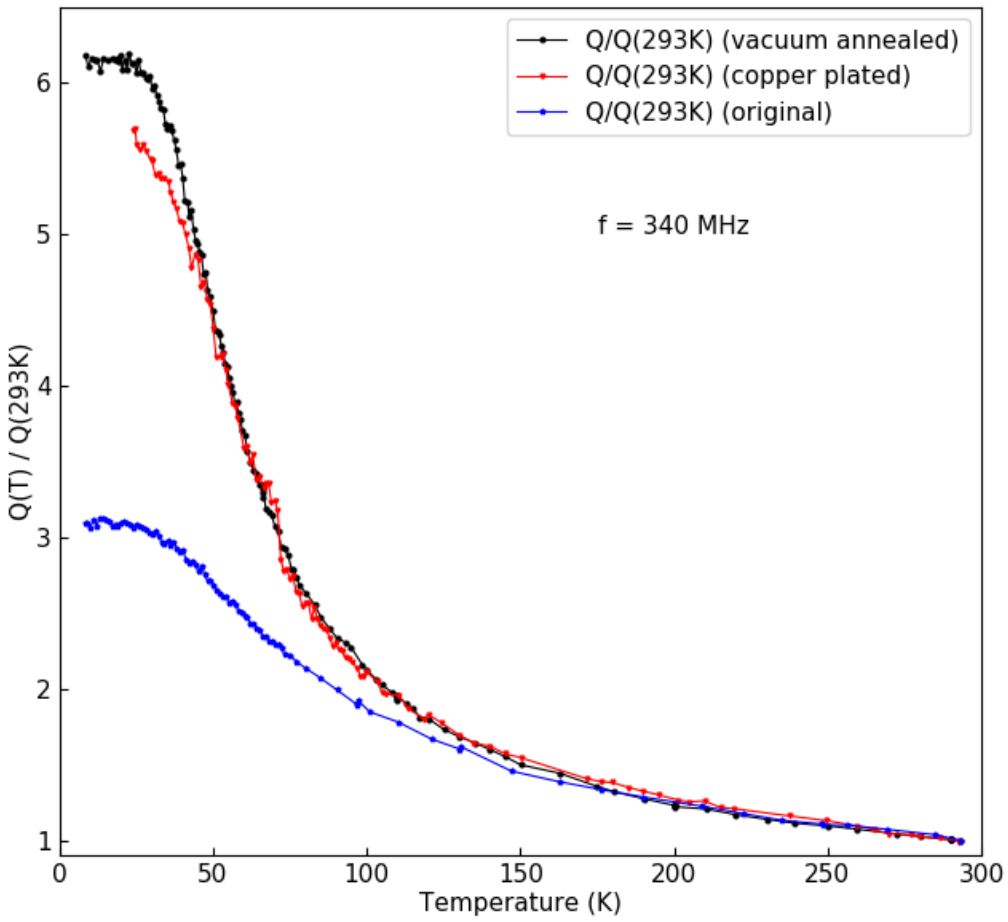

Figure 7.4: Measured $Q(T)/Q(293K)$ – values over T for all three surface conditions of the 340 MHz cavity.

As we can see from this figure, the ratio of the Q factor after the copper plating is significantly improved, which means, the RRR - value becomes much larger. The black curve shows the results after the vacuum annealing and indicates that this treatment indeed is giving some improvement additionally to the copper-plating.

7.5 Comparison with Theory

We cannot directly measure the RRR - value of the cavity after the copper plating and vacuum annealing to compare with the measured Q ratio and judge whether

the anomalous skin effect has affected the measurement results. However, one can calculate the RRR - value based on the measurements by referring to the theory and the geometric model described in Chapter 4.3.

Based on the method described in Chapter 7.3 and the measured $Q(T)/Q(293K)$, the DC-values for $\sigma(T)/\sigma_n$ for the vacuum annealed cavity can be calculated and the square root of it is plotted in Fig. 7.5.

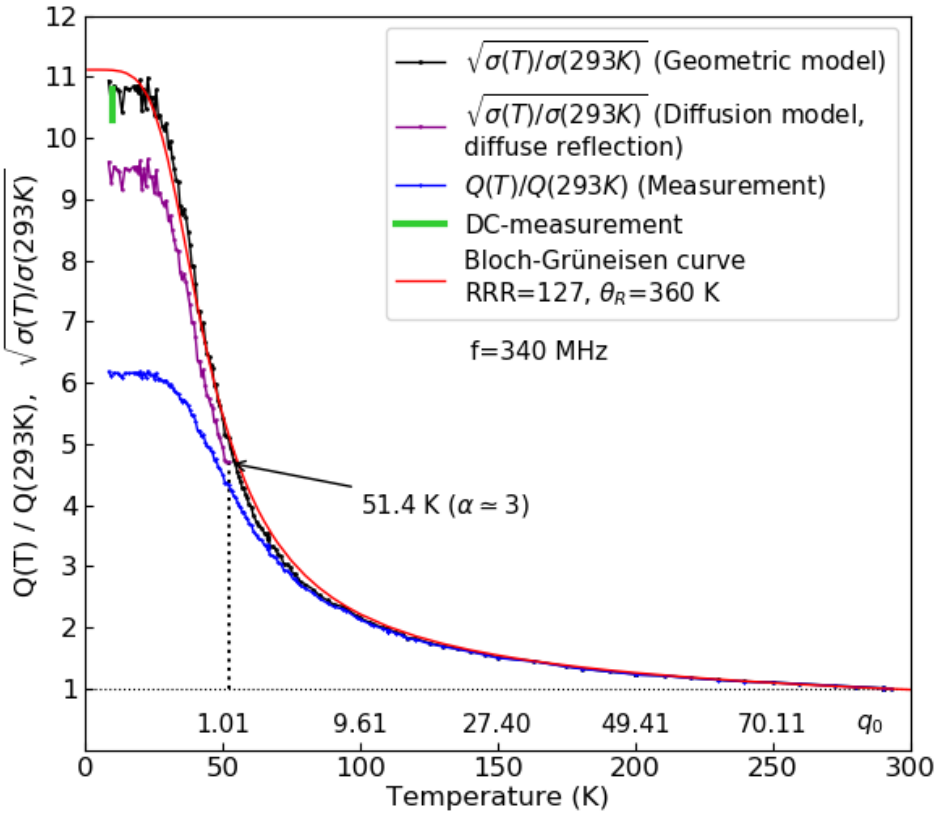

Figure 7.5: Calculated square-roots of the DC-conductivity ratios from the measured Q-value ratios. The DC–measurement for galvanically copper-plated layers is from Ref. [14].

According to Eq. (4.65), one obtains the value of h_0 from the calculated q_0 and q_l from the measurements. According to Eq. (3.3),

$$\frac{R(T)}{R_c(T)} = \sqrt{\frac{\sigma(T)}{\sigma_a(T)}} \tag{7.3}$$

Substituting h_0 into Eq. (4.72b and 4.73) and times the measured $Q(T)/Q(293K) =$

$\sqrt{\sigma_a(T)/\sigma(293K)}$ (see Eq. (7.4)), we get the $\sigma(T)/\sigma_n$ based on the diffusion model[9]. The results are also plotted in Fig. 7.5.

$$\frac{R(T)}{R_c(T)} \cdot \frac{Q(T)}{Q(293K)} = \sqrt{\frac{\sigma(T)}{\sigma_a(T)}} \cdot \sqrt{\frac{\sigma_a(T)}{\sigma(293K)}} = \sqrt{\frac{\sigma(T)}{\sigma(293K)}} \tag{7.4}$$

The calculated ratio at lowest temperatures of $\sqrt{\sigma(T)/\sigma(293K)} \cong 11$ means, that the RRR–value for that copper sheath corresponds to RRR $= 11^2 \cong 121$. This is just slightly above the results published in Ref. [14] for DC-measured RRR - values between 107 and 117 of galvanically copper-plated vacuum and annealed layers. The calculated value of $\sqrt{\sigma(T)/\sigma(293K)}$ at the lowest temperature based on the diffusion model is about 18% below that obtained from the geometric model.

The measured Q factor ratio at the lowest temperature is just 6.18, which is much smaller than 11. That means, the anomalous skin effect plays a key-roll by the measurements of the 340 MHz cavity after the copper plating and vacuum annealing. Figure 7.5 shows that the anomalous skin effect has already started to affect the measurements of the quality factor from about 100 K and the effects becomes larger and larger as the temperature decreases. Nevertheless, the ratio of the quality factor at 40 K is still 5.37 and at 50 K 4.5. Accelerators operated around these temperatures still have a lot of potential: the RF power losses are reduced by these factors. Additionally, measurements at cryogenic temperature operation of copper cavities showed a higher electric surface field limit [17, 24, 23]. This should allow for am optimum accelerator layout with respect to RF power amplifiers and compactness of the linac for short pulsed operation. The tolerable pulse lengths will bi discussed in chapter 8.

Chapter 8

Pulsed Normal-Conducting Ion Linac Operation at Cryogenic Temperatures

From the measurements described in the previous chapter, one can conclude that the RF conducting sheath has to be electrolytically copper-plated on a standard bulk copper material. From publications on electron structures one can deduce, that bulk OFHC – copper with RRR - values well above 100 can be delivered by industry. On the other hand, Fig. 4.3 clearly shows, that RRR – values above 300 will not improve the results significantly, as long as the intended operation temperature is 40 K or higher.

The backing material has to provide excellent heat conduction properties to keep the cavity surface close to the temperature of the coolant. The electrical conductivity dependence on temperature limits the allowed surface temperature increase within an RF pulse:

From Eqs. (3.3, 3.4) it follows that $P \sim \sigma_a^{-1/2}$. If for example a change of the amplifier RF power of 5% during one pulse is assumed acceptable and can be handled safely by the low-level RF controls, one can find from the function $\sqrt{\sigma_a(T)}$ the allowed temperature increase ΔT, corresponding to a 5% - variation of $\sqrt{\sigma_a(T)}$.

In the following, RF levels with a power loss density of $5MW/m^2$ at 300 K are investigated and compared with the other two cryogenic temperatures, namely 77 K and 40 K. The surface temperature rise and the temperature profile into the bulk copper is studied in the following for RF pulse lengths τ of 50, 200 and 500 μs. The power level at the cryogenic temperatures is reduced according to the corresponding

change of Q_0, to keep the acceleration voltage for all three cases about constant.

8.1 Surface Temperature Response and Temperature Profile

There are three modes of heat transfer: conduction, convection, and radiation. The wall of a cavity can be considered as a semi-infinite solid shown in Fig. 8.1 and is cooled down to an initial temperature T_i. A short, instantaneous pulse of energy is applied at the surface of the wall. The surface temperature is suddenly raised to a temperature T_0 at the end of the pulse. Due to the temperature gradient between the surface and the solid body, the energy will be transferred from the high-temperature region to the low-temperature region by conduction. Further, the wall is then cooled by contact with the coolant (such as liquid nitrogen, liquid helium). More details on that topic are described in Ref. [16].

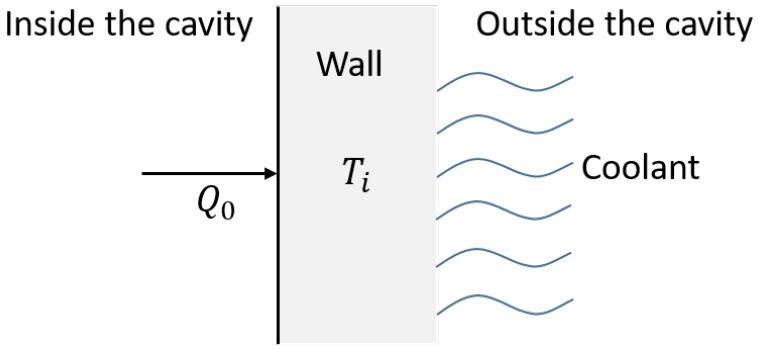

Figure 8.1: Schematic diagram for a short, instantaneous pulse of energy at the wall surface of a cavity

In this work we focus on the conduction process from the surface to the bulk copper after the energy pulse is applied to the surface. The temperature response in time and along y into the copper wall after the pulse is given by [16, p. 139]

$$\Delta T = \frac{W_0}{A\rho c \cdot \sqrt{\pi \alpha t}} \cdot e^{-y^2/4\alpha t} \tag{8.1}$$

with $W_0/J = p \cdot \tau \cdot A$ is the energy of the pulse, p the power loss density, $c/kJ/kg \cdot K$ the specific heat, $\alpha/m^2/s$ the thermal diffusivity, $\rho/kg/m^3$ the density of copper,

A/m^2 the area of the cavity surface. t the time after heat pulse. $y = 0$ denotes the surface.

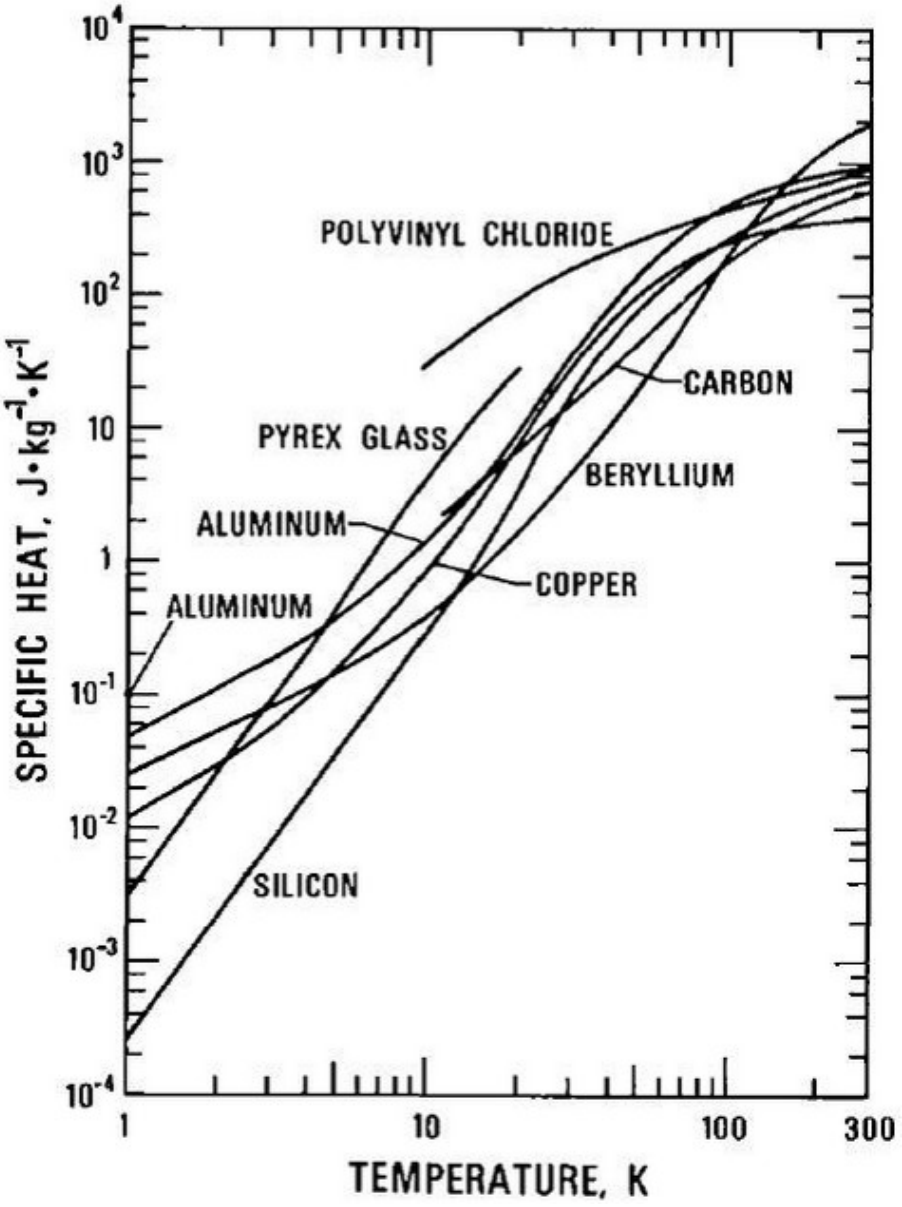

Figure 8.2: Specific heat dependence on temperature for several materials[35].

According to Eq. (3.5),

$$Q_0 \propto \frac{1}{P} \tag{8.2}$$

Therefore,

$$\frac{P_{77K}}{P_{300K}} = \frac{Q_{0,300K}}{Q_{0,77K}} \tag{8.3}$$

$$\frac{P_{40K}}{P_{300K}} = \frac{Q_{0,300K}}{Q_{0,40K}} \tag{8.4}$$

RF levels with a power loss density of $5MW/m^2$ at 300 K are investigated as well at 77 K and 40 K. To keep the acceleration voltage for all three temperature cases about constant, the power levels at the two cryogenic temperatures are reduced according to the corresponding change of Q_0 (see Eqs. (8.3 and 8.4)) and listed in Table 8.1.

The specific heat c and the thermal diffusivity α for different temperatures can be read from Figs. 8.2 and 8.3 respectively and are also listed in Table 8.1. The values

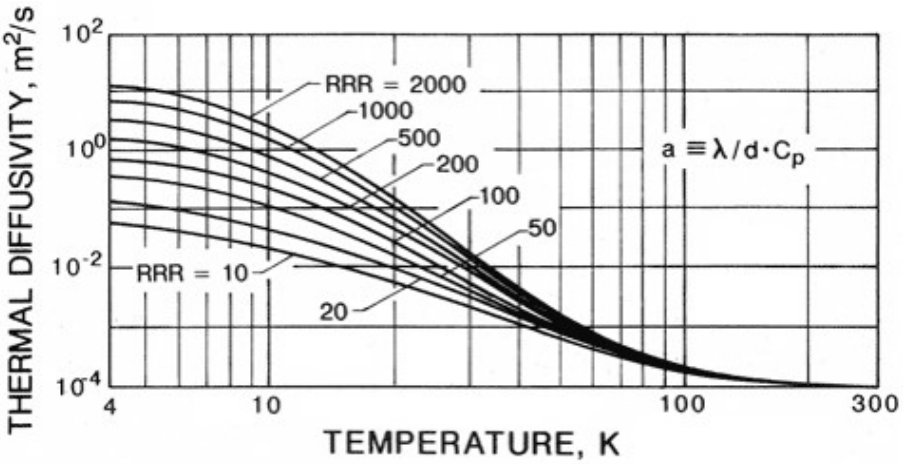

Figure 8.3: Thermal diffusivity of copper dependent on temperature with RRR from 10 to 2000[35].

Table 8.1: Thermal parameters for 300, 77 and 40 K.

Temperature	$Q_0(T)/Q_{0,300K}$	p(MW/m^2)	c(J/kg · K)	$\alpha(m^2/s)$
300 K	1	5	400	0.0001
77 K	2.734	1.8288	200	0.0003
40 K	5.368	0.9314	60	0.002

of the thermal diffusivity α were chosen from the curve with RRR = 100 in Fig. 8.3, which was assumed as a more pessimistic case as α profits from a higher RRR-value.

The results for the time dependence of the surface temperature at $y = 0$ are plotted in Fig. 8.4 for the three different operating temperatures with three RF pulse lengths of 50, 200 and 500 μs respectively.

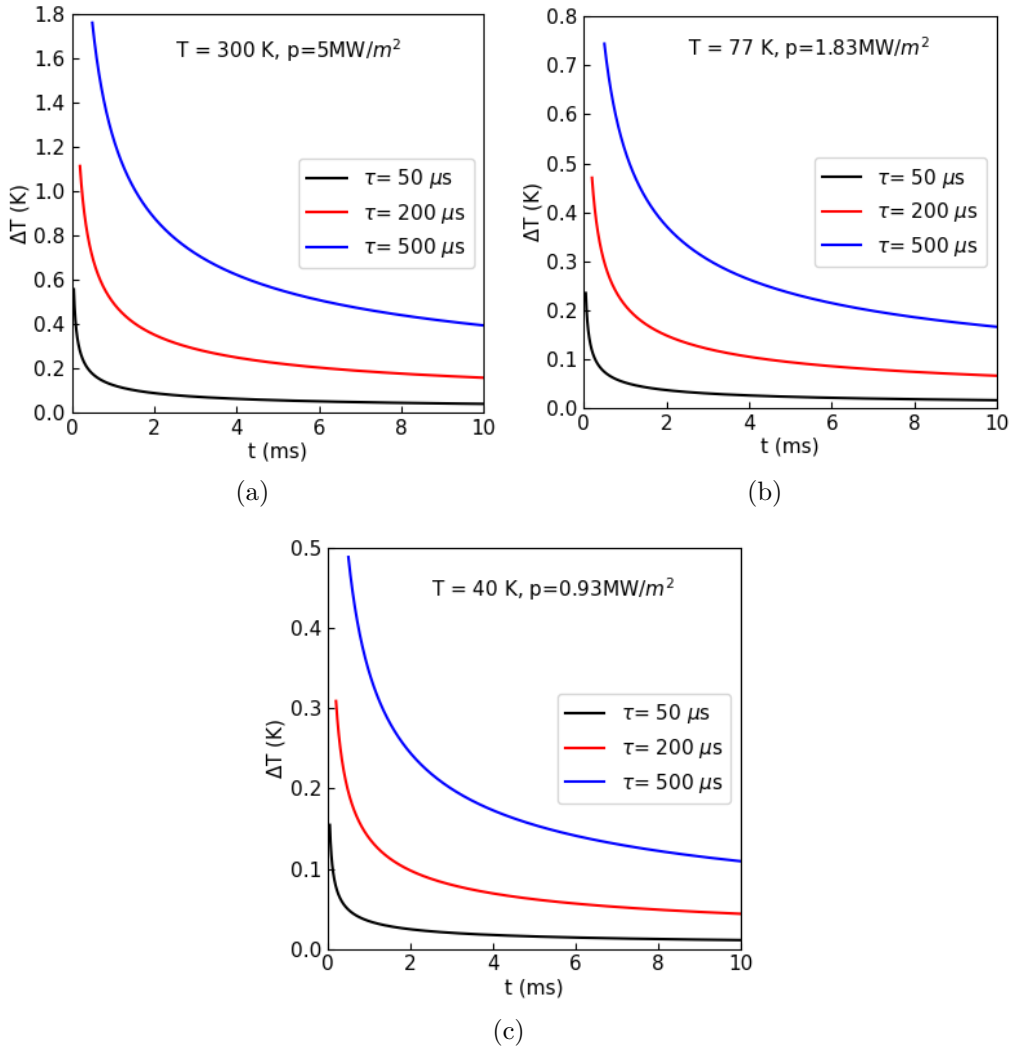

Figure 8.4: Plot of $\Delta T(t)$ for three pulse lengths and at three operation temperatures.

One can see, that pulse lengths as needed for injection into proton and ion synchrotrons can be realized by a cryogenic operation of copper linacs, up to very high acceleration fields. The temperature rise during one pulse remains within an acceptable range at a defined 40K - operation temperature:

From Fig. 7.4 it can be deduced that the relative change of the intrinsic Q - value is about 1.7%/K at that temperature. This will lead to only a modest change in

reflected RF power during pulses like plotted in Picture (c) of Fig. 7.4. Pulse lengths up to the ms–range seem feasible.

Another important aspect is the heat transport velocity from the cavity surface to the coolant. It has to be assured, that the cavity surface temperature has come back close to the starting value before the next RF pulse would be applied. Figure. 8.5 shows the temperature profiles along the heat transport coordinate y – one ms after the heat pulse application, $t = 1ms$. Figure 8.6 finally shows the two-dimensional temperature distributions along t and y for all three operation-temperature cases for a RF pulse length of 500 μs.

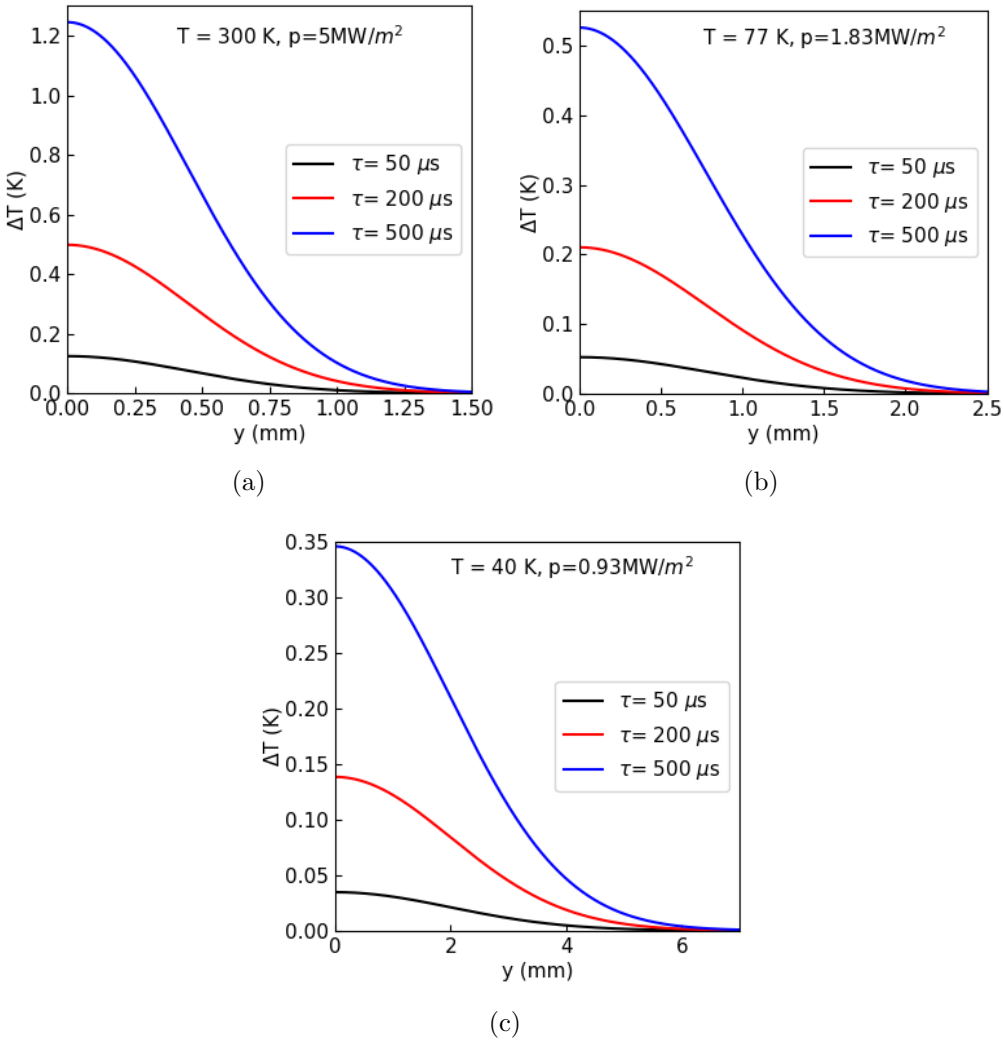

Figure 8.5: Plot of $\Delta T(y)$ one ms after the energy was applied on the surface.

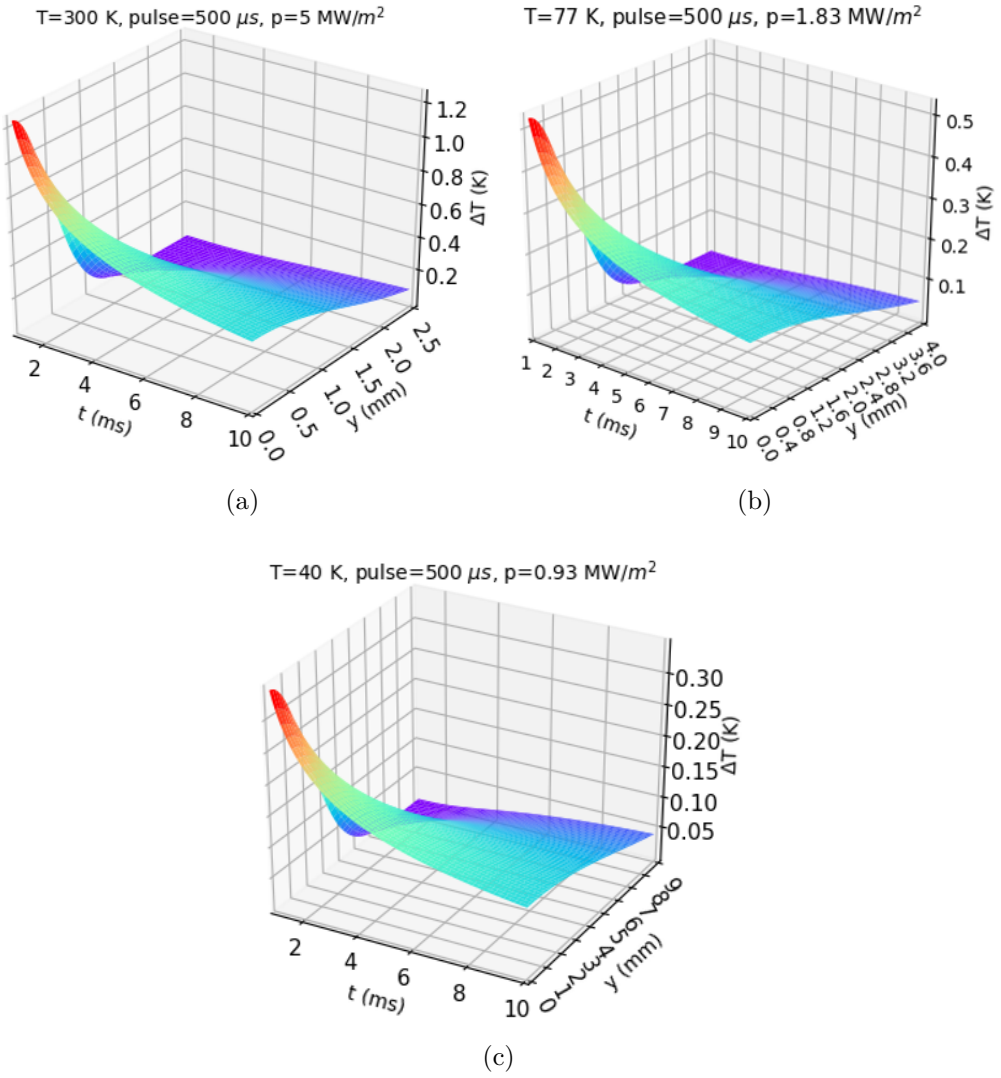

Figure 8.6: Temperature distribution in time and penetration depth.

8.2 Suggested Cavity Geometries and Cooling

Compact and simple drift tube cavities like shown by Fig. 8.7 are preferable for cryogenic temperature operation. KONUS– and APF–beam dynamics allow for a sequence of simple drift tubes, containing no focusing elements. In case of KONUS, magnetic quadrupole triplets are providing the transverse focusing after each sequence of simple drift tubes [29]. The cavities should preferably be built from bulk copper and with RRR - values around 150 to get an attractive performance at operation temperatures between 40 and 50 K. H-type cavities seem very well suited for this

purpose. However, the transition from the established copper-plated stainless-steel cavity technology to bulk copper cavities has to be made. An alternative might be thick-plated (a few mm) stainless steel cavities.

Cooling down to 77 K is easy with liquid nitrogen. The final cooling stage has to be designed according to the exact operating temperature and size of a facility. Optional concepts are described in Ref. [12].

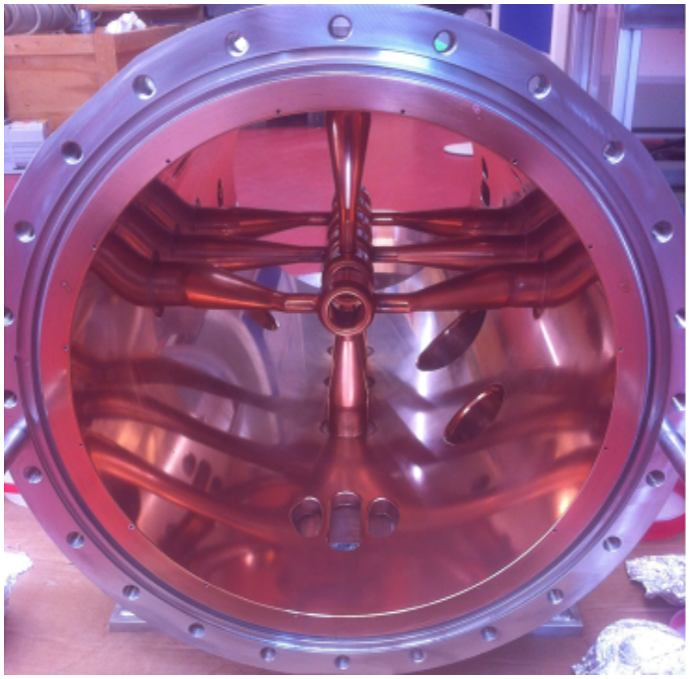

Figure 8.7: View into a 7 gaps, 325 MHz prototype CH–cavity for room-temperature operation[1]. The inner diameter is 330 mm.

Chapter 9

Summary and Outlook

Operating normal conducting accelerators at cryogenic temperature has became an interesting topic recently. The cryogenic operation of ion linacs is discussed and investigated for the first time at IAP in Frankfurt since around 2012. On one hand, the material copper shows a significantly higher conductivity at temperatures of liquid nitrogen and below. On the other hand, the anomalous skin effect reduces the gain in shunt impedance. The aim of this work is to study, how the anomalous skin effect affects the efficiency of copper-cavities in the temperature range 40 - 50 K.

For the experiment, three coaxial cavities were designed and built. The exact values of the lengths of the outer cylinder and the size of the gap were verified in simulations with CST Microwave Studio (MWS): 735 mm for the 100 MHz cavity, 324 mm for the 220 MHz cavity and 201 mm for the 340 MHz cavity; the size of the gap is 54 mm.

The simulated Q_0 are 13060 for the 100 MHz cavity, 17264 for the 220 MHz cavity and 19665 for the 340 MHz cavity. The measured Q_0 are 11803 for the 100 MHz cavity, 15812 for the 220 MHz cavity and 17569 for the 340 MHz cavity, which take 90.4%, 91.6% and 89.3% of the simulated values, respectively.

Two small loops (see Fig. 6.1) were used for the input and output coupler. The coupling strengths of them at room temperature has the order -4 and at cryogenic temperature near 4 K the order -3, which means, the coupling between the coupler and the cavity is very weak and the directly measured Q_L from the network analyzer can be seen as a good approximation of Q_0.

The low-level RF-conditioning took place from 0 W up to 50 W cw and stayed at

the maximum level for about three hours to burn off impurities and dust particles on the surface. The cavities were pumped by a combination of a turbo pumping-station and an ion getter-pump, as in use for the test of superconducting cavities. Temperature sensors were used to record the temperature changes. After cavity preparations, the whole experimental setup was placed in the cryostat and cooled down to about 10 K with liquid helium.

The quality factor measurements were performed during the warming up phase of the cavity. From the results we can conclude that the RRR-values of the original bulk-copper were very low - RRR $\cong$ 11. This is not unusual for bulk - copper with unspecified cryogenic capabilities. Subsequently, the 340 MHz cavity was matt copper-plated and further vacuum annealed at 400°C for one hour. The results showed that the copper plating improved significantly the Q factor, which means, the RRR - value becomes much larger and the vacuum annealing gave some improvement additionally to the copper-plating.

Since the diffusion theory based on electron small-angle scattering for the calculation of the anomalous skin effect is known to deliver somewhat too good results in the microwave range below 1 GHz and in the temperature range of interest here, a "geometric model" was developed, which is based on the fact that so-called Umklapp process plays an essential role in electron movement. This model compares well with our own measurements and with measurements from the literature.

Comparing the measured results of the 340 MHz cavity after the copper plating and vacuum annealing with the calculated RRR-value based on the measurements by referring to the theory and the geometric model described in Chapter 4.3, the ratio of the measured Q factor is 6.18 at the lowest temperature, while calculated $\sqrt{\sigma(T)/\sigma(293K)}$ from the geometric model is about 11, correspondingly, the RRR–value for that copper sheath is about $11^2 = 121$, which is just slightly above the results published in Ref. [14] for DC-measured RRR-values between 107 and 117 of galvanically copper-plated and vacuum annealed layers. The calculated value of $\sqrt{\sigma(T)/\sigma(293K)}$ at the lowest temperature based on the diffusion model is about 18% below that obtained from the geometric model. Nevertheless, the ratio of the quality factor at 40 K is still 5.37 and at 50 K 4.5. The RF power losses of the accelerators operated around these temperatures are reduced by these factors.

According to the simulated results of the temperature response to a short, instantaneous pulse of energy, the temperature rise during one pulse remains within an acceptable range at a defined 40 K - operation temperature. The change of Q_0 is small and the modest change in the reflected RF power can be handled safely by the low-level RF controls. Additionally, measurements at cryogenic temperature operation of copper cavities showed a higher electric surface field limit [17, 24, 23]. All these advantages should allow for an optimized accelerator layout with respect to RF power amplifiers and compactness of the linac at cryogenic temperature.

In case of the FAIR project at Darmstadt, a 100 A MeV injector linac into the SIS100 - providing the specified high particle number - could be realized by such a technology in a later upgrade project.

Bibliography

[1] Ali Almomani and Ulrich Ratzinger. A 325 mhz high gradient ch–test cavity for β= 0.16. In *Proceedings of the 5th International Particle Accelerator Conference (IPAC14), Dresden Germany*, page 3229, 2014, DOI:10.18429/JACoW-IPAC2014-THPME010.

[2] J. L. Altman. *Microwave Circuits*. D. Van Nostrand, Princeton, N.J., 1964.

[3] Neil W Ashcroft and N David Mermin. *Solid state physics*. Holt-Saunders Int. Ed., 1976.

[4] Mei Bai et al. A "cool" route to the higgs boson and beyond. *arXiv preprint arXiv:2110.15800*, 2021.

[5] Hans Heinrich Braun, Steffen Döbert, I Wilson, and Walter Wuensch. Frequency and temperature dependence of electrical breakdown at 21, 30, and 39 GHz. *Physical review letters*, 90(22):224801, 2003.

[6] Robert M. Brodhage. Aufbau und Hochfrequenzabstimmung einer IH-Kavität für den neuen Schwerioneninjektor am Brookhaven National Laboratory. Master's thesis, Goethe University Frankfurt.

[7] Marco Busch. Lecture script: Anwendung der supraleitung in bescheuniger- und fusionstechnologien, Institute for Applied Physics, Goethe Univercity Frankfurt, 2021.

[8] A Cahill, A Fukasawa, J Rosenzweig, et al. Measurements of copper rf surface resistance at cryogenic temperatures for applications to x-band and s-band accelerators. *Proc. of the LINAC2016 Conf., Busan, Korea*, 2016, DOI:10.18429/JACoW-IPAC2016-MOPMW038.

[9] RG Chambers. The anomalous skin effect. *Proceedings of the Royal Society of London. Series A. Mathematical and Physical Sciences*, 215(1123):481–497, 1952.

[10] Alexander Wu Chao, Karl Hubert Mess, et al. *Handbook of accelerator physics and engineering*. World scientific, 2013.

[11] Weiren Chou and Francesco Ruggiero. Anomalous skin effect and resistive wall heating. Technical report, CERN-LHC-Project-Note-2, 1995.

[12] Petar Dalakov, Erik Neuber, Jürgen Klier, and Ralf Herzog. Innovative neon refrigeration unit operating down to 30 k. In *MATEC Web of Conferences*, volume 324, page 01003. EDP Sciences, 2020.

[13] Donald G. Fink and Beaty H. Wayne. *Standard handbook for electrical engineers*. McGraw-Hill, 14th edition, 2000.

[14] M Fouaidy and N Hammoudi. Rrr of copper coating and low temperature electrical resistivity of material for ttf couplers. *Physica C: Superconductivity*, 441(1-2):137–144, 2006.

[15] Hendrik Hähnel and Ulrich Ratzinger. First 3D printed IH-type linac structure—proof-of-concept for additive manufacturing of linac RF cavities. *Instruments*, 6(1):9, 2022.

[16] Jack P Holman. *Heat transfer.* McGraw Hill Higher Education, 10 edition, 2010.

[17] Marek Jacewicz, Johan Eriksson, Roger Ruber, Sergio Calatroni, Iaroslava Profatilova, and Walter Wuensch. Temperature-dependent field emission and breakdown measurements using a pulsed high-voltage cryosystem. *Physical Review Applied*, 14(6):061002, 2020.

[18] John David Jackson. Classical electrodynamics, 1999.

[19] Howard Johnson and Martin Graham. *High-speed signal propagation: advanced black magic*. Prentice Hall Professional, 3rd edition, 2003.

[20] Richard Allen Matula. Electrical resistivity of copper, gold, palladium, and silver. *Journal of Physical and Chemical Reference Data*, 8(4):1147–1298, 1979.

[21] E Meyer and R Pottel. In *Physikalische Grundlagen der Hochfrequenztechnik*. Springer, 1969.

[22] Theodore Moreno. Microwave transmission design data. 1948.

[23] Mamdouh Nasr, Emilio Nanni, Martin Breidenbach, Stephen Weathersby, Marco Oriunno, and Sami Tantawi. Experimental demonstration of particle acceleration with normal conducting accelerating structure at cryogenic temperature. *Physical Review Accelerators and Beams*, 24(9):093201, 2021.

[24] Kai Nordlund and Flyura Djurabekova. Defect model for the dependence of breakdown rate on external electric fields. *Physical Review Special Topics-Accelerators and Beams*, 15(7):071002, 2012.

[25] Alfred Brian Pippard. The anomalous skin effect in normal metals. *Proceedings of the Royal Society of London. Series A. Mathematical and Physical Sciences*, 191, 1947.

[26] Holger Podlech. *Entwicklung von normal- und supraleitenden CH-Strukturen zur effizienten Beschleunigung von Protonen und Ionen*. Habilitation thesis, Goethe University Frankfurt am Main, 2008.

[27] Simon Ramo, John R. Whinnery, and Theodore Van Duzer. *Fields and waves in communication electronics*. John Wiley & Sons, 1994.

[28] Ulrich Ratzinger. Aufbau eines Harmonischen-Bunchers am Garchinger Schwerionennachbeschleuniger. Master's thesis, Technical University of Munich, 1981.

[29] Ulrich Ratzinger, Hendrik Hähnel, Rudolf Tiede, Jan Kaiser, and Ali Almomani. Combined zero degree structure beam dynamics and applications. *Physical Review Accelerators and Beams*, 22(11):114801, 2019.

[30] Ulrich Ratzinger and Huifang Wang. The anomalous skin effect and copper cavity operation at cryogenic conditions. *arXiv preprint arXiv:2211.00135*, 2022.

[31] GEH Reuter and EH Sondheimer. The theory of the anomalous skin effect in metals. *Proceedings of the Royal Society of London. Series A. Mathematical and Physical Sciences*, 195(1042):336–364, 1948.

[32] Sergei Alexander Schelkunoff. Electromagnetic waves. 1943.

[33] K. W. Shepard. Status of Low and Intermediate Velocity Superconducting Accelerating Structures PAC 2003,. *Portland, may*, 2003, DOI: 10.1109/PAC.2003.1288981.

[34] CST studio suite. Electromagneitc field simulation software. https://www.3ds.com/products-services/simulia/products/cst-studio-suite/.

[35] C.A. Thompson, W. M. Manganaro, and F.R. Fickett. Cryogenic Properties of Copper. https://www.copper.org/resources/properties/cryogenic/, July 1990.

[36] Ratzinger Ulrich. Script of the lecture "linear accelerator", 2022.

[37] Huifang Wang, U Ratzinger, and M Schuett. Operations of copper cavities at cryogenic temperatures. In *Proc. of the IPAC2021 Conf. Campinas, Brazil*, page 1020, 2021, DOI:10.18429/JACoW-IPAC2021-MOPAB329.

[38] Thomas P. Wangler. *RF Linear accelerators*. John Wiley & Sons, 2. edition, 2008.

[39] Alan Herries Wilson. The theory of metals. *The Theory of Metals*, 2011.

[40] Otto Zinke and Heinrich Brunswig. *Hochfrequenztechnik 1: Hochfrequenzfilter, Leitungen, Antennen*. Springer-Verlag, 2013.

Appendices

Appendix A

Technical Drawings of the Cavities

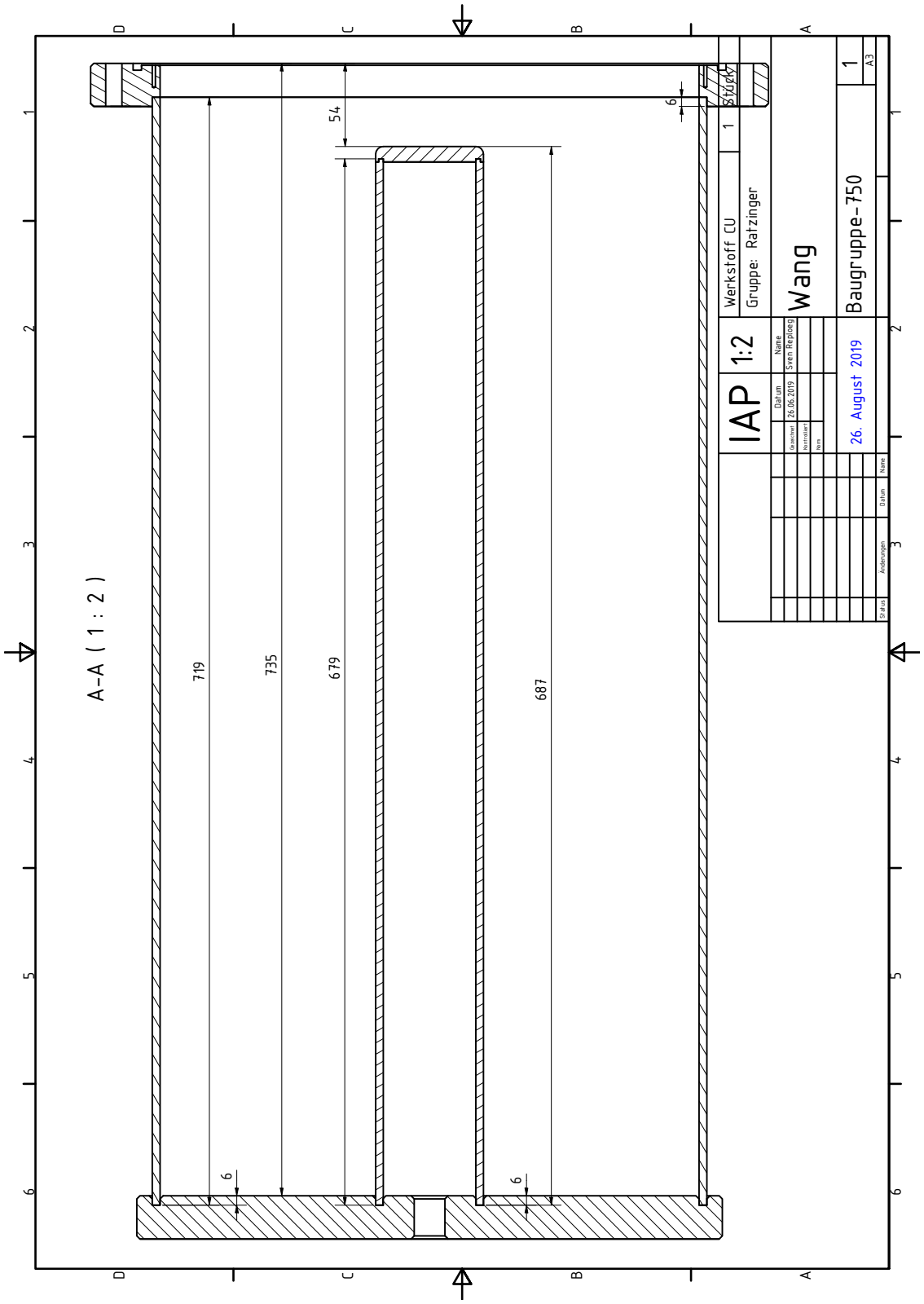

Figure A.1: Design of the 100 MHz cavity.

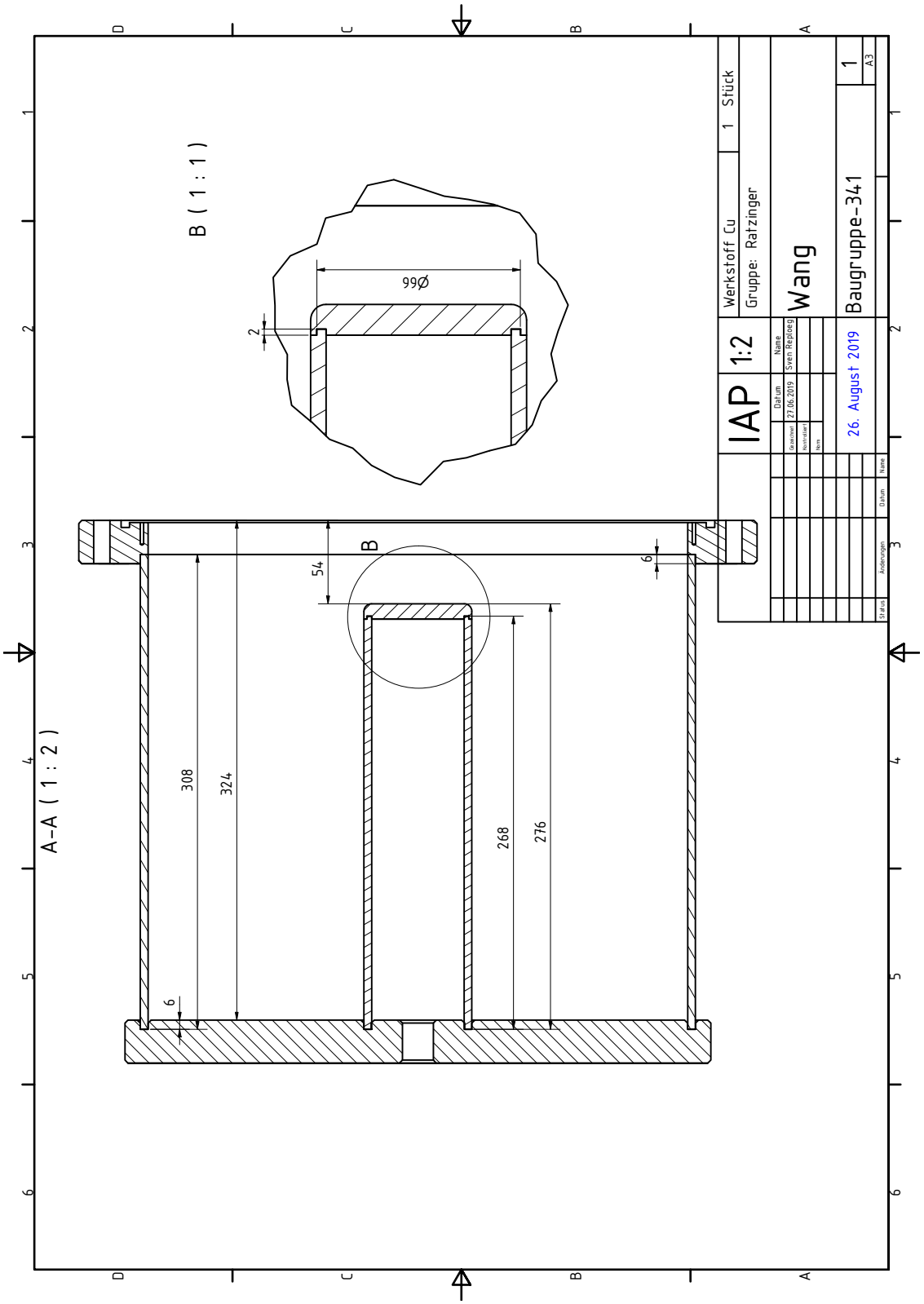

Figure A.2: Design of the 220 MHz cavity.

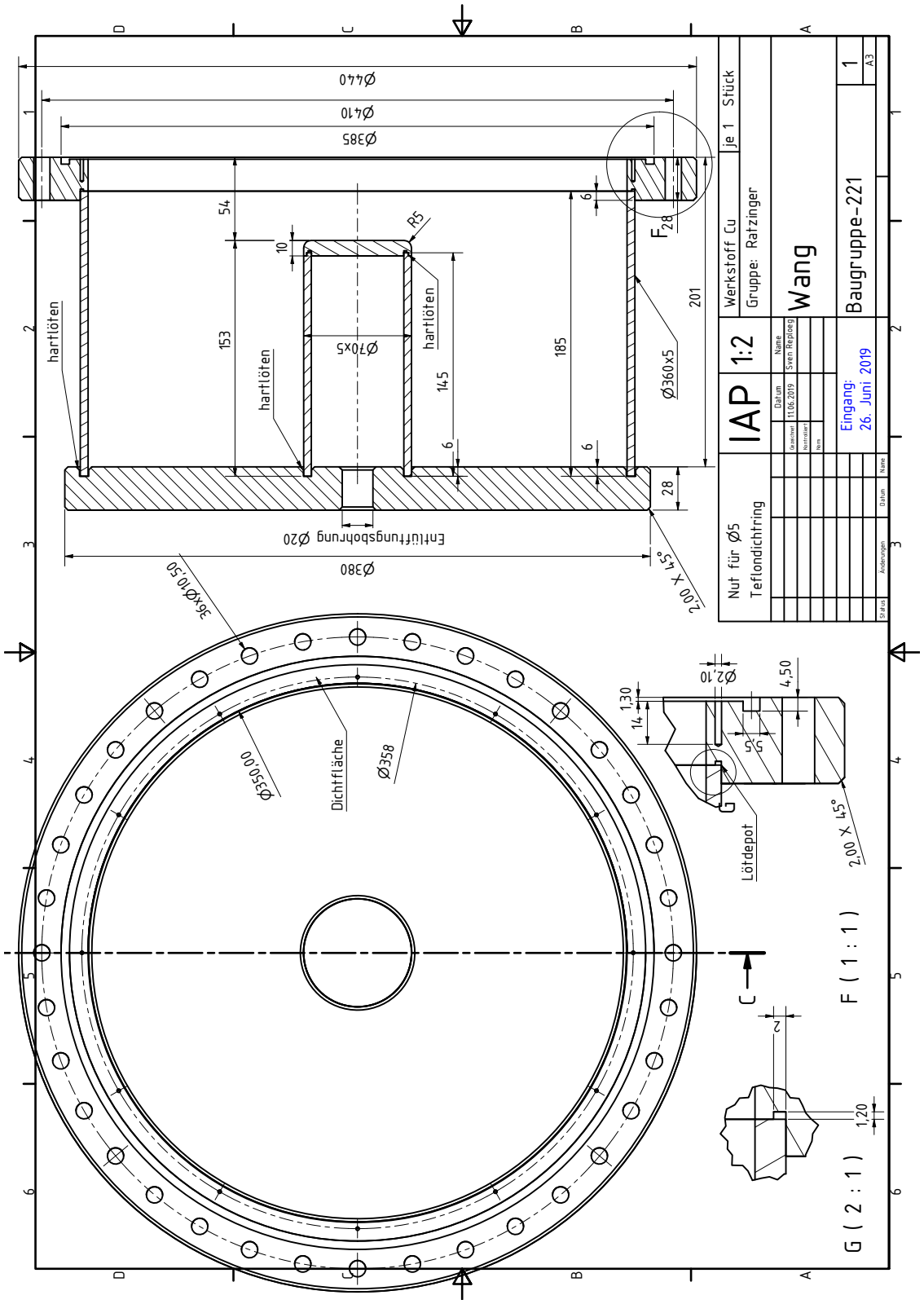

Figure A.3: Design of the 340 MHz cavity.

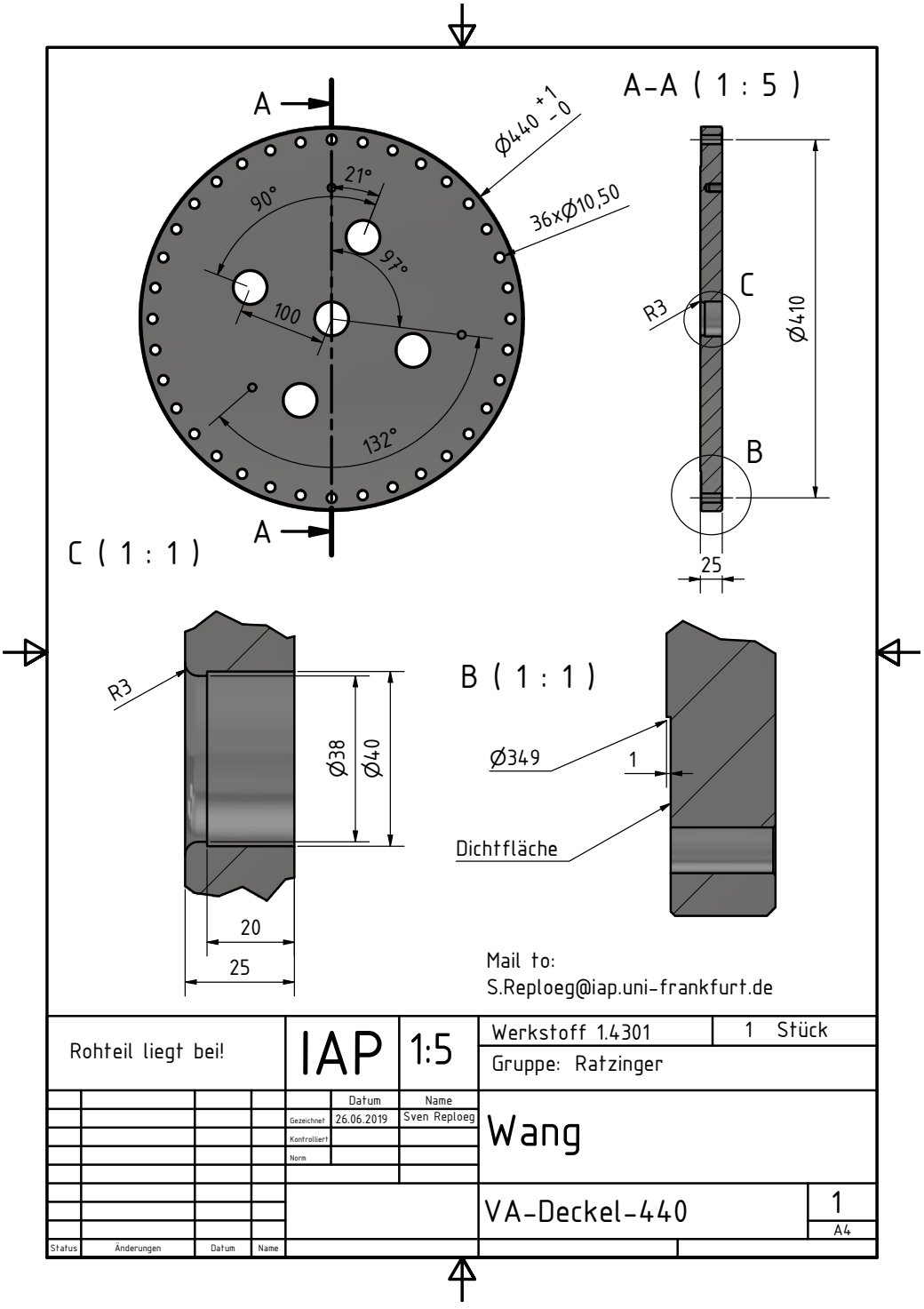

Figure A.4: Structure design of the cover.

Appendix B

Tabulated Values of $F_{l,s}$, $F_{l,d}$, F_l and h_0-(h_l, q_l)-q_0-Correlations for Copper

Table B.1: Values of $F_{l,s}$, $F_{l,d}$, F_l and h_0-(h_l, q_l)-q_0-Correlations.

h_0	q_0	h_l, q_l	$F_{l,s}$	$F_{l,d}$	$F_l(a = 0.75)$
0.005	0.20081	0.01712	0.09565	0.05646	0.08526
0.00619	0.20923	0.02001	0.10733	0.06370	0.09565
0.008	0.22032	0.02416	0.12309	0.07358	0.10965
0.01073	0.23450	0.03000	0.14371	0.08666	0.12793
0.0213	0.27564	0.05001	0.20451	0.12617	0.18147
0.03961	0.32628	0.08000	0.27801	0.17568	0.24525
0.05298	0.35625	0.10000	0.31964	0.20449	0.28079
0.07431	0.39784	0.13000	0.37452	0.24326	0.32689
0.08922	0.42401	0.15000	0.40725	0.26682	0.35394
0.11241	0.46156	0.18000	0.45182	0.29942	0.39019
0.12833	0.48575	0.20000	0.47900	0.31963	0.41196
0.15281	0.52109	0.23001	0.51665	0.34806	0.44168
0.16946	0.54412	0.25000	0.53988	0.36589	0.45979
0.19487	0.57805	0.28000	0.57228	0.39121	0.48476
0.21207	0.60035	0.30000	0.59239	0.40724	0.50012
0.25581	0.65520	0.35000	0.63800	0.44471	0.53468
0.30042	0.70912	0.40000	0.67752	0.47900	0.56465
0.34573	0.76239	0.45000	0.71145	0.51060	0.59089
0.39156	0.81530	0.50000	0.74020	0.53987	0.61413
0.43797	0.86735	0.55000	0.76382	0.56707	0.63483
0.48487	0.91878	0.60000	0.78350	0.59240	0.65378
0.53243	0.96876	0.65000	0.80015	0.61600	0.67148
0.58049	1.01791	0.70000	0.81443	0.63800	0.68823
0.62913	1.06588	0.75000	0.82680	0.65849	0.70420
0.6783	1.11280	0.80000	0.83762	0.67753	0.71946
0.72796	1.15891	0.85000	0.84718	0.69519	0.73400
0.77799	1.20443	0.90000	0.85567	0.71148	0.74777
0.82828	1.24972	0.95000	0.86326	0.72644	0.76068
0.87826	1.29765	1.00031	0.87014	0.74028	0.77275
1.382	1.76709	1.50000	0.91340	0.82680	0.84845
1.8833	2.25580	2.00008	0.93505	0.87010	0.88634
2.384	2.74942	2.50007	0.94804	0.89608	0.90907
2.8844	3.24529	3.00000	0.95670	0.91340	0.92423
3.3848	3.74253	3.50007	0.96289	0.92577	0.93505
3.885	4.24041	4.00003	0.96753	0.93505	0.94317
4.3852	4.73883	4.50004	0.97113	0.94227	0.94948
4.8854	5.23763	5.00009	0.97402	0.94804	0.95454
5.8856	6.23574	6.00007	0.97835	0.95670	0.96211
6.8857	7.23437	7.00001	0.98144	0.96289	0.96753
7.8858	8.23338	8.00000	0.98376	0.96752	0.97158
8.8859	9.23263	9.00001	0.98557	0.97113	0.97474
9.886	10.23206	10.00003	0.9870	0.97402	0.97727

Appendix C

Units and Variables

Variable	Description
A	Area
A_0	Voltage amplitude
a	Radius of the inner conductor
α	Thermal diffusivity
b	Radius of the outer conductor
$\vec{B}$	Magnetic field
β_e	Coupling strength of the input coupler
β_t	Coupling strength of the pickup
c	Speed of light
	Specific heat
C	Capacitance
δ	Skin depth
$\vec{E}$	Electrical field
e	Electric charge of a electron
E_F	Fermi energy
ε_0	Vacuum permittivity
ε	Absolute permittivity $\varepsilon = \varepsilon_r \varepsilon_0$
f	Frequency

Variable	**Description**
Γ	Reflection coefficient
j	Current Density
$\vec{H}$	Magnetic field
L	Inductance
l	Length
	Mean free path of electron
λ	Wavelength
m	Mass of the electron
μ_0	Magnetic permeability of vacuum, $\mu_0 = 4\pi \times 10^{-7}$
μ_r	Relative permeability
n_e	Free electron density
P_c	Power losses (Ohmic)
P_e	Emitted Power
P_f	Forward Power
P_t	Transmitted Power
Φ	Magnetic Flux
ϕ	Phase
Q	Quality factor
Q_0	Intrinsic quality factor
Q_L	Loaded quality factor
q	Electric charge
R_s	Surface resistance
r_i	Radius of the inner conductor
r_o	Radius of the outer conductor
ρ	Electrical resistivity
	Density of copper
	Electric charge density
S_{ii}	Scattering parameters

Variable	Description
σ	Electrical conductivity
T	Temperature
t	time
τ	Collision time
	Pulse length
θ_R	Debye temperature
U_l	Voltage induced in the coupler loop
V	Volume
V_{max}	Maximum voltage Multipacting occurs
V_{min}	Minimum voltage Multipacting occurs
v	Velocity
v_F	Fermi velocity
W	Energy
ω	Angular frequency
Z_F	Impedance of free space
Z_L	Line Impedance in vacuum

Acknowledgements

Zunächst danke ich Prof. Dr. Ulrich Ratzinger für die Annahme als Doktorand in seine Arbeitsgruppe, die vielen fachlichen und außerfachlichen Diskussionen, für seine Kollegialität und seine Unterstützung in allen Belangen. Ebenso bedanke ich mich bei meinem Zweitgutachter Prof. Dr. Holger Podlech!

Ein großer Dank gilt dem herausragenden, technischen Mitarbeiter Daniel Bänsch, ohne den die Kalttests kaum möglich gewesen wären. Danke für den unermüdlichen Einsatz, wenn mal wieder etwas schnell und sauber gelöst werden musste und für die fast täglichen Motivationsschübe. Ebenso danke ich dem Techniker Thomas Metz und Herr Siegfried Rapphahn für die Versorgung mit Flüssiggasen.

Darüber hinaus danke ich dem Werkstattteam rund um Herrn Reploeg für die zeitnahe Ertüchtigung essentieller Bauteile und die Organisation der Betriebsausflüge.

Ein weiterer herzlicher Dank gilt allen Mitgliedern (und Ehemaligen) des IAP für die großartige Zeit in der Arbeitsgruppe. Besonders erwähnt seien hier das Winterseminar und IPAC/Linac Konferenzreisen, die eine große Bereicherung des Erfahrungshorizontes erwirkten. Im speziellen möchte ich noch Dr. Maximilian Schütt, dem besten Tutor und Trainingspartner, herzlich danken! Ebenso danke ich Ezgi Sunar für die große Begleitung bei jeder Konferenz und freundliche Unterstützung.

Vielen Dank auch an Dr. Carl Kleffner für jedes PhD-Committee Meeting und freundliche Diskussionen. Ebenso danke Dr. Chuan Zhang für die Unterstützung bei der Bewerbung um das Stipendium.

Ebenso möchte ich GSI und der Firma Galvano-T für die Herstellung und Bearbeitung der Kavitäten danken.

Dem HGS-HIRe for FAIR sei für die durchgehende, finanzielle Unterstützung meiner Arbeit gedankt!

Zuletzt richte ich meinen Dank an meine Familie, sowie allen namentlich unge-

nannten Freunden, die mich in der ganzen Zeit geduldig unterstützt und motiviert haben. Danke, dass ihr an meiner Seite steht!

Akademische Lehrer

Prof. Dr. Joachim Stroth, Prof. Dr. Michael Huth, Dr. Marcus Iberler, Prof. Dr. Viktor Krozer, Prof. Dr. Ulrich Ratzinger, Prof. Dr. Holger Podlech, Dr. Marco Busch, Dr. Rudolf Tiede, Priv. Doz. Dr. Chuan Zhang, Prof. Dr. Luciano Rezzolla, Prof'in. Dr. Roser Valenti